

Micro- and Nanomechanical Study on Aluminum Bulk Material and Micromachined Surfaces

Dissertation von Pavel Sergeevic Filippov



München 2021

Micro- and Nanomechanical Study on Aluminum Bulk Material and Micromachined Surfaces

Dissertation

zur Erlangung des Grades eines Doktors der Naturwissenschaften an der Fakultät für
Geowissenschaften der Ludwig-Maximilians-Universität München

vorgelegt von

Pavel Sergeevic Filippov

München, den 23. Juli 2021

Erstgutachter: Prof. Dr. Markus Lackinger

Zweitgutachterin: Prof. Dr. Ursula Koch

Tag der mündlichen Prüfung: 22. Dezember 2021

Acknowledgements

It has only been possible to compose the present thesis due to the supportive environment which I have enjoyed for the last four years. At first, I want to thank my supervisor Prof. Dr. U. Koch who continually supported me during the dissertation. With her extensive knowledge in material science she provided the basis of this research. Prof. Koch helped to solve many complex problems always preserving the big picture.

Also not to be underestimated is the help of Prof. Dr. Lackinger who regularly provided a competent view on the research. He was always here to give advice and assistance with the scientific as well as with the organizational aspect of the dissertation.

It is also important to mention that a great part of this research has been funded by VDI/VDE. I also thank the FORWIN team of the Munich University of Applied Sciences (MUAS) for their advise and also for funding the publication of open access research and conference contributions.

I greatly appreciate the professional collaboration with *Rohde & Schwarz* and project partners from the *Forschungsinstitut für Edelmetalle + Metallchemie* and *Steinbeis Transfer Center Manufacturing Technology & Machine Tools*. Especially I want to thank Mr. M. Ebner and Prof. Dr. M. Kaufeld for sharing their expertise and also for informative and motivating discussions.

I want to thank the team of the *Laboratory for Materials Technology* at the *Munich University of Applied Sciences* for their support in the daily questions, many fun and encouraging moments and also for the cheerful atmosphere in the lab. This includes Dr. C. Eulenkamp, C. Hausner-Henzel, Prof. Dr. Steinhauser, Prof. Dr. G. Pham and others.

I also wish to thank my wife for her continuous support during this challenging but also exciting time. She not only encouraged me to trust in my abilities and to endure difficult situations. She also provided essential critical insights from the technical point of view. Her assistance concerning this thesis and beyond is invaluable. I also thank my parents who always jumped in and enthusiastically supported us when ever needed.

And last but not least:

אַתָּה חוֹנֵן לְאָדָם דַּעַת. וּמְלִמֵּד לְאָנוּשׁ בִּינָה:

“You graciously favor man with knowledge and teach mortals understanding.”

Abstract

To enable future applications of micromilling for production of small-scale components with sufficient precision and repeatability fundamental understanding of the process and changes in material behavior is necessary. For this purpose, microstructure and mechanical properties of aluminum-based materials subject to strain hardening were investigated. In the present thesis, crystal anisotropy (aluminum single crystals in (100), (110) and (111) orientations), plastic flow under uniaxial compression (recrystallized high purity aluminum) and the effect of micromilling on strain hardening of the AA6082 surface (micromilled with monocrystalline diamond (radius 17 nm) and solid carbide (radius 671 nm) tools) were studied in detail. Nanoindentation was used to investigate mechanical properties with high precision. It could be determined that crystal orientation influences the indentation modulus by 1.3 %. The combined effect of crystal symmetry and indenter geometry (Vickers indenter) was found to affect hardness and modulus by up to 1.8 %. Deformation behavior of aluminum under uniaxial load was found to be significantly influenced by the initial orientation of the respective grains and their slip-system in respect to the load direction. This led to highly anisotropic plastic flow for degrees of deformation over 40 % as resulting in an intermittent grain softening. This effect is attributed to dynamic discontinuous recovery. The milling experiments showed that the surface roughness is largely influenced by the cutting edge radius and roughness along the cutting edge. Depth and hardness of the deformation zone introduced due to the ploughing-effect was demonstrated to depend mostly on the cutting edge radius. The influence of cutter material on surface roughness and the ploughing effect is not considered to be significant. The monocrystalline diamond tool showed superior performance by producing very smooth and nearly undeformed surfaces. Based on our studies we conclude, that the it should be the tool of choice for high-precision micromanufacturing.

“If I have seen further it is by standing on the shoulders of giants.”

Sir Isaac Newton, 1675

In the first chapters, the necessary basis for the accomplished work is provided. Here it should be mentioned, that it is only thanks to the enormous efforts of previous generations of scientists and engineers, that the present research was possible.

Contents

Acknowledgements	iii
Abstract	v
Introduction	1
1 Introduction	1
2 Basics of Nanoindentation	5
2.1 Historical development of the hardness test	5
2.2 The nanoindentation experiment	7
2.3 Data analysis	9
2.4 Influencing factors	12
2.4.1 Instrument compliance	13
2.4.2 Indenter geometry	14
2.4.3 Piling-up and sinking-in	15
2.4.4 Indentation size effect	16
2.4.5 Surface roughness	18
2.5 Thin film hardness	19
2.5.1 Bückle’s rule	20
2.5.2 Depth-dependent nanoindentation	22
2.5.3 Film-substrate models	22
3 Elastic-Plastic Deformation of Aluminum	25
3.1 Crystalline structure	25
3.2 Elastic deformation	27
3.2.1 Elastic anisotropy in cubic crystals	27
3.2.2 Influence of crystal orientation on hardness and modulus: A literature review	28
3.2.3 Explicit approximation of the indentation modulus for anisotropic materials	28
3.3 Plastic deformation	30
3.3.1 Dislocation slip	30

3.3.2	Incipient plasticity and the pop-in effect	32
3.4	Strengthening mechanisms and their impact on the microstructure	34
3.4.1	Strengthening mechanisms	34
3.4.2	Strengthening-related microstructure	37
3.5	Recovery and recrystallization	39
4	Mechanical Modification of Aluminum Surfaces	41
4.1	Mechanically affected metallic surfaces	41
4.2	Mechanical and electrochemical polishing	42
4.3	Surface machining by micromilling	43
4.3.1	Effect of micromilling parameters on surface roughness	43
4.3.2	Strain hardening by micromilling	44
5	Materials and Methods	47
5.1	Raw materials	47
5.2	Material treatment	49
5.2.1	Recrystallization	49
5.2.2	Uniaxial compression	49
5.2.3	Micromilling	51
5.3	Sample preparation by polishing	52
5.4	Roughness analysis	56
5.4.1	Topography acquisition	56
5.4.2	Determination of the roughness parameters	57
5.5	Nanoindentation setup	58
5.5.1	Device installation and setup	58
5.5.2	Sample fixation	59
5.5.3	Berkovich and Vickers indenters	60
5.5.4	Area function calibration	60
5.5.5	Basic indentation procedure	61
5.5.6	Multi-step indentation	63
5.5.7	Pile-up and sink-in corrections	63
5.6	Data fitting	65
6	Influence of the Nanoindenter Setup and Sample Preparation	67
6.1	Introduction	67
6.2	Results	67
6.2.1	Surface quality	67
6.2.2	Influence of the nanoindenter	69
6.2.3	Indentation results on optimized sample geometry	70
6.3	Discussion	74
6.4	Conclusions	75

7	Impact of Relative Orientation of Indenter and Crystal Lattice	77
7.1	Introduction	77
7.2	Results	78
7.2.1	Quality of sample preparation and pile-up corrections	78
7.2.2	Influence of the crystal orientation	79
7.2.3	Influence of the indenter orientation	82
7.3	Discussion	87
7.4	Conclusions	89
8	Stress Induced Microstructures and Mechanical Properties of Polycrystalline Aluminum	91
8.1	Introduction	91
8.2	Results	92
8.2.1	Microstructure of compressively deformed polycrystalline aluminum	92
8.2.2	“Basic” indentation	94
8.2.3	Multi-step indentation	95
8.2.4	Review of the experimental setup	97
8.2.5	Influence of indenter geometry	100
8.3	Discussion	100
8.4	Conclusions	102
9	Mechanical Characterization of Micromilled AA6082	103
9.1	Introduction	103
9.2	Results	104
9.2.1	Tool geometry	104
9.2.2	Roughness of the machined surfaces	105
9.2.3	Depth dependent hardness of micromilled surfaces	107
9.2.4	Film-substrate-model fit	112
9.2.5	Evolution of indentation hardness of aluminum	112
9.3	Discussion	114
9.3.1	Indentation hardness evolution of aluminum	117
9.4	Conclusions	117
10	Summary and Outlook	119
	Appendices	123
A	Employed materials and their chemical composition	123
B	Devices and chemicals	125
C	Residual analysis of the fitted sine function	127
D	Depth-dependent hardness models: Fit parameters	129
	References	131
	Lebenslauf	151

Glossary

AFM atomic force microscope.

BSE back scattered electrons.

CRSS critically resolved shear stress.

FEM finite element method.

GND geometrically necessary dislocations.

ISE indentation size effect.

LMA Levenberg-Marquardt algorithm.

MD-tool mono crystalline diamond tool.

MEMS micro electro-mechanical Systems.

NLLS nonlinear least squares.

RSS residual sum of squares.

SC-tool solid carbide tool.

SDH sample down-holder.

SEM scanning electron microscopy.

UTS ultimate tensile strength.

Chapter 1

Introduction

Motivation

Since Richard P. Feynman declared that “there is plenty of room at the bottom” in his famous lecture in 1959, miniaturization became the driving force in many industry branches [21]. As originally proposed by Feynman, the information technology was the first and most successful industry to follow the trend. The current progress of miniaturization is best illustrated by the recent development of the 2-nanometer chip process [45]. One key technology for the production of small-scale metal components is micromilling. Conventional milling stands out by high production speed, flexibility and ability to produce complex three-dimensional structures. For micromilling, to take full advantage of these qualities on the micro-scale, deep understanding of the cutting process both on the tool and on the material side is indispensable.

Milling is a sophisticated technology with a solid knowledge base being built up over decades of research. However, it can not be easily transferred to micromilling. One reason is the micromilling size effect, also called the ploughing effect. It occurs when the length scale of the produced part is reduced to the micrometer size. In this case the critical tool dimensions (i.e. cutting edge radius, roughness), process parameters (i.e. uncut chip thickness) and the microstructural features of the milled material (e.g. grain boundaries, intermetallic phases) have comparable size. This leads, for example, to microstructural features that are considered insignificant for conventional machining to become game-changers on the microscale [88]. The interactions between these components are complex, which brings the milling process into a whole new regime, also rendering the experience on the macroscale obsolete.

Regarding the choice of materials, aluminum alloys are widely adopted for conventional milling because of many positive properties such as machinability, mechanical properties, corrosion resistance and low specific weight. Because of an excellent record in conventional machining, it is only sensible also to employ aluminum and its alloys for micromilling. Additionally, it is also extensively used for micro electro-mechanical Systems (MEMS) [64]. Therefore, it likely has the potential to fulfill the industry’s demands for the miniaturization

of metal components. For this reason, aluminum has attracted significant research interest in the last decades as a candidate material for micromilling applications.

For a comprehensive understanding of the micromilling process, it is important to characterize mechanical surface properties before and after micromilling. The intrinsic material properties and their variations on the microscale can significantly influence the cutting forces, and thus the micromilling process. To another end, the process parameters can influence mechanical properties of the produced surface, thus the performance of machined parts.

The influence of cutting speed, tool geometry, undeformed chip thickness (depth of cut per tool revolution) and other factors have already been investigated in previous studies. In most cases, the cutting force is the measured quantity as in the study on chip formation by Niu et al. [69]. However, this approach provides only indirect information on the effect of micromilling on the material. Alternatively, finite element method (FEM) simulations have also been utilized to estimate the mechanical influences on micromilled surfaces as in the study of Lai et al. [55]. However, a deep understanding of the material influence is still lacking.

To overcome this challenge, relevant microstructural features must be linked to mechanical properties on the adequate length scale. Characteristic material thickness, which is influenced by micro-milling, ranges between the lower micrometer to the upper nanometer scale. To measure mechanical properties on this length scale, dedicated tools and methods are required. The method of choice to measure small-scale mechanical material properties is nanoindentation which is a well-established method to determine local mechanical properties with resolution in the nanometer range. Nanoindentation can be applied to a large variety of materials and its suitability to characterize micromilled surfaces was previously demonstrated by Boehme et al. on austenitic stainless steel [9].

Objective

The objective of this thesis is to improve the fundamental understanding of plastic deformation and strengthening of aluminum during micromilling. To achieve this goal the influence of relevant microstructural features and processing steps on mechanical properties of aluminum have been investigated systematically. To acquire the necessary data, the number of contributing factors was increased systematically. At first, the influence of intrinsic material properties (i.a. lattice orientation) is studied on monocrystalline aluminum. Then the effect of strain hardening, texturization and plastic flow was assessed on polycrystalline aluminum. Finally, the effect of micromilling on surface properties of an engineering AA6082 alloy was investigated. The focus of the present work was on the indentation hardness and modulus of the examined materials. However, the research was augmented by characterization of microstructure, roughness measurements and other investigations.

Structure

The thesis begins with the fundamental description of the nanoindentation technique in chapter 2. After a brief overview, the typical nanoindentation setup and common data analysis methods are presented. Also, the most important factors which can affect nanoindentation results are discussed including nanoindentation of thin-films. To provide the necessary theoretical background selected metallurgical topics which are relevant to small-scale mechanical testing, are presented in chapter 3. Especially, the basics of elastic anisotropy, plastic deformation mechanisms, in particular dislocation slip, as well as relevant strengthening techniques and their effect on the microstructure are discussed. The mechanical modification of aluminum surfaces and the impact on mechanical properties are described in chapter 4. Here, the general structure of mechanically affected surfaces and the potential effects of electropolishing are presented along with the basics of micromilling.

After introducing the necessary basics, deployed materials and methods are summarized in chapter 5. The parameters of thermal and mechanical processing of the material (recrystallization, compression, micromilling), sample preparation (electropolishing) and analysis methods (roughness analysis, nanoindentation and data fitting) are provided in section 5.2. The primary instrument for mechanical investigations in this thesis was the nanoindenter. For this reason, a comprehensive description of the respective experimental setup, applied methods and parameters are presented in section 5.5. Prior to the actual experiments, the potential influences of sample preparation and the experimental setup were analyzed, and the achieved results are provided in chapter 6.

In the first stage of the analysis micro-mechanical properties of monocrystalline aluminum are obtained by nanoindentation. Two influencing factors on indentation hardness and modulus are examined: crystal anisotropy as well as the combined effect of indenter geometry and crystal symmetry. Both effects are quantified and the results are presented in chapter 7. In the next step the influence of strain-hardening and microstructural evolution due to uniaxial compression on micromechanical properties of pure polycrystalline aluminum in different deformation-states are investigated. Results indicating the nature of microstructural evolution and dynamic recovery are presented in chapter 8. In the next step micro-milled AA6082 surfaces were examined and the results are presented in chapter 9. Especially, the effects of tool geometry and tooth feed (i.e. thickness of the removed layer) on roughness and strain-hardening of the machined surface were investigated. The results are particularly relevant as they establish a link between the single microstructural constituents, strain hardening via micromilling and the mechanical properties of the machined surface. The thesis is concluded by a brief summary of the results in chapter 10.

Chapter 2

Basics of Nanoindentation

In this chapter it is first demonstrated how nanoindentation has developed from traditional indentation hardness techniques. Then the general nanoindentation technique is described including the commonly used measurement procedure, data analysis models and factors potentially affecting the measurements. The chapter is concluded by the special case of hardness and modulus determination of thin films and strain hardened layers by nanoindentation.

2.1 Historical development of the hardness test

There are numerous methods to determine mechanical properties of materials. Concerning material testing on small-scale, one of the most important methods is nanoindentation. It is a modern mechanical testing method by which it is possible to measure hardness and other mechanical properties on the nano-scale with high precision and repeatability. Although, comparison of materials by hardness is an ancient method¹, the technological use of the hardness test is relatively new. One of the first scientists to systematize relative hardness of different materials (especially minerals) was probably a German-Austrian geologist and mineralogist Friedrich Mohs (1773-1893). He ordered different minerals according to their relative scratch resistance. The Mohs' method proved to be practical to characterize minerals, but not for technological use [3].

In 1900, a Swedish engineer Johan August Brinell proposed a different hardness test. According to his method, the specimen surface is impressed with a hard metal ball at fixed load. After the load is released, the impression area is measured to determine hardness defined at load per area. The main advantage of the Brinell hardness in comparison to Mohs is that Brinell hardness is proportional to the ultimate tensile strength (UTS), which

¹“The method for comparing different materials (especially minerals) by their relative scratching resistance is of great antiquity. The method was mentioned by Theophrastus in his treatise “On Stones”, c. 300 BC., followed by Pliny the Elder in his “Naturalis Historia”, c. AD 77”, by Wikipedia https://en.wikipedia.org/wiki/Mohs_scale_of_mineral_hardness (accessed 9.11.2020, 23:36)

is a technologically highly relevant parameter. Therefore, the method enjoyed very broad acceptance and is used until today.

There are two major limitations of the Brinell hardness regarding its technological use: the inability to measure hard materials and the large distances required between single impressions to avoid mutual influence. To overcome the limitations of the Brinell method, the Vickers hardness test was presented by Robert L. Smith and George E. Sandland from Vickers Ltd. in 1922 [85]. As an improvement over Brinell, they introduced a sharp diamond pyramid indenter with well-defined geometry. This addressed both limitations of the Brinells method and allowed to test hard materials due to extremely hard indenter material and also to reduce the distance between the indents due to its sharp geometry. According to Vickers and Brinell, hardness H is the ratio of load P and the projected area A of the residual indent:

$$H = \frac{P}{A} \quad (2.1)$$

Brinell and Vickers methods describe only plastic resistance of the material to indentation by a rigid body, since A is measured after unloading.

A recent approach to hardness measurement is the instrumented indentation test. Analogous to prior methods, the sample is impressed with a rigid indenter of defined geometry. In contrast to conventional hardness tests mentioned above, load and indentation depth are recorded continually while the load is applied and released. The load-depth curve is the principal result of the measurement from which the material parameters are derived. The resulting hardness value HM is referred to as ‘‘Martens Hardness’’ after a German metallurgist A. Martens². HM is determined by calculating the surface area of the indenter A_s at contact depth under load P as follows:

$$HM = \frac{P}{A_s(h)} \quad (2.2)$$

In contrast to both Brinell and Vickers hardness, HM includes the elastic and plastic resistance to indentatio, since it is determined under load. The area A_s is derived from the tip geometry at maximum load based on the measured depth h and the indenter geometry, relying on models of contact mechanics. Microscopical determination of the indentation area is time consuming and erroneous due to the human factor. Therefore, instrumented indentation opened a completely new field in terms of measurement accuracy, speed and test automation.

²Adolf Karl Gottfried Martens (1850-1914) was a German metallurgist, who made a major contribution to materials engineering especially mechanical testing. The martensite crystalline structure is also named after A. Martens.

2.2 The nanoindentation experiment

Nanoindentation is a miniaturization of the instrumented indentation method in terms of instrumentation as well as a substantial refinement of the underlying contact mechanical models. Both, the instrument and the models are optimized for measurement at low indentation depths and high spatial resolution. A typical nanoindenter instrument consists of a table for holding the sample and the indenter head arranged in the typical “C”-configuration (Figure 2.1). The indenter head contains the indenter probe (i.e. a diamond pyramid), the transducers for load application and measurement as well as the displacement measurement modules.

The basic procedure is identical for all instrumented indentation methods. After the indenter head is positioned above the sample, which is firmly attached to the measurement table, the indenter is moved shock-free towards the specimen surface. The actual measurement procedure consists of four principal phases during which load and depth are recorded continuously:

1. Load increase: The load is increased up to a defined maximum value P_{max} in a controlled manner (load controlled or displacement controlled). P_{max} is applied during the load time t_{load} . Even though most experiments are load-controlled however, a displacement-controlled approach is also possible on more sophisticated systems.
2. Hold period at P_{max} : At P_{max} an optional hold-phase can be introduced where load is then kept constant for t_{hold} . The procedure with an included hold-phase is shown as the blue curve in Figure 2.2 (a) and (b).
3. Unload: P is lowered down to P_{min} . This step is characterized by the load-removal time t_{unload} which is usually equal to t_{load} .
4. Hold period at P_{min} : An optional hold period typically at $P_{min} = 0.05 \cdot P_{max}$ can be included in the measurement to characterize thermal drift.

Once the procedure is finished, the indenter is retracted from the sample surface. The measurement sequence is shown schematically as a time-load diagram along-side with the resulting load-depth in Figure 2.2.

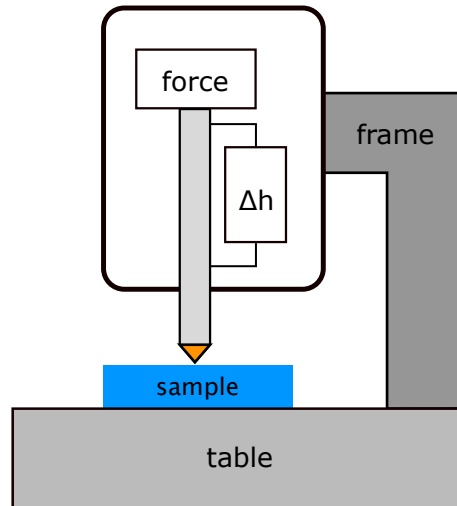


Figure 2.1: Scheme of a typical nanoindenter in the ‘C’-configuration. All components including the sample, indenter and the C-shaped device frame contribute to the compliance of the system. This setup differs from the Fischer ‘Picodentor HM500’ device configuration shown in Figure 5.7.

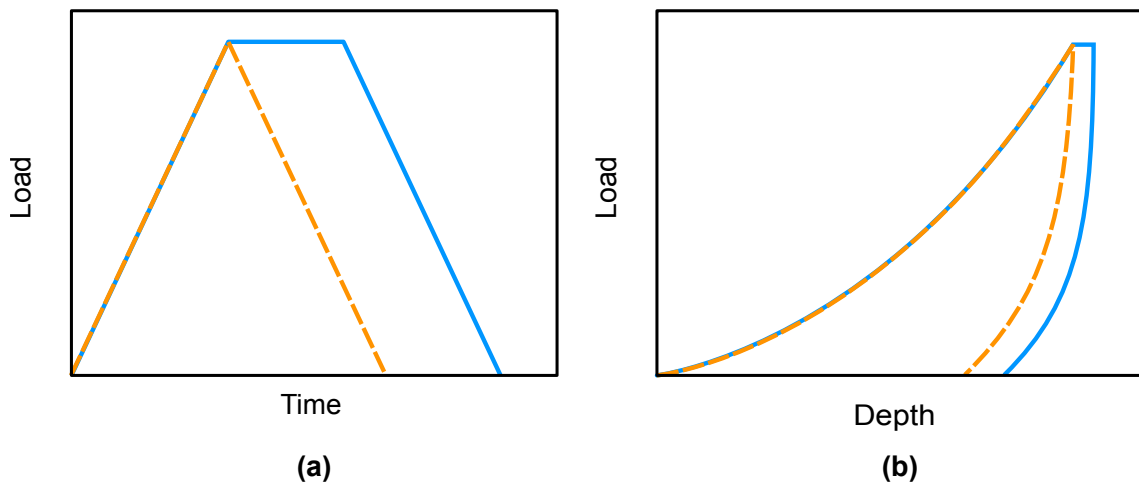


Figure 2.2: Basic procedure of a nanoindentation experiment. (a) Schematic indentation load-time curves. Basic indentation procedure including a load and unload phase (orange). The procedure can be extended with an additional hold period at maximum load (blue). (b) Load-depth curves resulting from the load-time curves in (a). Basic indentation procedure including a load and unload phase (orange dashed line) and the procedure modified with the hold period (blue line).

2.3 Data analysis

The load-depth curve shown schematically in Figure 2.2 (b) is the direct result of the nanoindentation measurement and contains the deformation response of the analyzed material to load. The curve is analyzed to derive desired mechanical properties (usually hardness and modulus). The nature of the mechanical contact between the indenter and the material surface is complex. Therefore, appropriate models of contact mechanics must be applied to extract the material properties. The most common method for interpretation of the load-depth curves is the Oliver-Pharr method [71] which is also a recognized standard and is described in the normative DIN EN ISO 14577. To extract the material properties with this method, besides the indentation curve, exact knowledge of geometry and material of the indenter probe is necessary. With this information at hand the indentation hardness H_{IT} , modulus M and other material properties are derived directly from the load-depth curve. The optical analysis of the impression by the operator, which is prone to errors, is thus eliminated. The basics of the indentation data analysis necessary to extract the material parameters from the indentation the load-depth curves are described in the following.

The first parameter to be determined from the load-depth curve is the projected area A_p . It is defined as the cross-sectional area of the indenter at contact depth h_c shown in Figure 2.3. h_c is estimated from the unload part of the load-depth curve shown in Figure 2.4). According to Oliver-Pharr method, the unload part of the curve can be described with the following power-law [71]:

$$P = \alpha(h_{max} - h_f)^m \quad (2.3)$$

with α and m being constants and h_f the residual depth after load removal (Figure 2.3). To deduce α , m and h_f the power-law from equation (2.3) is fitted numerically to the experimental data.

The contact stiffness S is the slope of the unload-part of the load-depth curve at maximum indentation depth h_{max} (Figure 2.4)). It is determined from the first derivative of the power-law from equation (2.3) resulting in:

$$S = S \left(\frac{dF}{dh} \right)_{h=h_{max}} = \alpha m (h_{max} - h_f)^{(m-1)} \quad (2.4)$$

Furthermore, the contact depth h_c at maximum load is determined according to the following relation:

$$h_c = h_{max} - \varepsilon \cdot \frac{P_{max}}{S \left(\frac{dF}{dh} \right)_{h=h_{max}}} \quad (2.5)$$

The geometry factor ε , as derived from a paraboloid, corresponds to $\varepsilon = 0.75$. According to the more recent analysis of the effective indenter shape ε is expected to vary between 0.74 and 0.79 with an average value of 0.76. Thus, the ε based on paraboloid indenter geometry is a reasonable approximation [72].

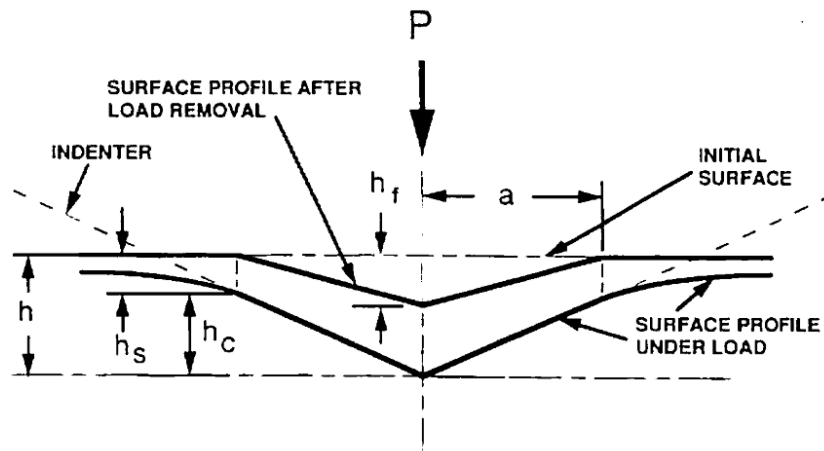


Figure 2.3: Schematic cross-sectional view on the indented surface under load and after load removal. The indentation depth h is the maximum vertical displacement of the indenter during indentation. The contact height h_c is the depth at which the indenter has actual contact with the sample surface. After load removal, the depth of the remaining impression is the residual depth h_f . h_s is merely the difference between h and h_c . Figure from [71], reproduced with permission from Springer Nature.

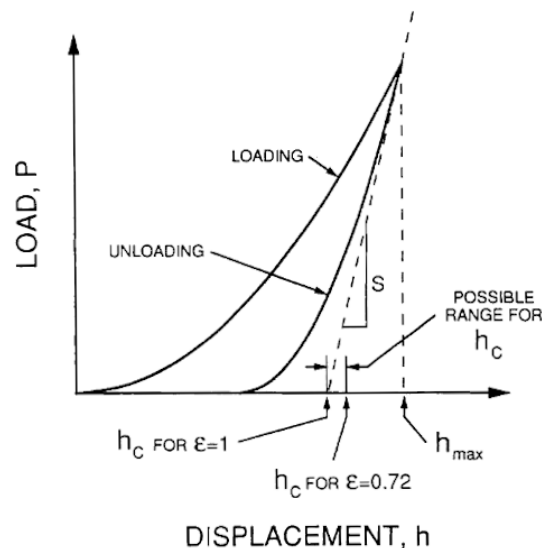


Figure 2.4: Scheme of a load-depth curve with the most important indentation parameters of the Oliver-Pharr analysis. Here, the difference between maximum indentation depth h_{max} and the contact depth h_c is notable. Figure from [71], reproduced with permission from Springer Nature.

The projected area at a given contact height $A_p(h_c)$ is derived from the indenter geometry by simple geometric considerations. For Berkovich and Vickers indenters (three and four-sided pyramid respectively, with identical area function) the area function can be formulated in the short form as:

$$A_p(h_c) = 24.5 \cdot h_c^2 \quad (2.6)$$

Due to elastic deformation, the contact height h_c is different from the maximum indentation depth h_{max} as illustrated in Figure 2.3. To determine A_p at the correct height, the h_c from equation (2.5) is substituted in equation 2.6:

$$A_p = 24.5 \cdot \left(h_{max} - \varepsilon \frac{P_{max}}{S \left(\frac{dP}{dh} \right)_{h=h_{max}}} \right)^2 \quad (2.7)$$

H_{IT} is defined as the quotient of maximum load P_{max} and the projected area A_p at the contact height h_c :

$$H_{IT} = \frac{P_{max}}{A_p(h_c)} \quad (2.8)$$

This expression is indeed very similar to the definition of the Martens, Brinell and Vickers hardness which are also defined as the quotient of load and loaded area. By contrast, the elastic properties of the indented specimen are derived based on the contact stiffness S . For a rotationally symmetric indenter geometry the analysis is based on the so-called Sneddon-Equation [86, 71]:

$$S = \frac{\delta P}{\delta h} = \frac{2E_r \sqrt{A_p(h)}}{\sqrt{\pi}} \quad (2.9)$$

The specimen surface and the indenter are both deformed elastically during indentation and thus contribute to the contact compliance resulting in a reduced modulus. Hence, the reduced modulus E_r can be described based on the Poisson's ratio ν , the Young's modulus of the sample, the Poisson's ratio of the indenter material ν_i and Young's modulus of the indenter material E_i as follows:

$$\frac{1}{E_r} = \frac{1 - \nu^2}{E} + \frac{1 - \nu_i^2}{E_i} \quad (2.10)$$

Determining Young's modulus of anisotropic materials via nanoindentation is challenging. The reason is that ν of the specimen is also anisotropic and cannot be determined separately for each indentation direction. Additionally, the indentation direction in respect to the sample orientation must also be known exactly. To eliminate these difficulties, the ν -independent indentation modulus M is introduced. To calculate M the equation (2.10) is resolved for $M = E/(1 - \nu^2)$:

$$M = \frac{E}{1 - \nu^2} = \left(\frac{1}{E_r} - \frac{1 - \nu_i^2}{E_i} \right)^{-1} \quad (2.11)$$

Solving the equation (2.9) for E_r and inserting the result into equation (2.11) provides an overall formula for M :

$$M = \left(\frac{2\sqrt{A_p(h_c)}}{\sqrt{\pi}S} - \frac{1 - \nu_i^2}{E_i} \right)^{-1} \quad (2.12)$$

Using this formula, M can be determined directly from the load-depth curve. The values for E_i and ν_i of the diamond-indenter are provided by the ISO14577 and parameters from reference [49] ($E_i = 1140$ GPa, $\nu_i = 0.07$).

2.4 Influencing factors

There are many factors influencing indentation results in different ways. Anthony C. Fischer-Cripps summarized these factors bellow [28]. Some of these factors are discussed in more detail in the next sections (marked with an asterisk*):

- Instrument compliance (section 2.4.1)*
- Indenter geometry and tip rounding (section 2.4.2)*
- Piling-up and sinking-in (section 2.4.3)*
- Indentation size effect (section 2.4.4)*
- Surface roughness (section 2.4.5)*
- Substrate influence (section 2.5)*
- Specimen preparation(section 4.1)*
- The plastic depth
- Residual stress
- Friction and adhesion
- Thermal Drift
- Initial penetration depth

2.4.1 Instrument compliance

All parts of the indentation system including the sample, the indenter and the device frame undergo elastic deformation during the measurement. The deflection of the entire system dh^* is registered by the displacement measurement module. The contact stiffness is derived from the slope of the unload-part of the load-depth curve as $S = dP/dh$. Its accurate determination is problematic because the measured dh^* is the deflection of the entire system which also includes the frame stiffness. In the actual experiment it is desired to determine dh exclusively originating from the sample-indenter interaction. Therefore, it has to be deconvoluted properly from the measured deflection that includes device specific contributions.

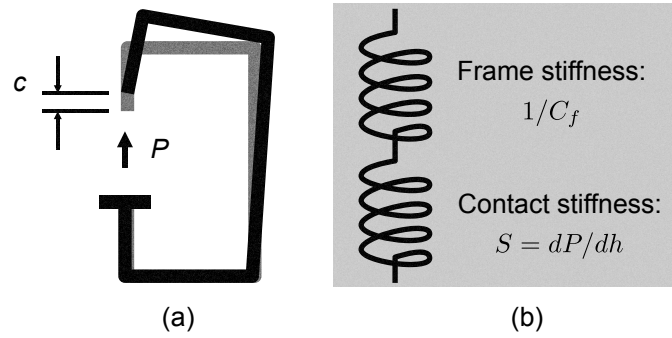


Figure 2.5: (a) Illustration of the C-type indenter frame. The initial geometry of the indenter frame is shown in gray. After applying the load P to the sample, the frame is also deformed elastically (black shape). The difference between both states is the deflection c . (b) Spring-model of the system stiffness. The frame and the contact stiffness are modeled as two springs in series. Figure based on [28].

Due to the applied load P the device frame is deflected by the distance c as shown schematically in Figure 2.5 (a). The indenter-specimen contact and the device frame can be modeled as two spring in series (Figure 2.5 (b)). Accordingly, the equivalent system compliance C_{eq} corresponds to the sum of the contact compliance C_c and the device frame compliance C_f :

$$C_{eq} = C_c + C_f \quad (2.13)$$

The equivalent compliance is defined as $C_{eq} = dh^*/dP$ and the contact compliance as $1/S$. Thus, according to Fischer-Cripps [28] the equation can be written in the following form:

$$\frac{dh}{dP} = \frac{1}{S} + C_f \quad (2.14)$$

The desired S is obtained by measuring C_f as a function of load on an infinitely stiff sample (either without the indenter or with a flat punch). Then S is obtained by subtracting C_f from the measured dh/dP :

$$\frac{1}{S} = \frac{dh}{dP} - C_f \quad (2.15)$$

This is especially important for devices with a C-type frame as shown in Figure 2.1 that usually exhibit significant frame compliance. The nanoindentation device used for the present thesis is optimized to minimize frame compliance on the hardware side. Its exact operating principle is further described in section 5.5.2.

2.4.2 Indenter geometry

One of the prerequisites for nanoindentation data analysis is exact knowledge of the indenter geometry. Standardized indenters have been introduced to the market to assure reproducible results on different systems. The most common sharp diamond indenters are the Vickers and the Berkovich indenter.

The Vickers indenter is a four-sided square pyramid as shown in Figure 2.6. Owing to the four-sided geometry it is difficult to maintain the self-similar geometry at the indenter tip. The apex is often edged and not pointed, and also subject to significant rounding. Indenters with tip radii in the range of 500 nm are commonly available.

The Berkovich indenter with a three-sided pyramid (Figure 2.6) was designed to have the same area function (projected area at certain depth) as the Vickers indenter. This is practical since the same indentation depth results in almost identical contact area for both indenter types. Since the Berkovich indenter can be produced with a much smaller tip radii (< 100 nm) than the Vickers indenter, it is widely adopted for nanoindentation.

The geometry-derived area-functions of standard indenters (Berkovich, Vickers, cube-corner, etc.) are well known and can be found in the literature [27]. However, the indenter tip shape can deviate significantly from the designed shape, especially on the nano-scale (compare Figure 2.7 (a) and (b)). In addition to the limits of the manufacturing process the indenter tip is also blunted in the course of use due to tip wear. The exact knowledge of the indenter tip geometry is particularly important for measurements at low depths since the sample is penetrated with the blunted indenter tip and not the pyramidal indenter body. The actual contact area is then larger than proposed by the area function due to tip rounding.

Usually, an atomic force microscope (AFM) image of the tip is made on delivery from which the tip radius R is determined. To improve the accuracy of area determination, the tip can be modeled with a sphere-conical geometry (Figure 2.7 (c)). Consequently, the area-function consists of two parts. The indenter tip is modeled as a sphere with the AFM-determined radius R and the indenter body is derived from its ideal geometry (i.e. Berkovich pyramid).

To account for tip wear, R must be redetermined regularly. This is not trivial as the indenter has to be unmounted from the indenter system for the AFM-measurement which

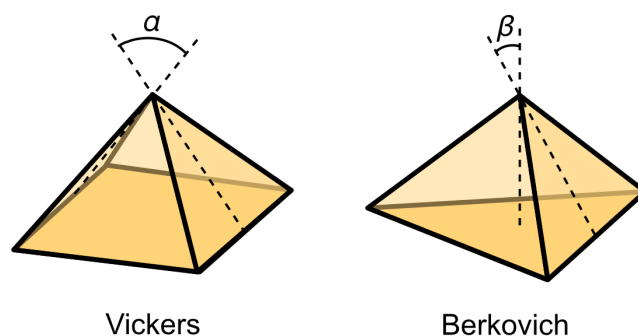


Figure 2.6: Specifications of the employed indenters according to the DIN EN ISO 14577-2. The Vickers indenter (left) is based on a regular square pyramid with $\alpha = 136^\circ \pm 0.3^\circ$ (angle between opposite lateral faces). The Berkovich indenter (right) is based on a tetrahedron with $\beta = 65^\circ \pm 0.3^\circ$ (angle between the center line and a lateral face).

is a significant downside. A more robust approach is to determine the individual tip area function by indentation on a reference material. For this purpose H or E is measured as a function of depth. The achieved depth-dependent values are compared to the known properties of the reference material. Deviations from the known value are attributed to the differences in contact area. The so derived empiric area function is determined by resolving the respective H or E equations of the Oliver-Pharr method for A_p which is then determined as a function of depth. Fused silica is usually used as a reference material. It's hardness and modulus are independent from indentation depth and indenter-orientation (amorphous isotropic material). The calibration procedure utilized in this work is described in section 5.5.4.

2.4.3 Piling-up and sinking-in

In an indentation experiment, a certain volume of the material is displaced and pushed away from the indenter. There are two possibilities, how the displaced material is accom-

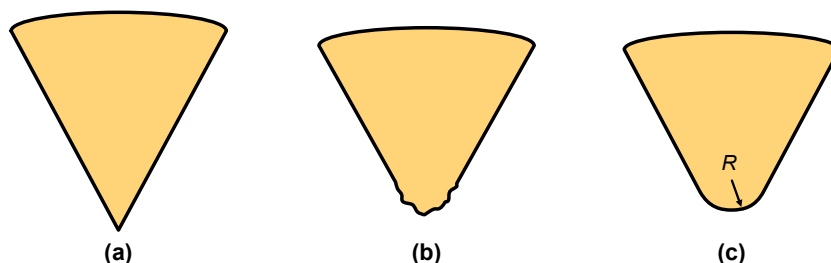


Figure 2.7: Schematic depiction of the indenter tip shape (a) Ideal indenter tip. (b) Actual indenter shape (exact geometry is usually inaccessible). (c) The indenter is modeled as a cone with a spherical tip with radius R (sufficient for most experiments).

modated within the bulk. The material is either pushed downwards, creating a sink-in, or bulges around the indenter creating a pile-up (Figure 2.8). Whether a sink-in or a pile-up is produced depends in metals on the strain-hardening rate of the indented material [66]. Annealed metals demonstrate high strain-hardening rates. Indentation on these materials causes significant strain-hardening in the proximity of the indenter. During the indentation process, plastic deformation propagates continually from the indenter towards bulk, thus resulting in a sink-in. Pronounced sinking-in leads to actual contact area A_c being smaller than the indenter cross-sectional area $A_p(h_c)$ (Figure 2.8). Thus, according to equation (2.8) and equation (2.12) the so determined properties H_{IT} and M are underestimated. Strain-hardened materials and metallic glasses show low strain-hardening rates upon indentation. Plastic deformation takes place in the near-field around the indenter producing a pile-up. A_c then is larger than the indenter cross-sectional area $A_p(h_c)$. (Figure 2.8). Consequently, H_{IT} and M are overestimated according to equation (2.8) and equation (2.12). The effects of the pile-up and sink-in on the derived material parameters are summarized in Figure 2.8.

In addition, the exact plastic flow depends on the slip-system configuration of the indented material [77], the crystallographic orientation of the single crystal or grain, the geometry and azimuthal orientation of the indenter. This is especially critical for indentation of ductile crystalline materials such as Au, Cu or Al. Because of the pronounced anisotropy of plastic flow and distinct differences in the strain-hardening rate of aluminum, derivation of the contact area due to pile-up should be carefully considered. For severe deviations the contact area must be corrected. There are different correction schemes as summarized by Guillonneau et al. [40]. The procedures chosen to determine true projected areas are described in section 5.5.7.

2.4.4 Indentation size effect

Hardness of various materials is often observed to increase with decreasing indentation depth. This is counter-intuitive, especially for homogeneous isotropic materials. Gane and Cox for example reported in 1970, that indentation hardness of Au single crystals increases threefold when the diameter of an approximately round contact area is decreased from 10 μm to 100 nm [31]. This effect is commonly known as the indentation size effect (ISE). The length scale on which the ISE is observed lies in the nanometer-range. This is evident from the work of Stelmashenko et al. on tungsten-molybdenum single crystals, where they showed a significant hardness increase for indent diagonals below one micrometer [87]. There are different interpretations of the ISE, which are comprehensively reviewed by Gerberich et al. [35]. One of the most important scientific works on ISE regarding metals has been published by W. D. Nix and H. Gao [70]. In this paper they applied strain gradient plasticity analysis to explain the ISE.

According to different authors, the physical explanation of ISE for metals originates from large strain gradients that are inherent in small indentations [29, 87, 83]. These gradients lead to geometrically necessary dislocations (GND) that cause enhanced strain hardening. According to Gao GND “represent extra storage of dislocations required

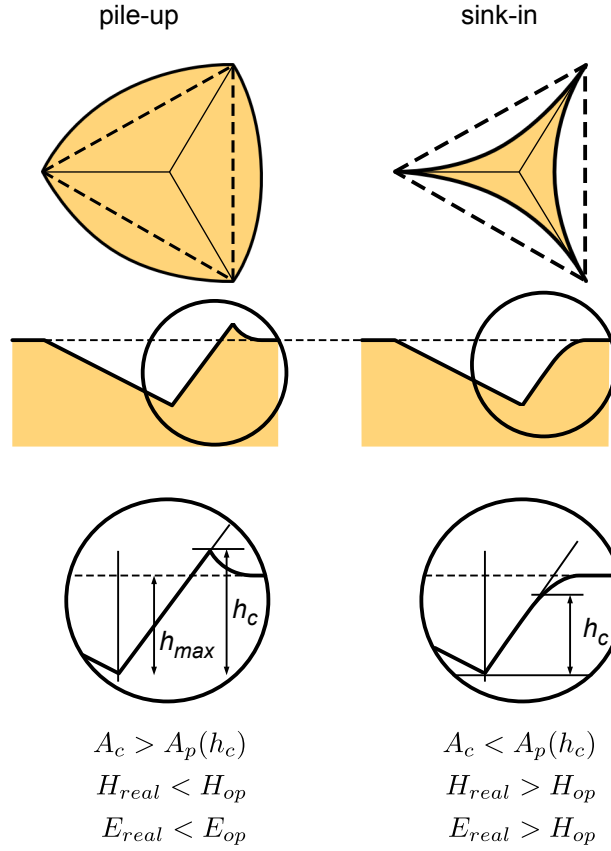


Figure 2.8: Schematic depiction of the pile-up and sink-in effect with a Berkovich indenter (three-sided pyramid), and their implications on indentation hardness and modulus calculated according to the Oliver-Pharr method.[28]

to accommodate the lattice curvature that arises whenever there is non-uniform plastic deformation.”[32] In terms of nanoindentation, this means that GND are produced by pushing the displaced material towards bulk in the form of extra planes of atoms in the original atomic lattice which produce GND. These extra dislocations do not contribute directly to plastic strain, but are effective obstacles for the motion of statistically stored dislocations. Since the concentration of GND relative to the volume of the plastic zone beneath the indenter is increasing with decreasing indentation size, depth-dependent hardening or ISE is observed [32]. According to Nix and Gao it is possible to accurately describe the hardness-depth data of crystalline materials with significant ISE by the following equation [70]:

$$\frac{H}{H_0} = \sqrt{1 + \frac{h^*}{h}} \quad (2.16)$$

Here H is the indentation hardness, h the indentation depth, H_0 the bulk hardness (i.e. hardness at large indentation depth) and h^* the characteristic length which depends on the indenter shape, shear modulus of the material and H_0 .

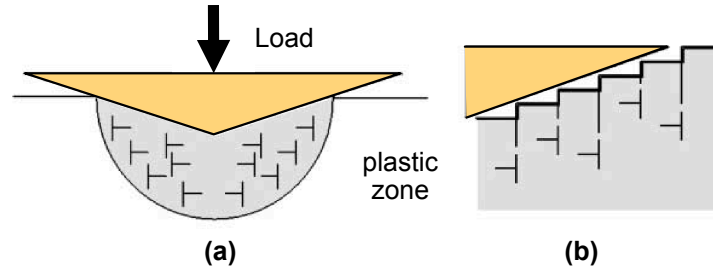


Figure 2.9: Schematic depiction of GND underneath the indenter tip. **(a)** The material beneath the indenter is pushed into the bulk, resulting in the creation of additional defects (plastic zone). **(b)** On small scale atomic steps are produced on the deformed surface. Each step is associated with a single GND. Figure based on [70].

2.4.5 Surface roughness

The presented approach to evaluate the indentation data anticipates an absolutely smooth surface. However, this condition cannot be fulfilled for most real surfaces. To achieve reliable indentation results, the height variations of the surface must be accounted for. To better understand the underlying contact mechanics between the indenter and rough surface two cases are especially important. Figure 2.10 (a) shows the case, where the indenter diameter is significantly larger than the average vertical distance between peaks and valleys (indentation with a blunt indenter, low roughness of the specimen). The indenter comes in contact with the roughness peaks only. For this reason the actual contact area between the indenter and the surface (red in Figure 2.10 (b)) is smaller than on an ideally surface. Hence, according to equation (2.8) indentation hardness is overestimated. This is critical for low indentation depths, where the surface roughness has not yet been smoothed out by the indenter. In the case that the indenter tip radius is in the same order of magnitude as the height variations (indentation with a sharp indenter, high roughness), additional scenarios must be distinguished as shown in Figure 2.11: the indentation is placed either on a roughness peak (a), a flank (b), or a valley (c). The effect of each case on the indentation results is further discussed by Böhme et al. [9].

The impact of these effects on the uncertainty of the measured contact area is considered by the DIN EN ISO 14577. It is assumed to be negligible when the indentation depth is significantly higher than surface roughness. In order to keep the uncertainty of the determination of the contact area below 5%, the following condition for the maximum indentation depth h_{max} in relation to the arithmetical mean roughness R_a (equation (5.1)) is proposed:

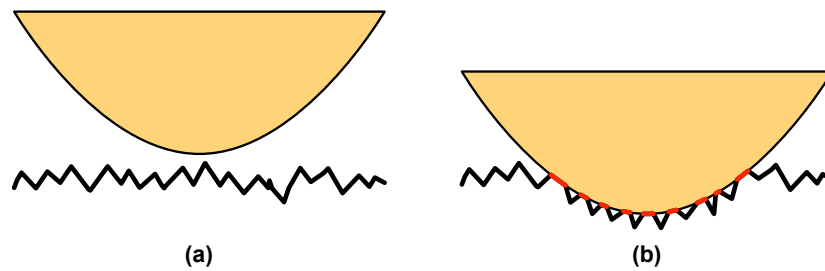


Figure 2.10: Principal indentation with a blunt indenter (i.e. spherical tip) on a rough surface. The actual contact area (red) between the indenter and the surface is lowered due to surface roughness.

$$h_{\max} \geq 20 \cdot R_a \quad (2.17)$$

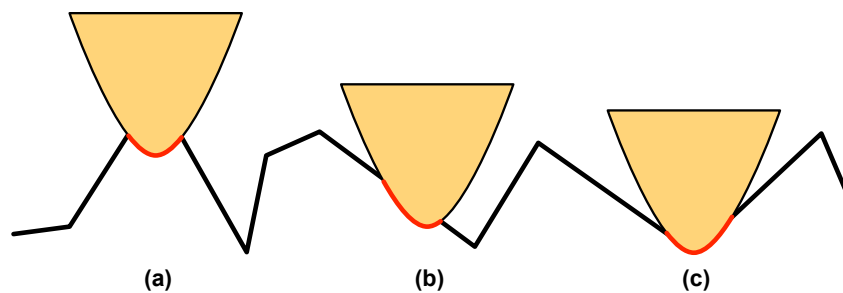


Figure 2.11: Indentation with a sharp indenter (i.e. Berkovich) on a rough surface. The actual contact area, hence indentation hardness depends on the indent position: **(a)** Roughness peak: hardness is underestimated. **(b)** Flank: hardness depends on the flank slope. **(c)** Valley: hardness is overestimated. Figure based on [9]

2.5 Thin film hardness

Determination of mechanical properties of thin films is one of the most prominent nanoindentation applications. For example, it is of significant interest for the investigation of mechanical properties for MEMS or tribological coatings. The configuration of a test layer system usually consists of a thin film and a substrate. Both have different hardness and are separated by an interface. An indentation of such a film-substrate system is schematically shown in Figure 2.12. Both the film and the substrate contribute to the resulting effective hardness while the proportion of each contribution depends significantly on the indentation depth. Indentation hardness measured at a certain indentation depth is an averaged value

from the stress field below the indenter. This stress field develops according to the applied stress, indenter shape and material's anisotropy [20].

The principal depth-dependency of hardness for an exemplary coating system (hard film on a soft substrate) is presented in Figure 2.13. With increasing load the indenter penetrates gradually through the film. At low indentation depth hardness is dominated by the film (Figure 2.13 (a)). That is because the stress-field beneath the indenter is completely accommodated within the film. As the indenter continually penetrates the film, the stress-field below the indenter exceeds film thickness and protrudes into the substrate. Accordingly, the measured hardness begins to decrease due to the influence of the soft substrate (Figure 2.13 (b)). For indentation depths significantly higher than film thickness (Figure 2.13 (c)) the results are dominated by the substrate.[10]

The described depth dependence is problematic, since in most cases the mechanical properties of the substrate must be known independently from the film. In the following, two common approaches are presented by which the film's mechanical properties obtained by nanoindentation can be separated from the substrate. The first most straightforward approach is to decrease the indentation depth to a certain value at which the stress-field below the indenter is completely accommodated within the film. An alternative approach is to produce a series of measurements with variable depth to analyze the depth-dependent behavior of the coating-system. The mechanical properties of the film can be extracted from these data by application of appropriate film-substrate models.[28]

2.5.1 Bückle's rule

The film hardness H_f can be separated from the substrate hardness H_s by reducing the applied load to a value where the substrate influence becomes negligible (film-dominated regime as shown in Figure 2.13 (a)). To achieve this, the maximum load and the resulting indentation depth of the film-dominated region must be specified. This has been done by Bückle who elaborated a model that describes the effective hardness of film-substrate systems in relation to indentation depth [11]:

$$H_{eff} = \alpha H_f + (1 - \alpha) H_s \quad (2.18)$$

with the effective hardness H_{eff} (also called the composite hardness corresponding to the measured value). The coefficient α depends on the indentation depth h , film thickness t and transition range Δt as follows:

$$\alpha = \left[1 - \frac{\exp(h - t)}{\Delta t} \right]^{-1} \quad (2.19)$$

From these equations the well-known Bückle's 1/10-rule is derived. Accordingly, to avoid substrate influence for a given t the maximum indentation depth h_{max} must be less than $t \cdot 1/10$. This empiric relation was confirmed for various materials. This rule can be used to effectively constrain the indentation depth to a certain value depending on the film thickness. However, thickness of the film must be known for this approach. It must also

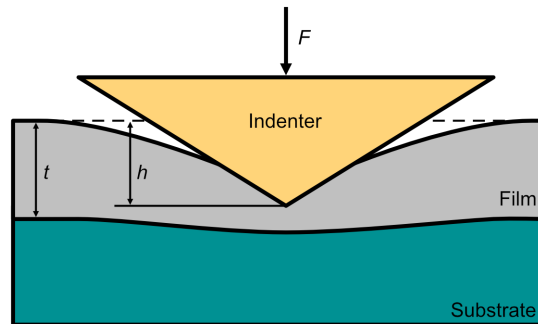


Figure 2.12: Scheme of an indentation of a film-substrate system with a sharp indenter. The substrate influence on measured hardness depends on the film thickness t and indentation depth h . Figure adapted from [10]

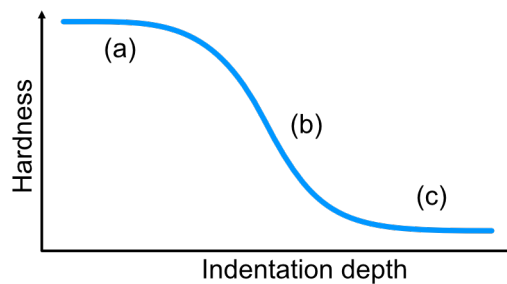


Figure 2.13: Anticipated hardness-depth curve of an indentation through a film-substrate system (hard film, soft substrate). **(a)** Film-dominated region (Indentation depth significantly lower than film thickness) **(b)** Transitional region (indentation depth in the range of film thickness). **(c)** Substrate-dominated region (Indentation depths exceeds film thickness significantly).

be mentioned, that the Bückle's rule applies only to sufficiently thick hard coatings with uniform hardness distribution. The determination of thin film hardness with this approach is therefore problematic.

2.5.2 Depth-dependent nanoindentation

Because of the limitations described above, a method to determine H_f for indentation in the transitional region shown in Figure 2.13 (b)) is needed. Bückle proposed a method to extract H_f for h being in the same range as t [12]. The downside of this approach is that both t and H_s must be known a priori or determined independently. While H_s can often be measured only after stripping the film from the substrate, it is often difficult or even impossible to determine t of thin or non-uniform films. Soft or very thin films pose additional difficulties since there are still significant substrate influences even for very low h .

One approach to mechanically characterize those thin-films solely by nanoindentation is to reproduce the curve from Figure 2.13 with experimental data. All three regions of the curve should be covered: coating-dominated, transitional and substrate-dominated region. If an appropriate model of depth-dependent mechanical behavior can be derived, the desired parameters can be extracted from the depth-hardness curve.

These curves can be acquired by the multi-step method where indentation is performed at a single location while load application is divided into multiple steps. Each step includes a load segment to an intermediate $F_{max,(i-1)}$, a partial unload step and is concluded with a subsequent load step to the next $F_{max,(i)}$. The procedure is repeated until the global F_{max} is reached after which the load is removed. Each segment for the resulting multi-step curve is analyzed separately to deduce the depth-dependent hardness.

2.5.3 Film-substrate models

To extract H_s , H_f and t from the experimental hardness-depth curves the effective hardness is modeled. Multiple approaches have been suggested to describe the hardness-depth behavior of film-substrate systems (compare Fischer-Cripps or Broitman for an extensive review of prevalent models [28, 10]).

Korsunsky model

Besides the capturing the essential physics of the analyzed system, the suitability of the model for numerical fits is important. For this reason the film-substrate model developed by Korsunsky, McGurk and Page [53] is of particular interest. Their indentation-energy-based model yields the following relationship of H_f and H_s :

$$H_{eff} = H_s + \frac{H_f - H_s}{1 + \frac{t}{\alpha} \left(\frac{h}{t}\right)^2} \quad (2.20)$$

In this equation α is a factor which describes film plasticity. The model actually reproduces the curve shape presented in Figure 2.13. It includes all necessary parameters (H_s, H_f, h, t) and is particularly well suited for numerical fits. This suitability of this model to determine H_f by means of numerical fit of the experimentally achieved partial depth-hardness curves has been demonstrated by Tuck et al. [92, 93].

Exponential model

Both the Bückle and the Korsunsky model assume the film to be uniformly hard with an abrupt hardness change at the interface. Accordingly, the fitted depth-hardness curves exhibit two pronounced hardness plateaus at small (H_f dominated) and large (H_s dominated) indentation depth [92, 93]. This assumption is hardly justified for thin strain-hardened surfaces produced by micro-machining which are investigated in chapter 9. Applied external stress, i.e. by micromilling, leads to strain-hardening of the surface. Since the stress decreases over depth a gradually strain-hardened zone is produced. The effective hardness achieved experimentally on such surfaces is expected to change gradually from $H_{eff,max}$ at minimum indentation depth (H_f) to a plateau at large indentation depth (H_s). To the best of our knowledge no appropriate model exists to describe such film-substrate system satisfactorily on the nano-scale. Our approach presented here is based on the assumption, that the hardness decreases exponentially with increasing indentation depth. This corresponds well to preliminary results (not shown here) and a simplified model of the strain hardened layer (Figure 4.1 in section 4.1). This is implemented in the following exponential equation:

$$H_{eff} = H_s + (H_f - H_s) \cdot e^{-h/m} \quad (2.21)$$

In contrast to the Korsunsky model, this equation includes no parameter for the film thickness, rather the factor m describes the hardness increase rate with decreasing indentation depth. Because of the low number of parameters and its exponential form this model is also well suitable for numeric fits.³

³Here, the assistance of Prof. Dr. A. Kersch, from Munich University of Applied Sciences is highly appreciated for the proposal of this model

Chapter 3

Elastic-Plastic Deformation of Aluminum

The mechanical response of the material measured by nanoindentation highly depends on its micro- and nanostructure. Insights into the underlying microstructure and the related deformation mechanisms are essential to understand the indentation results. In the following chapter, the atomic structure of aluminum is presented. The elastic anisotropy for cubic crystals and especially aluminum is calculated and the indentation modulus is estimated. With regard to plastic deformation on the atomic scale the dislocation slip mechanism is introduced, the slip-systems of the face centered cubic structure are discussed and the dislocation related pop-in effect is explained. Yet, microstructure of a technical alloy is significantly different from a pure material, because of the applied strengthening mechanisms. The strengthening-related microstructural features are described in view of their effect on the nanoindentation results. Selected strengthening methods in view of small scale mechanical testing conclude the chapter.

3.1 Crystalline structure

Under normal conditions¹metals form crystals with a periodic structure [77]. Aluminum is a third main group element which adopts face centered cubic (fcc) crystal structure (Figure 3.1) with a lattice parameter of 4.04 Å. It is possible to grow aluminum single crystals but technical aluminum or its alloys usually occur in polycrystalline form. A polycrystal consists of multiple differently oriented grains (i.e. single crystals or crystallites, Figure 3.2) the size and morphology of which depend mainly on the manufacturing process. Extensive rolling, for example, yields an elongated grain structure. For small scale mechanical testing the crystalline structure of the metal is important, since the sampled volume is comparable to the size of a single grain (every single grain is a single crystal).

¹It is possible to force metals into amorphous structures by hindering the diffusion resulting in metallic glasses with an amorphous structure and metallic characteristics at room temperature [47].

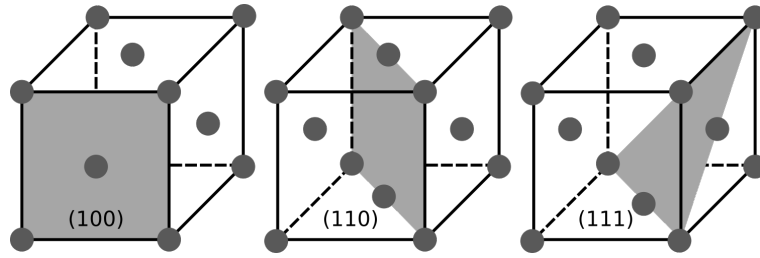


Figure 3.1: Face centered cubic crystal lattice with three major lattice planes (100) , (110) and (111) (grey areas).

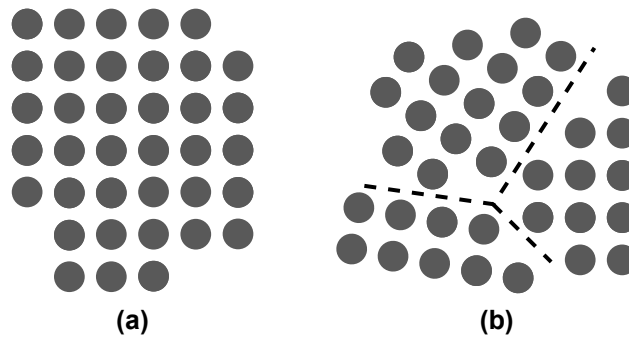


Figure 3.2: Illustration of two different possibilities (not inclusive) for arrangement of atoms in a metal. **(a)** Single crystal structure with a distinct orientation (extends to sample boundaries). **(b)** A polycrystal consisting of many differently orientated grains (single crystals) with identical lattice structure, separated by grain boundaries (dashed line).

When a metal is subjected to mechanical stress in a elastic or reversible manner, the atomic bonds are stretched until a new equilibrium position is reached. If the applied stress is increased beyond the threshold (yield stress), where the capacity of elastic deformation is not sufficient to relieve the applied stress, the atomic order changes permanently (plastic or irreversible deformation). The main mechanism for plastic deformation in aluminum by the movement and multiplication of dislocations. Alternative plastic deformation mechanisms such as deformation twinning, strain induced phase transformation or grain boundary sliding are of minor importance for aluminum at ambient conditions, thus not further discussed here.

3.2 Elastic deformation²

3.2.1 Elastic anisotropy in cubic crystals

The resistance of the material to elastic or reversible deformation (stretching of the atomic bonds) is usually characterized with the Young's modulus E . Young's modulus is defined by Hooke's law:

$$E = \frac{\sigma}{\varepsilon} \quad (3.1)$$

with the stress σ and strain ε . Since E mainly depends on the strength of the atomic bonds, it can have a pronounced dependence on the direction of the applied stress (crystal anisotropy). This can be described with the anisotropy factor A which depends on the crystal structure and the elastic constants C_{ij} :

$$A = \frac{C_{44}}{C_{11} - C_{12}} \quad (3.2)$$

For cubic crystals A can also be approximated from Young's moduli measured uniaxially (i.e. by tensile tests of single crystals) along $\langle 111 \rangle$ and $\langle 100 \rangle$:

$$A \approx \frac{E_{\langle 111 \rangle}}{E_{\langle 100 \rangle}} \quad (3.3)$$

A varies between 1 (isotropic) and 4 (highly anisotropic), while A for aluminum amounts to 1.23 [44]. Therefore, the dependence of the resistance to elastic deformation on the load direction relative to the crystal orientation should be considered. For single crystals E along $[uvw]$ can be calculated according to the following equation (Hooke's law for cubic crystals) [100, 77, 44, 46]:

$$\frac{1}{E_{[uvw]}} = S_{11} - [2(S_{11} - S_{12}) - S_{44}] (\alpha^2\beta^2 + \alpha^2\gamma^2 + \beta^2 + \gamma^2) \quad (3.4)$$

with $E_{[uvw]}$ being the Young's modulus in $[uvw]$ direction and α , β and γ the respective direction cosines. The coefficients of the compliance matrix S_{11} , S_{12} and S_{44} can be converted to the corresponding coefficients of the elasticity matrix, i.e. the elastic constants C_{11} , C_{12} , C_{44} as can be found in literature. Here, we utilized values also used by Vlassak and Nix [94] (originally provided by Simmons and Wang [84]) corresponding to $C_{11} = 107.3$ GPa, $C_{12} = 60.9$ GPa and $C_{44} = 28.3$ GPa. By this means, directional Young's Moduli $E_{[uvw]}$ for three major crystallographic orientations are calculated as $E_{100} = 63.2$ GPa, $E_{110} = 72.0$ GPa and $E_{111} = 75.6$ GPa.

²Parts of the following section are adapted from *Filippov, P.; Koch, U. Nanoindentation of Aluminum Single Crystals: Experimental Study on Influencing Factors. Materials (Basel). 2019, 12, 3688. [25]*

3.2.2 Influence of crystal orientation on hardness and modulus: A literature review

The influence of the crystallographic orientation on indentation hardness and modulus has been studied for different materials. It has been investigated on for polycrystalline austenitic steel by Hausild et al. [41] and titanium by Merson et al. [67]. Among face-centered cubic (fcc) metals, copper was studied in many aspects. Zahedi et al. [103] found the crystal orientation to have only a small effect on the indentation results; Geng et al. [34] analyzed the influence of crystallographic orientation with respect to nanoscratching behavior and Liu et al. [61] has investigated the plastic behavior of single crystalline copper by numerical simulation and experimentally (indentation with a spherical indenter). Although copper and aluminum both possess a fcc structure, it is impossible to directly compare results because of their different anisotropic ratios ($A_{Al} = 1.23$, $A_{Cu} = 3.22$, according to [77]).

Only few dedicated experimental studies on the indentation of aluminum single crystals were published. In their fundamental study, Vlassak and Nix [94] investigated elastic anisotropy of aluminum single crystals among other materials. Yet, their focus lay on mathematical modeling of the contact problem and the experimental results have no statistical basis. In a recent study Liu et al. [60] combined simulation with an experimental approach. Here, indentation results of Al single crystals are included but without a statistical analysis. Moreover, the absolute values and anisotropy published by Liu differ significantly from the results reported by Vlassak and Nix [94]. There are other studies on indentation of aluminum single crystals such as that by Kolor et al. [75], but these often demonstrate the indentation results of only one crystallographic orientation or are lacking statistical basis. Hence, no statistically reliable experimental data describing anisotropy of hardness and modulus for pure aluminum are available. These data were acquired in this thesis and can be found in chapter 7.

3.2.3 Explicit approximation of the indentation modulus for anisotropic materials

In contrast to the directional modulus shown in equation (3.4), nano-indentation with a sharp indenter is not a strictly unidirectional process. Instead, the measured mechanical properties are averaged over various directions depending on the crystal structure, elastic constants, load direction and the indenter geometry. This is related to as the nanoindentation averaging effect [36]. Therefore, the indentation modulus M can differ from the directional Young's modulus calculated for the indentation direction (equation (3.4)). The approximated anisotropy ratio based M (analogous to A from equation (3.3)) $A_{indentation}$ is lower than the A based on the directional Young's modulus. This can be expressed as relation of the indentation moduli measured in the $\langle 111 \rangle$ and $\langle 100 \rangle$ directions:

$$A_{indentation} \approx \frac{M_{\langle 111 \rangle}}{M_{\langle 100 \rangle}} \quad (3.5)$$

Vlassak and Nix [95] provided the contact mechanics equations to determine M for metals with a cubic structure indented with a flat circular punch and a paraboloid. The contact problem was further extended to a flat triangular indenter. Since the analytical solution to the proposed equations is not feasible, a numerical solution was applied. The so derived moduli for some cubic materials including aluminum are given in [94]. The results indicate a decrease in the measured anisotropy and confirm the indentation averaging effect. Yet, the contact mechanics approach of Vlassak and Nix can be simplified in order to achieve an analytic solution. This is accomplished by assuming a conical indenter geometry (rotational symmetry) and an orthotropic material. The solution is an explicit approximation as proposed by Delafargue and Ulm [15]. It is demonstrated by Delobelle et al. [16] to be in good agreement with the numeric calculations proposed by Vlassak and Nix [94]. In this work we utilize the formulation used by Delobelle et al. that provides very similar results to the three-dimensional finite element simulation of a Berkovich indentation [16]. The indentation modulus $M_{\langle uvw \rangle}$ in the crystallographic $\langle uvw \rangle$ direction can be calculated as follows:

$$M_{\langle uvw \rangle} = M_{\text{VRH}} \sqrt{\frac{\langle C_{11}^* \rangle}{\langle C_{33}^* \rangle}} \quad (3.6)$$

with M_{VRH} being the isotropic indentation modulus approximated with the Voigt-Reuss-Hill method and $\langle C_{ij}^* \rangle$ the elastic constants of the orthotropic material in with $\langle 11 \rangle$ being the indentation direction. These can be deduced using the elastic constants used by Vlassak and Nix [94, 84] and the following relations for $\langle C_{ij}^* \rangle$ according to Delobelle et al. [16]:

$$\begin{aligned} \langle 100 \rangle \quad \langle C_{11}^* \rangle &= C_{11} & \langle C_{33}^* \rangle &= (3C_{11} + C_{12} + 2C_{44})/4 \\ \langle 110 \rangle \quad \langle C_{11}^* \rangle &= (C_{11} + C_{12} + 2C_{44})/2 & \langle C_{33}^* \rangle &= (9C_{11} + 7C_{12} + 14C_{44})/16 \\ \langle 111 \rangle \quad \langle C_{11}^* \rangle &= (C_{11} + 2C_{12} + 4C_{44})/3 & \langle C_{33}^* \rangle &= (C_{11} + C_{12} + 2C_{44})/2 \end{aligned} \quad (3.7)$$

M_{VRH} can be calculated from the isotropic shear moduli G_V , G_R and G_{VRH} (Voigt, Reuss and Hill approximations as given by Chung and Buessem [14]):

$$G_V = \frac{C_{11} - C_{12} + 3C_{44}}{5} \quad (3.8a)$$

$$G_R = \frac{5}{\frac{4}{C_{11}-C_{12}} + \frac{3}{C_{44}}} \quad (3.8b)$$

$$G_{\text{VRH}} = \frac{G_V + G_R}{2} \quad (3.8c)$$

The isotropic Young's modulus E_{VRH} can be calculated from G_{VRH} as follows:

$$E_{\text{VHR}} = G_{\text{VRH}}(2 + 2\nu) \quad (3.9)$$

Finally, M_{VRH} can be evaluated according to the relation used by Göken [36]:

$$M_{\text{uvw}} = E_{\text{uvw}}/(1 - \nu^2) \quad (3.10)$$

For aluminum a Poisson's ratio $\nu = 0.35$ was used for calculations [44]. Equation (3.10) is used to compare Young's modulus from Equation (3.4) to the indentation modulus. The anisotropy of indentation hardness depends on a more complex plastic material behavior that is difficult to derive explicitly just from the materials structure.

3.3 Plastic deformation

3.3.1 Dislocation slip

The deformation is permanent, when the material is loaded beyond the yield strength. For metals, the yield strength approximated from the model of simple shearing of atomic planes (Figure 3.3), exceeds experimental values by multiple orders of magnitude [77]. Thus, another mechanism for plastic deformation must operate at lower stress levels. Dislocation slip is the main mechanism to account for plastic deformation of metals and especially aluminum. It is based on the movement and multiplication of dislocations.

Dislocations are one-dimensional or linear lattice defects which are described as an additional half-plane between two atomic planes (Figure 3.4 (a)). In contrast to the plane slip mechanism only one atomic bond is flipped at a time to move the dislocation by one lattice constant (Figure 3.4 (a)-(c)). The dislocation moves step-wise along the crystal lattice by folding atomic bonds one-by-one. The stress required to activate plastic deformation due to dislocation slip (i.e. Peierls stress) along a certain crystallographic plane is naturally significantly lower than for slipping a full atomic plane.

This mechanism can only set in, when mobile dislocations are present in the material. For pure, quasi defect-free monocrystalline metals, dislocations must be generated first to allow plastic deformation. The same applies to mechanical measurement of very small defect free material volume (local small scale measurement, i.e. nanoindentation at shallow indentation depth). The relevant mechanism for initial generation dislocations is sliding of full atomic planes (shown in Figure 3.3), resulting in significantly higher stress.

Dislocation slip is an anisotropic process. It depends on the materials structure (fcc in case of aluminum) and the direction of the applied stress in respect to the lattice orientation. The configuration of preferred crystallographic planes and directions for dislocation slip is the so-called "slip system". For fcc metals the slip system is designated as $\{111\} \langle 1\bar{1}0 \rangle$. The slip planes are shown in Figure 3.5. Consideration of all crystallographically equivalent lattice planes and directions of each slip system, results in 12 possible slip directions (indicated with white arrows for one slip plane (purple) in Figure 3.5).

Taking the active slip systems into account is of particular importance for nanoindentation. Kucharski and Jarzabek demonstrated that pile-up formation around the indenter

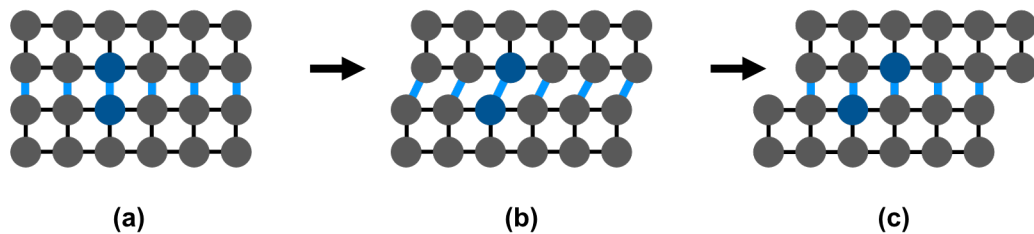


Figure 3.3: Sliding of complete atomic planes in a single crystal. **(a)** Undisturbed atomic order without applied load. **(b)** The load is applied and the atomic bonds are stretched reversibly (two blue atoms are connected via a blue atomic bond). **(c)** All atomic bonds along the plane (blue) simultaneously flip to the next atom on the left side to accommodate the stress. Figure adapted from [77].

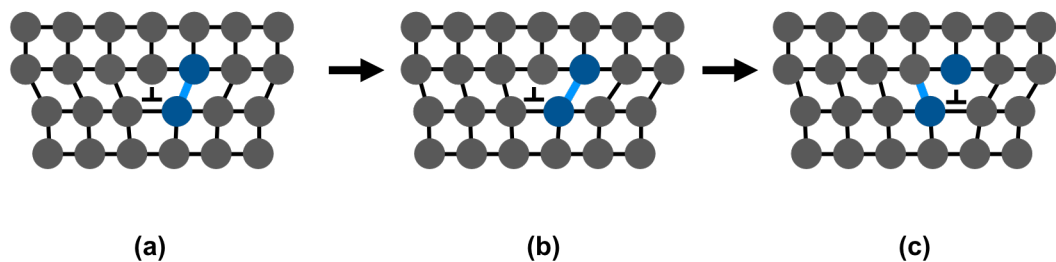


Figure 3.4: Movement of a step-dislocation due to external stress. **(a)** Undisturbed atomic order without load. The dislocation is marked with an upside-down “T”. **(b)** Applying shear stress below the critically resolved shear stress (CRSS) leads to an elastically distorted structure. **(c)** Once the shear stress exceeds the CRSS, a single atomic bond (blue) flips to the next atom, moving the dislocation by one lattice constant.

for loads > 2 mN on monocrystalline copper depends on the crystal symmetry and the respective slip-systems [54]. In this work, the implication of indentation direction on hardness of aluminum single crystals (chapter 7) and polycrystalline aluminum (chapter 8) were explored.

3.3.2 Incipient plasticity and the pop-in effect

A typical indentation usually leads to purely elastic deformation at low indentation depth and elastic-plastic deformation at higher indentation depth and an elastic recovery during unloading. The transition from elastic to elastic-plastic deformation is a discontinuous process which is evident on the produced load-depth curve. Shallow indentation (small indentation size) on smooth surfaces of low-defect metals is very probable to be located at a dislocation free site. To mediate sufficient deformation, new dislocations must be generated or present dislocations must be unpinned. The indentation is purely elastic until the CRSS required for dislocation generation is reached. Once the CRSS is exceeded, the deformation can proceed via dislocation slip at significantly lower stresses. Mechanical properties derived with small indentation depth, i.e. smaller than the characteristic distance between statistically stored dislocations, are expected to be comparable to the theoretical yield strength as derived from the atomic plane slip model described above. This is confirmed by Gane and Bowden for Au, Cu and Al crystals at the nanoscale. The measured strength approaches the theoretical limit for the indenter size of 100 nm [30].

Typical load-depth curves on annealed metals demonstrate a discontinuity in the low-load region above the elastic limit. This discontinuity, referred to as the pop-in, is a displacement burst (load controlled indentation) or a load-drop (displacement controlled indentation). For instance this was demonstrated by Göken on NiAl crystals for indentation depths as low as 20 nm (Figure 3.6). The pop-in divides the load-depth curve into two parts. The region from zero load to pop-in shows purely elastic behavior which can be modeled with the Hertzian model for elastic contact. After the pop-in, irreversible deformation sets in. Occurrence of a pop-in indicates that the indentation took place on a dislocation free location.

It is well known that in contrast to electropolished unstrained metals, mechanically prepared metal surfaces do not show pop-ins. The load-depth curve is continuous at all stages [82, 36]. Since dislocations are introduced into the surface layer already through mechanical polishing, dislocation slip can set in at much lower stress by the activation of pre-existing dislocations [97]. Upon removing the deformation layer, the undamaged bulk material (low defect density) is exposed to nanoindentation, and the pop-in effect is regained. There is an alternative explanation for the absence of pop-ins on mechanically polished surfaces proposed by Göken and Kempf [37]. Accordingly, this effect is attributed to the morphology of mechanically polished surfaces, even polished to the so-called mirror-finish, which exhibit surface-steps (nano-scratches). These steps act as locations of focused stress and significantly reduce the load required for the nucleation of a dislocation. Also in this case, the CRSS is reduced significantly resulting in continuous indentation curves without pop-in.

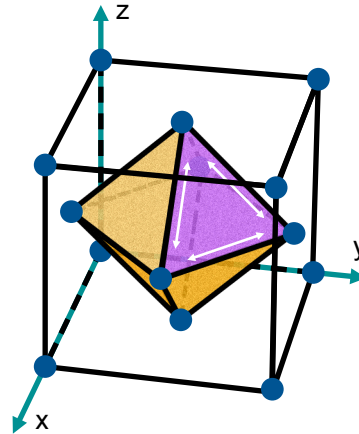


Figure 3.5: Four slip planes of a fcc structure with the $\{111\} \langle 1\bar{1}0 \rangle$ slip system are illustrated in a unit cell. Four of the eight crystallographically equivalent planes have a different orientation. Three different directions per plane (white arrows) results in 12 possible slip-directions for a fcc structure. Image adapted from [77].

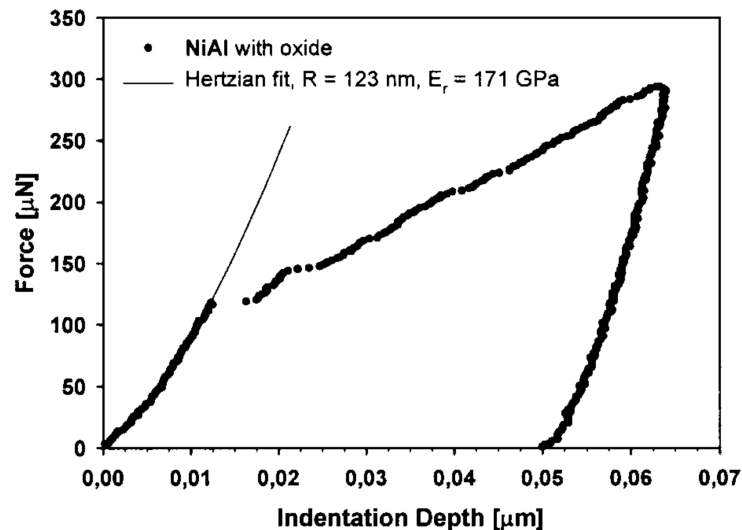


Figure 3.6: Exemplary load-depth curve showing a discontinuity at low indentation depth directly after there Hertzian contact. The curve was acquired on oxidized NiAl surface. Figure from [38], reproduced with permission from John Wiley and Sons.

Pop-in behavior represents a valuable criterion for sample preparation quality as has been demonstrated by Wang et al. [97]. They performed a statistical pop-in analysis of electropolished Ni (100) surfaces to judge the surface preparation quality. The method can also be used to qualitatively evaluate dislocation density by comparison to a reference.

3.4 Strengthening mechanisms and their impact on the microstructure

3.4.1 Strengthening mechanisms

To attain higher strength, the ability of the material to deform plastically has to be reduced. The main mechanism for plastic deformation of aluminum is dislocation slip. Therefore, all strengthening techniques introduce barriers for dislocation movement. Numerous strategies are implemented to increase the strength of aluminum. The strengthening techniques applied on aluminum which relevant for this research are the following (in the order of technological importance) [77]:

- Precipitation hardening
- Grain boundary strengthening
- Strain-hardening*
- Solid solution hardening

The main focus of this thesis is to evaluate the effect of surface preparation and machining on mechanical properties. These mainly involve strain-hardening, therefore only the effect of strain-hardening* on material plasticity and hardness was analyzed. Other strengthening mechanisms described here also influence material plasticity significantly. However, they are not affected by surface preparation of machining and are described here solely to understand their effect on microstructure and basic mechanical properties of the material. Each hardening technique is related to a certain group of lattice defects or inclusions as schematically shown in Figure 3.8.

Solid solution strengthening

Most technical alloys possess a polycrystalline structure, resulting from crystallization during material production.³ Upon solid solution strengthening the periodic atomic arrangement of each grain is disturbed by introducing substitutional or interstitial atoms (Figure 3.8 (1)). Different atomic radii of the alloying element and the host result in lattice distortions and local stress fields (tensile or compressive stress, depending on the difference in atomic radii of the host lattice and the alloying element). To move through the compressive stress field with the compressive-stress end of the dislocation, additional energy is required. If a dislocation approaches the compressive stress field with its tensile-stress

end, it is pinned. Additional energy is needed to unpin the dislocation. For aluminum, solid solution strengthening is mainly achieved by addition of magnesium.

Grain boundary strengthening

Grain boundaries separating differently oriented grains (Figure 3.8 (2),(3)) pose natural barriers to dislocation movement as was described above. However, since the indentation size is usually significantly smaller than the typical grain size of engineering materials, the effect is not observed by nanoindentation.

Strain-hardening

Strain-hardening is a result of cold work normally introduced on purpose during the manufacturing process. Yet, it also can be an undesired material defect originating e.g. in mechanical sample preparation, mechanical cutting or other mechanically induced strain. Although necessary for plastic deformation, dislocations are also obstacles to other dislocations (Figure 3.8 (4)). This effect intensifies with increasing dislocation density ρ , which can be influenced by plastic strain (e.g. via cold rolling, multiplication of dislocations). An increasing degree of deformation results in an increased ρ and thus in increased material strength. At the same time, the ductility is reduced and the material becomes brittle. Thus, strain hardening is a straightforward possibility to increase strength. However, its efficiency is limited by material embrittlement (unavoidable for increasing plastic deformation). Strain hardening can be reversed by thermal annealing of the material above the recrystallization temperature. To estimate the degree of deformation and embrittlement the cold forming degree η can be used. It is defined as the ratio of the final sheet thickness ΔS measured after deformation (i.e. through rolling) to the initial sheet thickness S_0 :

$$\eta = \frac{\Delta S}{S_0} \quad (3.11)$$

Grain boundary strengthening

Single grains (Figure 3.8 (2)) are separated by grain boundaries (Figure 3.8 (3)) that are inherent in a polycrystal and represent significant barriers to dislocation movement. The dislocations are anchored at the grain boundaries and become ineffective for plastic deformation. Significantly higher stress is necessary for intergranular strain transmission. The free path length of the dislocation is inversely proportional to the material strength. The measure of the free path length for engineering purposes is the average grain size d_m . The relationship of strength and d_m is described by the Hall-Petch law [2]:

$$\sigma_S = \sigma_0 + k \cdot \frac{1}{d_m} \quad (3.12)$$

³Unless the columnar or mono-crystalline structure is produced on purpose such as in the case of nickel-base super-alloy single crystals for turbine blades [74].

In this equation σ_s is the resulting yield stress, σ_0 is the initial or intrinsic strength and k is a constant. This relationship can be used to characterize aluminum and aluminum alloys. Analogous to strain-hardening, grain boundary strengthening can also be reversed by recrystallization.

Precipitation hardening

Precipitation hardening is a very effective strengthening technique for aluminum alloys. It is well known from the original “Duralumin” material (Al-Cu alloy). Different precipitates are formed through specialized heat treatment which proved very efficient as dislocation barriers. The prerequisites for precipitation hardening are illustrated by the binary phase diagram of the respective material:

- The compound must be an alloy
- One-sided, temperature dependent solubility of the alloying elements which increases with temperature
- Segregation of the solid solution over meta-stable intermediate states

A multi-staged heat treatment is applied to achieve precipitation hardening and the desirable material properties. It consists of three critical steps which are described on the example of a Al-Cu alloy:

1. Annealing: Heating up to a temperature above the Cu solution limit. Here the alloying element Cu is dissolved in the host α -crystal.
2. Quenching: Rapidly cooling the material to room temperature. Cu atoms are frozen on their lattice sites, resulting in the oversaturated *alpha* solid solution (thermodynamically unstable).
3. Natural (at room temperature) or artificial aging (at elevated temperatures):
 - Natural aging: Through natural aging for over 24h at max. 40 °C the Cu-rich coherent phases (Guinier Preston zones or GP1-zones) with an approximate diameter of 10 nm (few atomic layers) are formed, resulting in a moderate hardness increase.
 - Artificial aging: At elevated temperatures (below recrystallization temperature or solubility limit, typically 180°C) the GP1- zones grow in size to form larger coherent GP2-zones (stacks of several atomic layers and approx. diameter of 100 nm), the semicoherent θ' -phase.
4. Overaging: After aging for prolonged time periods the incoherent equilibrium θ -phase (Al_2Cu) is formed.

The heat treatment can be optimized according to the desired material properties from ductile naturally aged to the highest hardness possible (peak-aging). The various precipitates (GP1, GP2, θ' and θ , shown in Figure 3.8 as (5)) increase the strength to a different degree, but the semi-coherent θ' phase is most effective. The thermodynamics of

the process as well as the exact chemical description of the phases can be found in the literature [106, 63].

Other prominent microstructural features are dispersions (covalently bound particles which are added to increase strength, Figure 3.8 (6)), intermetallic phases (covalently bound phases normally present in the microstructure due to chemical reactions between the alloying elements and impurities, Figure 3.8 (7)) and coarse second phase particles analogous to intermetallic phases, (Figure 3.8 (8)).

3.4.2 Strengthening-related microstructure

Technically relevant aluminum alloys usually show complex microstructures. An example of such a microstructure is shown in the form of two scanning electron microscopy (SEM) images of the aluminum alloy AA5083 in Figure 3.7. Three grains (triple point) and a larger intermetallic phase (typical length $> 5 \mu\text{m}$) are recognizable already in the image with lower magnification (left). Higher magnification reveals additional details including smaller intermetallic phases (typical length $< 1 \mu\text{m}$). The reason for this complex microstructure is that multiple strategies were applied simultaneously to improve material strength and other properties. Normally, microstructural features are present on all length scales in the material from substitutional atoms, dislocations, grain boundaries, GP-zones, dispersoids or large second phases (Figure 3.8). When mechanical properties are measured on the macro-scale, all these features contribute to the average measured value. However, in case of small-scale mechanical testing, and especially nanoindentation, the measured volume often lies in the characteristic length scale of one of the microstructural features. Depending on the indentation depth, the size of microstructural features and the current measurement location it is even possible to measure individual properties of single features. This has to be considered in the experiment design and also in the interpretation of the results. This size relations between indenter and microstructure are shown schematically in Figure 3.8.

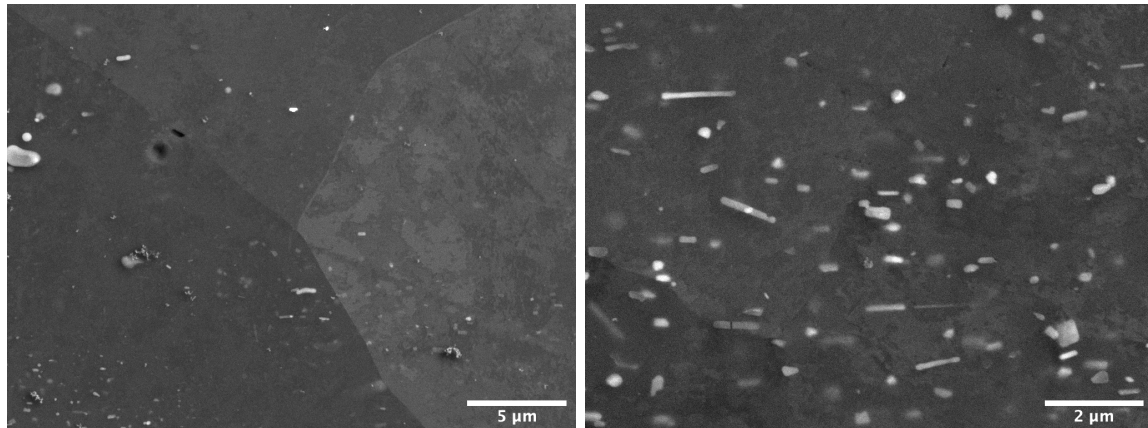


Figure 3.7: SEM image of an exemplary AA5083 microstructure at two different magnifications. (a) Triple point between three grains separated by grain boundaries and several micrometer-sized intermetallic phases (light gray especially on the top left) (b) Close-up on small sub-micrometer intermetallic phases (rounded and elongate, light gray) (SEM imaging parameters: 10kV, back scattered electrons (BSE) detector, 8 mm working distance)

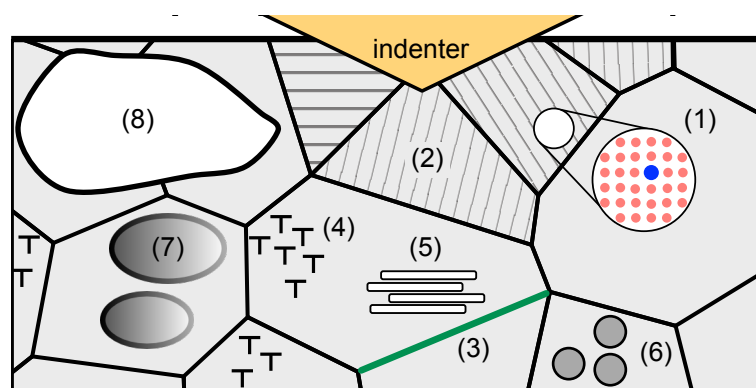


Figure 3.8: Scheme of a complex microstructure resulting from different strengthening measures. Different microstructural features on varying length scales are depicted: (1) Substitutional atoms (solid solution strengthening) (2) Grains with different orientations (3) grain boundaries, (4) dislocations, (5) GP zones (precipitations < 100 nm), (6) dispersoids (< 1000 nm), (7) intermetallic particles (< 20 μm) and (8) coarse second phase.

3.5 Recovery and recrystallization

Plastic deformation through mechanical processing (e.g. rolling, compression, milling, etc.) has a profound influence on the microstructure. This includes the development of textures (pancake grain structure), grain orientation and increased dislocation density due to cold work. However, it is possible to restore the initial grain structure through heat treatment. The two most important processes in this context are recovery and recrystallization. For materials being heat-treated at recrystallization temperature T_R (see below) at first the process of recovery sets in. The electrical conductivity improves by healing of Frenkel-defects (a combination of vacancy and an interstitial atom) and rearranging of dislocations. By contrast, recrystallization involves formation and movement of large-angle grain boundaries and thus the complete replacement of the strained grain structure with a new undeformed set of grains. A distinction is made between static recovery/recrystallization via thermal treatment after deformation and dynamic recovery/recrystallization during the deformation process.

The main driving force for recrystallization is the strain-energy which is stored in form of dislocations. The process is also influenced by other factors such as the number of defects/impurities in the material, annealing temperature T_R and the annealing time. With regard to all factors, a threshold must be reached in order to initiate recrystallization. Once this level is reached, the recrystallization begins with nucleation and growth of new grains until these eventually merge at the expense of the existing grains (primary recrystallization). The dislocations related to strain-hardening before recrystallization are eliminated along with the strained grain structure. Thus, dislocation density is eliminated discontinuously by the growth of dislocation-free grains. For this reason it is often referred to as the discontinuous recrystallization [39]. The temperature T_R required to initiate recrystallization for technically pure metals can be estimated from the respective melting temperature T_M by the following equation (temperatures in K):

$$T_R \approx 0.4 \cdot T_M \quad (3.13)$$

Pure iron with $T_M(Fe) = 1809K = 1536\text{ }^\circ\text{C}$ has a minimum $T_R(Fe) = 720K = 450\text{ }^\circ\text{C}$ according to [5]. For aluminum with $T_M(Al) = 933K = 660\text{ }^\circ\text{C}$ the same consideration results in $T_R(Al) \approx 373K$. Yet, it must be noted that this represents only an approximation since other factors such as purity grade, implanted strain energy etc. were not considered. Actually, the recrystallization temperature of Al5N is close to room temperature. Yang-Yang Lv et al. demonstrated in their work, that it is possible to control microstructure of pure aluminum by considering the recrystallization parameters (degree of deformation, temperature, recrystallization time) [62]. High purity aluminum that was recrystallized at $330\text{ }^\circ\text{C}$ for 20 minutes showed a very homogeneous grain structure. The same recrystallization procedure described in 5.2.1 was applied to obtain low defect Al5N-Poly samples with a homogeneous grain structure (chapters 6, 8 and 9).

Chapter 4

Mechanical Modification of Aluminum Surfaces

Nanoindentation enables measurement of local material properties both in the lateral direction as well as normal to the sample surface. However, mechanical properties are extracted by nanoindentation from the surface layer only. To attain trustworthy data about the surface layer, care must be taken to remove any undesired influence on the material surface. Such influence can, for example, originate from the sample preparation (deformation layer). In this chapter, the structures of mechanically influenced metallic surface is discussed in general. Mechanical polishing and electropolishing are two methods commonly used for the preparation of metallic sample surfaces for nanoindentation. Both methods are briefly described and their ability to yield appropriate surface quality is compared. Finally, micromilling is presented as a processing technique that can introduce severe plastic deformation into the near-surface region.

4.1 Mechanically affected metallic surfaces

Mechanical properties of a metallic surface can be considerably affected by surface treatment through cutting, grinding, polishing, milling and others. To avoid undesired influences on the nanoindentation results, the proper choice of sample preparation technique is crucial as already pointed out by Pathak et al. [73]. A fundamental understanding of changes in mechanical properties of the surface due to mechanical influences is important for correct interpretation of nanoindentation results. A general overview of an influenced metal surface due to superficial mechanical treatment is shown in Figure 4.1. Each aluminum surface is covered with a native surface oxide layer (1) (Al_2O_3) that is less than 10 nm thick according to Evertsson et al. [22]. Beneath the surface oxide layer lies a thicker Beilby layer (maximum 800 nm for hot and cold rolled aluminum alloys, respectively [80]). Initially it was thought to be amorphous, but recent investigations revealed its ultra fine grained structure. Then follows the strain-hardened layer. Its thickness varies widely de-

pendent on the type and severeness of the mechanical impact. These three layers are called the deformation zone with the bulk material beneath it.

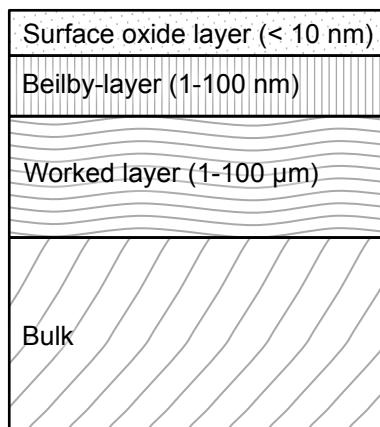


Figure 4.1: Typical structure of a mechanically influenced aluminum surface. Figure adapted from [42].

4.2 Mechanical and electrochemical polishing

As has been discussed in section 2.4, nanoindentation requires flat smooth surfaces for correct data evaluation. The appropriate methods to generate such surfaces can be adapted from metallography, because the requirements on the surface quality are very similar. In metallography, a thick deformation zone (1-3 in Figure 4.1) is undesired, since it does not represent the material microstructure, that is the subject of investigation (except for examination of the preparation method itself). The same is true for nanoindentation analysis, except for the mechanical properties being the subject of investigation.

The most common metallographic surface preparation method is mechanical polishing. However, strain-hardening of the surface is unavoidable in this case. Multiple increasingly finer surface preparation steps are applied to reduce the deformation zone with every step and to remove the scratches from the previous step. The procedure usually starts with coarse plane grinding and proceeds to fine polishing with particle size below 1 μm. As final step, the mechano-chemical polishing is often applied (i.e. acid dispersed nanoparticles or other methods like vibropolishing). However, the size of the deformation zone can only be reduced to an acceptable thickness, but not eliminated. This is especially true for very ductile high-purity polycrystalline or monocrystalline aluminum.

One method to achieve smooth almost scratch-free surfaces without introducing mechanical deformation is electropolishing. By applying a voltage to the sample, roughness peaks are dissolved electrochemically. The surface is evened according to the distribution of the electric field at the surface (increased electric field at sharp peaks). The underlying operational principle is sufficiently described in the literature e.g. in [43]. One drawback

of the method is that the material removal rate depends on the electrochemical potential. For this reason, the method is unsuitable for composite materials because of different etch rates for different constituents. Furthermore, the removed material thickness must be sufficient to remove unavoidable influences from preceding mechanical preparation steps (cutting, plain grinding, mechanical polishing). In this thesis analysis of the pop-in effect (section 3.3.2) was used to verify that the applied electropolishing parameters were sufficient to remove the deformation layer as shown in section 6.2.1.

4.3 Surface machining by micromilling¹

Miniaturization of metallic components bears advantages such as space savings, lower energy consumption or improved behavior of high-frequency components (transmission, reflection, etc.). Micromilling is a widely used technology for machining of miniaturized parts with high growth potential. It represents a technological down-scaling of the traditional milling method and as such also shares its advantages: high material removal rates and process flexibility. Hence, it is possible to produce complex three-dimensional geometries with acceptable manufacturing times. Producing miniature parts at industrial scale requires manufacturing tolerances (dimensions and surface quality) on the sub-micron level. For this means a precise understanding of the manufacturing process is necessary. Two aspects of how micromilling affects the material surface are especially relevant: surface roughness and strain hardening thorough the ploughing effect.

New challenges arise on the technological and on the material side when a critical degree of miniaturization is reached. This usually happens when a critical tool dimension approaches the removed material thickness or characteristic length scale of single microstructural features. Numerous factors influence surface integrity, such as real tool geometry, cutting parameters, workpiece properties and cutting phenomena which are summarized by Wang et al. [96]. Surface roughness is especially important for the quality of high-frequency components. Strain-hardening, on the other hand, can help to improve control over the manufacturing process. Both parameters account for the quality of the milled surfaces.

4.3.1 Effect of micromilling parameters on surface roughness

One important application of micromilling are waveguides for giga- and terahertz frequency range. With increasing frequency, wavelengths are approaching lower μm -range, surface quality becomes increasingly important, because the waveguide efficiency is influenced significantly by surface roughness. As shown by Dikemlik et al. surface roughness significantly influences the reflection and affects the signal-noise ratio [17]. This could be

¹Parts of the following section are adapted from Filippov, P.; Kaufeld, M.; Ebner, M.; Koch, U. *Investigation of the effect of end mill-geometry on roughness and surface strain-hardening of aluminum alloy AA6082. Materials (Basel). 2020, 1–16. [23]*

confirmed by Iwai et al. for high-frequency transmission lines by new measurement approach [48]. Tian et al. demonstrated successful fabrication of a terahertz waveguides with extremely low transmission loss owing to low surface roughness among other aspects [91].

Various parameters have been shown to influence surface roughness. Yuan et al. reported that cutting edge radius between $0.3\ \mu\text{m}$ and $0.6\ \mu\text{m}$ has a considerable effect on surface roughness [102]. An experimental study of pure copper using tungsten carbide micro-endmills by Filiz et al. indicated that surface roughness also increases with feed rate [26]. Additionally, Aurich et al. showed, that the tilt angle of the main spindle significantly changes material removal on the microscale and influences burr formation as well as surface topography [4]. Gao et al. surveyed different micromilling parameters of nickel-based single crystal superalloy [33]. He found that feed rate, spindle speed, and milling depth have a profound influence on surface roughness. From this short review it can be concluded, that cutting edge radius and feed rate (i.e., single tooth feed) have the most severe influence on micro-milled surface roughness.

4.3.2 Strain hardening by micromilling

The mechanical properties of a metal surface are significantly influenced by the micromilling process. Surface strain-hardening is in general caused by the plastic deformation introduced into the material through milling. In the case of conventional micro-cutting the uncut chip thickness h is usually much larger than the cutting edge radius r_e (Figure 4.2 (a)). The tool can be assumed as infinitely sharp while the deformation layer remains infinitely small (the tool just slices a piece from the material without mechanically affecting the now created surface). This is different for micromilling, where h and r are on the same length-scale (Figure 4.2 (b)). The exact cutting regime is defined by the minimum chip thickness of h_{min} which is the smallest h where a minimal amount of material is still removed. The relationship of h_{min} to tool geometry is $h_{min} \approx 1/3r$ according to the literature [55, 51].

There are three significantly different cutting modes which can be distinguished in regard to h_{min} as illustrated in Figure 4.3 [1]. If h is in the same range as r_e , significant plastic deformation of the surface occurs. For cases where $h < h_{min}$ (Figure 4.3 (a)) no

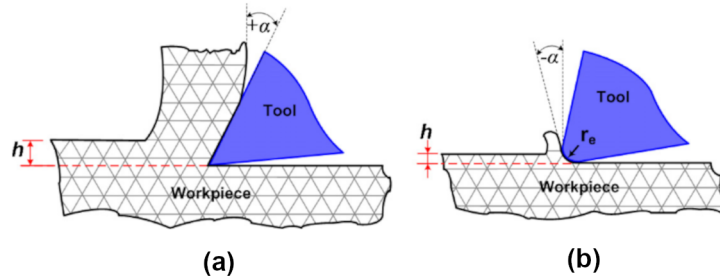


Figure 4.2: Chip formation depending on the cutting edge radius r_e and the uncut chip thickness h . (a) Traditional cutting with infinitely small r_e . (b) Micro-cutting with the r_e in the same range as h . Figure from [1], reproduced with permission from Elsevier

material is removed. However, a very thin strain-hardened layer is built up since the rounded cutting edge deforms the metal surface beyond the elasticity limit. The thickness and hardness of the strain-hardened layer depend on h and tool cutting edge radius r_e . Yet, the strain is usually so small, that the elastic springback leads to significant recovery of the surface. For $h = h_{min}$ (Figure 4.3 (b)) chip formation is initiated and material is actually removed. However, the removed material thickness is minimal, and the remaining surface layer is strain-hardened with significant elastic springback. Also, the thickness and hardness of the deformation layer depend on h and r_e . By further increasing the uncut chip thickness to $h > h_{min}$ (Figure 4.3 (c)) even more material is removed. Since $h \gg h_{min}$, a further increase of h does not affect the deformation layer. Its properties are solely dependent on the cutting edge radius. However, the impact of cutting rate is unclear and further influence on surface strain-hardening cannot be excluded.

The plastic deformation induced in the material surface by a relatively blunt tool (in relation to h) is referred to as the micromilling ploughing effect. The ploughing effect induces surface strain-hardening which leads to a significant increase in cutting forces. Klocke et al. found that the cutting regime is dominated by the ploughing effect when the uncut chip thickness h (Figure 4.2) is on the same order as the tool edge-radius [52]. Already in 1996, it was reported by Yuan et al., that the sharpness of diamond tools has a significant influence on surface strain-hardening [102]. Lai et al. showed systematically that the micro-cutter edge radius r_e (Figure 4.2) is the reason for minimum chip thickness h_{min} [55]. For oxygen free high conductivity copper using a tool with $r = 2\mu\text{m}$, h_{min} is proposed to be 0.25 times r_e . Additionally, they proposed that the micromilling size-effect is caused by material behavior at the micron level. Additionally, Biermann et al. characterized the influence of h_{min} on burr formation [8]. In conclusion, it can be stated that the interplay of the undeformed chip thickness and h_{min} , which is mainly influenced by r_e , is critical for surface strain-hardening.

Rarely the ploughing effect is measured directly from the surface hardness, but is rather evaluated from the increase of cutting forces on the micro-scale. Niu et al. reported that cutting forces increase with increasing tooth feed and cutting edge radius [69], which is in good agreement with the above theory. Also, the previously mentioned study of Lai et al. introduces a model to predict the cutting forces while taking the size-effect by the strain-

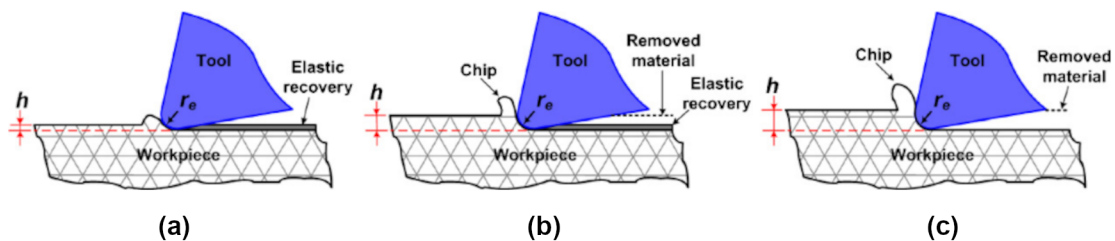


Figure 4.3: The effect of h on chip formation and surface strain-hardening due to the ploughing-effect. (a) $h < r_e$. (b) $h \approx r_e$. (c) $h > r_e$. Figure from [1]

gradient plasticity into account [55]. However, it is important to measure these effects directly from the machined surfaces to characterize the response of the material surface to micromilling.

The milling-process is highly dependent on tool's geometry at the micro- and nanoscale. Also, the nano-strain-hardened surface layer with typical dimensions on the nanometer scale is beyond reach of traditional mechanical analysis methods. Nevertheless, the mechanical properties of such surfaces can be evaluated with nanoindentation. As demonstrated by Boehme et al. on austenitic stainless steel, nanoindentation constitutes an effective method to directly investigate critical changes in mechanical properties of micro-milled surfaces [9]. This is feasible due to the ability of nanoindentation to measure material volume or thickness on the nano-scale or even to acquire depth-dependent hardness profiles.

Chapter 5

Materials and Methods

In this work, aluminum materials were prepared and studied by nanoindentation and complementary methods. In this chapter, the utilized raw materials and the respective preparation and analysis methods are documented. At first, the properties of raw materials as aluminum single crystals, polycrystalline aluminum and the engineering alloy AA6082 are provided. These materials prepared and processed by recrystallization, uniaxial compression and micromilling to yield a defined state of deformation. To avoid undesired mechanical damage to the surface, samples were electropolished for further analysis. The quality of the so prepared surfaces was initially evaluated by roughness measurements. Nanoindentation is the main tool for mechanical analysis of this work. Therefore, the employed device and the specific methodology are described in more detail. Generally, two main techniques were used for characterization, standard and multi-step indentation procedures. Finally, to analyze the collected nanoindentation data, experimental data was fitted according to models. The mathematical description of these models concludes the chapter.

5.1 Raw materials

The list of used materials, including the delivered form, nominal composition and the supplier are summarized in Table 5.1. A commercially available high purity (99.999%) aluminum single crystal grown along the $\{111\}$ direction was used. The crystallographic orientation of single crystal cylinders (diameter 10 mm, length 25 mm) was verified by X-Ray Laue diffraction (Figure A.1). Samples with (111), (110) and (100) oriented surfaces were prepared by cutting the original cylinders along the respective lattice planes with a lapping saw.¹ The Al5N-Poly (plate) material was rolled from originally 100 mm down to 5 mm thickness ($\eta = 95\%$) and subsequently recrystallized at 250 °C by the supplier resulting in hardness of approx. 17 HV20 (Vickers hardness with applied load of 196 N, according to DIN EN ISO 6507-1). Al5N-Poly rods were used for compression experiments that required

rotationally symmetric samples. 5 Original high purity aluminum rods (diameter 5 mm, length 100 mm) in the “as drawn” state were separated into smaller cylinders (diameter 7 mm, length 7 mm) and processed according to the respective experiment. AA6082 plate with hardness of 106 HV20 was used for the milling experiments. This medium strength structural alloy is widely used for machining and possesses an excellent corrosion resistance. As a base-line reference high purity recrystallized aluminum (hardness 12 HV5) was investigated.

Table 5.1: Overview of raw materials used in this study. The code given in the first column is used throughout the present study. Additional information including the chemical composition is provided in chapter A, for exact reference see right column.

Code	Material	Form	Composition	Supplier	Chem. comp.
Al5N-SX	Al, single crystal	$\langle 111 \rangle$ -rod	99.999 % Al	Alineason Materials Technology GmbH	-
Al5N-Poly	Al, polycrystalline	plate	99.999 % Al	HMW Hauner GmbH & Co. KG	Table A.1
Al5N-Poly	Al, polycrystalline	rod	99.999 % Al	Goodfellow GmbH, Hamburg, Germany	Table A.2
AA6082	EN AW6082-T651	plate	AlSi1MgMn	Vimecto Alro S.A.	Table A.3

Table 5.2 presents a complete overview of all samples studied in this thesis. The further treatments are described in the following sections. The recrystallization procedure is described in section 5.2.1. The details of the uniaxial compression test used to produce compressed specimen are provided in section 5.2.2. The electropolishing procedure is described in section 5.3. The specifications of the milling procedure are provided in section 5.2.3.

¹The help of Prof. Dr. P. Gille from Crystallography Section of the Department of Earth- and Environmental Science, Ludwig-Maximilians-Universität München in the preparation of single crystal specimen is gratefully acknowledged.

Table 5.2: Overview of samples investigated in the experimental part of this work. The base materials from Table 5.1 with the respective form, sample orientation, bulk and surface treatments are represented.

Material	Form/Orientation	Heat treatment	Mechanical treatment	Surface preparation
Al-SX	Rod / (100)	as grown	as grown	electropolished
	Rod / (110)			
	Rod / (111)			
Al-Poly	Plate	recrystallized	-	electropolished
	Rod		compressed (0-75%)	
AA6082	Plate	T651	-	electropolished
				$f_z = 3 \mu\text{m}$
				SC-mill $f_z = 8 \mu\text{m}$
				$f_z = 14 \mu\text{m}$
				MD-mill $f_z = 8 \mu\text{m}$
				$f_z = 14 \mu\text{m}$

5.2 Material treatment

5.2.1 Recrystallization

For recrystallization of pure aluminum samples two slightly different procedures were used. After the Al5N-Poly (plate) samples were cut to required dimensions, they were recrystallized at 330 °C for 20 minutes and cooled down to room temperature. Since the material was already received in a slightly recrystallized state, additional recrystallization resulted in a more homogeneous microstructure. Thereby, the measured macrohardness was reduced to approximately 12 HV. A slightly varied procedure was applied to produce recrystallized material for uni-axial compression. Cylinders (length 7.5 mm, diameter 5 mm) were separated from the Al5N-Poly rod. Yet, the annealing time of 20 min proved insufficient to acquire a homogeneous grain structure. For this reason, the annealing time was extended to 45 minutes.

5.2.2 Uniaxial compression

Bulk deformation of polycrystalline aluminum was performed to understand the influence of plastic deformation and subsequently apply this knowledge to micro-milled surfaces that were expected to show more complex behavior. In this case, the entire sample was deformed whereby the strain-hardening of the material is influenced by the degree of deformation

η (equation (3.11) in section 3.4.1) and the respective orientation of each slip system. A compression test has proven to be a very suitable tool to yield samples with a well defined degree of deformation. In comparison to rolling the strain rate and the final η are much more reproducible. Therefore, the samples were compressed to achieve a defined η .

Al5N-Poly rod was cut into cylinders (diameter 5.0 mm, length 7.5 mm) which is a proven sample geometry for miniature compression experiments, used for example by Lenz et al. [58]. To remove the cold work caused by pulling of the rod in the course of the manufacturing process, the cylinders were recrystallized (cf. section 5.2.1). Uniaxial compression was performed on the “Zwick Retro Line” universal testing machine (Table B.1). The recrystallized cylinders were placed on the compression plates, while PTFE-tape was used to reduce friction between the sample and the compression plate. The compression setup is shown in figure 5.1. The procedure was carried out with a preload of 50 N and a strain rate of 0.1 mm/s at room temperature. The parameters used for the test series are summarized in Table 5.3. Since the readings of traverse length measurement from the testing device are less accurate for small lengths, the samples were measured manually before and after the experiment with a micrometer screw gauge.

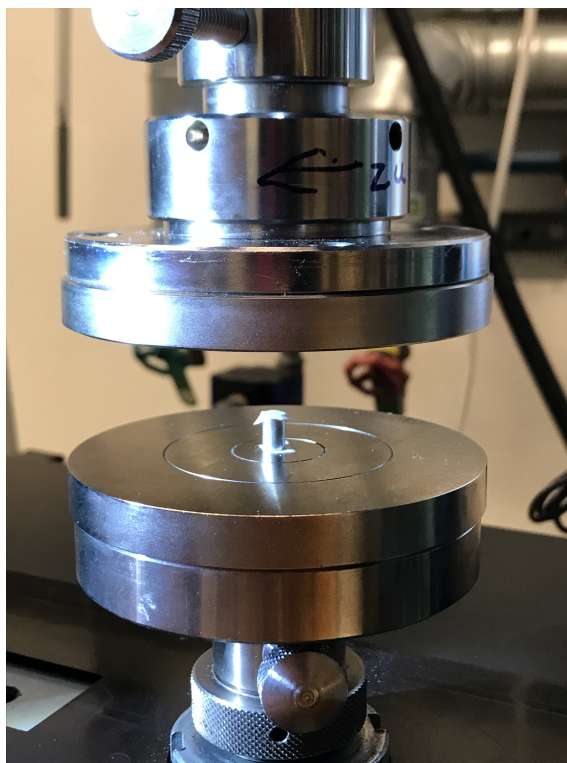


Figure 5.1: Compression setup with a cylindric Al specimen mounted between two round compression plates of the “Zwick Retro Line” (Table B.1) and covered by PTFE tape at top and bottom.

Teplyakova et al. showed evidence of strain localization in monocrystalline aluminum [89, 90]. The distribution of stress and strain is segmented, influenced by the so-called

Table 5.3: Load and strain resulting from the compression of the Al5N-Poly (rod) specimens on the “Zwick Retro Line”. Nominal strain from the devices traverse measurement. Real strain from the micrometer screw gauge measurement.

Nr.	Load (N)	Nominal strain	Real strain
1	1040	10 %	12%
2	1533	20 %	21%
3	2012	30 %	31%
4	2697	40 %	40%
5	3497	50 %	49%

volumes of eased stress (VES) according to their work. To verify the influence of VSE on the distribution of strain hardening in the sample volume preliminary investigations were performed. Yet, no hardness gradients were observed along or normal to the load direction. Hence, it could be demonstrated that for polycrystalline aluminum VES do not affect strain-hardening distribution across the sample face.

5.2.3 Micromilling²

The samples were micromilled on the “KERN Pyramid Nano” CNC machining center (Table B.1). For all experiments, cutting velocity v_c , rotational speed n , axial cutting depth a_e , radial cutting depth a_p and tool diameter D were identical, while the feed per tooth f_z was varied between 3.0 μm , 8.0 μm and 14 μm as shown in Figure 5.2. The peripherally milled surface was used for further analysis (highlighted in green in Figure 5.2). For comparison, two different commercially available single-tooth micro end-mills were used for micromilling:

- Solid carbide (SC) end-mill (Sphinx Tools AG, Derendingen, Switzerland)
- Monocrystalline diamond (MD) end-mill (Diatec Diamond Technology LLC, Pforzheim, Germany)

Both mills are nominally similar with an effective cutter diameter of 500 μm and the cutting length of 1000 μm and 500 μm respectively. However, geometrical characteristics of the tools that critically affect the produced surface (i.e. the wedge angle β , the cutting edge radius r and the cutting edge roughness, cf. Figure 5.3)) were not available from the datasheets. To obtain these parameters the tools were inspected by light microscopy and SEM, while the cutting edge roughness was determined as described in section 5.4.1. Additionally, flank and rake face morphology were qualitatively evaluated.

²Parts of the following section are adapted from Filippov, P.; Kaufeld, M.; Ebner, M.; Koch, U. *Investigation of the effect of end mill-geometry on roughness and surface strain-hardening of aluminum alloy AA6082. Materials (Basel). 2020, 1–16. [23]*

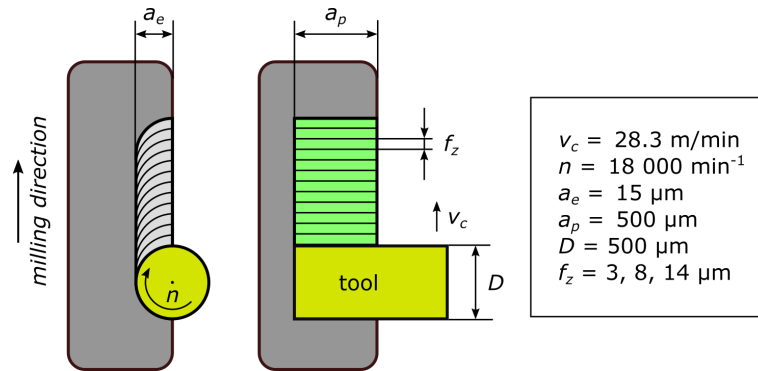


Figure 5.2: Scheme of the machined structures with corresponding process parameters.

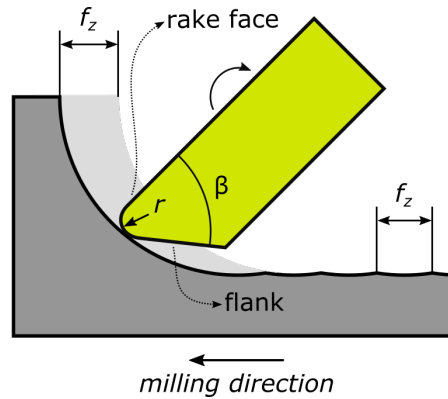


Figure 5.3: Illustration of the tool parameters wedge angle β and cutting edge radius r along with single tooth feed f_z and milling direction.

5.3 Sample preparation by polishing

In the course of this study, aluminum surfaces were prepared by electropolishing, mechanical polishing and micro-machining. All these preparation techniques have different effects on the metal surface, ranging from zero mechanical influence (electropolishing) to a severe strain hardening of the surface (micro-machining). The actual effect of the sample preparation method on the mechanical surface properties also depends on technological details and process parameters.

At first, the general sample separation and polishing procedure (mechanical and electrochemical) are described. The following principal steps are highlighted in Figure 5.4. Prior to surface preparation, the specimens must be mounted. This step is necessary for several reasons. Mounted samples can be easily either mechanically polished or electropolished. The fixation in the nanoindenter is much easier with standardized sample geometry (25 mm cylinders). Finally, pure aluminum samples are ductile, hence they need an extra support to prevent undesired cold work through handling or fixation.

The specimen were cleaned with ethanol, embedded with Specifix cold mount resin (Table B.2) and cured for over 12 hours at room temperature. To achieve a planar surface,

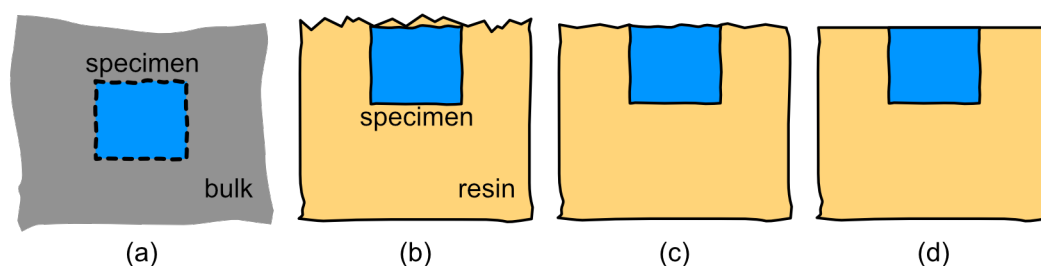


Figure 5.4: Illustration of the sample preparation. (a) Sample separation from the bulk. (b) Mounting/Embedding the sample in a resin. (c) Plane grinding the embedded sample. (d) Polishing of the specimen.

the mounted samples are mechanically plane ground on SiC abrasive paper under water flow. The grit of abrasive paper is increased successively from 600 to 2500 (grain size < 10 μm). For electropolishing the samples were contacted from the back through a drill hole just deep enough to reach the metallic surface. It was positioned at the edge of the sample to avoid potential damage to the investigated sample region.

Two different sample preparation techniques were used. While the initial sample preparation remains the same (mounting and grinding), the polishing is made either mechanically or electrolytically. For samples, where a flat surface is required and a thin deformation layer is acceptable, mechanical polishing is preferred. For samples, where the deformation layer has to be removed completely, electrolytic polishing was used. The used agents and devices are summarized in Tables B.1 and B.2.

In preliminary studies, Al5N-SX samples were mechanically polished to investigate the influence of the polishing procedure (according to the protocol documented in Table 5.4). Therefore, the Dap-7 polisher (Struers ApS, Ballerup, Denmark) was used. The samples were polished on a fibre cloth with a “CT Dia Twin Poly” polycrystalline diamond emulsion down to 1 μm grain size (rotation speed 125 rpm). Then the sample was polished on a perforated cloth using OP-S (Table 5.4). After the last step the sample was “washed” with detergent and rinsed with distilled water directly on the polisher to remove the OP-S residue. An exemplary indentation curve acquired on mechanically polished surface can be found in Figure 7.1 (section 7.2).

Table 5.4: Parameters of the mechanical polishing of aluminum samples, for used materials see Table B.2

Step	Mat	Polishing agent	Load (a.u.)	Time (min)
1	Fibre cloth	CT Dia Twin Poly 6 μm	1.5	4
2	Fibre cloth	CT Dia Twin Poly 3 μm	1.5	3
3	Fibre cloth	CT Dia Twin Poly 1 μm	1.0	3
4	Perforated cloth	OP-S	0.7	3

All Al₅N samples in this study, with one exception of the sample above (Figure 7.1 from (section 7.2)), were electropolished to provide smooth and more importantly, unstrained, ultra-pure aluminum surfaces suitable for nanoindentation. The basic principle of electropolishing consists of connecting the sample as the anode of an electrolytic cell. The sample is then submerged into the electrolyte and subjected to DC voltage with an electrochemically superior material being the cathode. In consequence, the sample is anodically dissolved. Thereby, roughness peaks and edges are dissolved which leads to a leveling of the sample surface [43]. Since no mechanical influence is exerted on the surface (the influence of initial plain-polishing step is removed by succeeding electropolishing) the mechanical surface properties are not influenced by sample preparation. For this reason, electropolishing is often used to produce smooth low defect surfaces for nanoindentation testing [95, 60, 101]. It is also used in present thesis for this very purpose.

This principle is implemented in the “Electromet III” (Figure B.1 and table B.1). The sample is positioned upside down with its surface on a round insulating mask above the electrolyte. The electric contact is made through the drill hole with soft aluminum spring. The specimens are electropolished at 20 V for 60 seconds while the electrolyte “CT A2” (Table B.2) is pumped up onto the sample surface from the bottom. This ensures fresh electrolyte on the sample surface and the removal of reaction products by hydrodynamics.

Owing to the high current during electropolishing, the sample can heat up considerably, while the heat cannot be dissipated by the mounting material (epoxy resin). Due to different thermal expansion properties of resin and metal, the embedding material can be mechanically deformed as it is shown at Figure 5.5. In addition to that, the material condition can change under exposure to heat. The electrolyte is therefore continuously cooled to < 14 °C. The electropolished samples were subsequently cleaned under running water, rinsed with ethanol and dried in hot air. After that, the surface was inspected microscopically with the “Hirox RH2000” optical microscope (Table B.1) at an objective magnification of 250x.

Aluminum single crystals in three major orientations (100), (110) and (111) were embedded and electropolished as described above (section 5.3). Additionally, the specimen back-side was ground plane-parallel to the top-side, with the maximum angle between the front- and back-side of 0.3°.

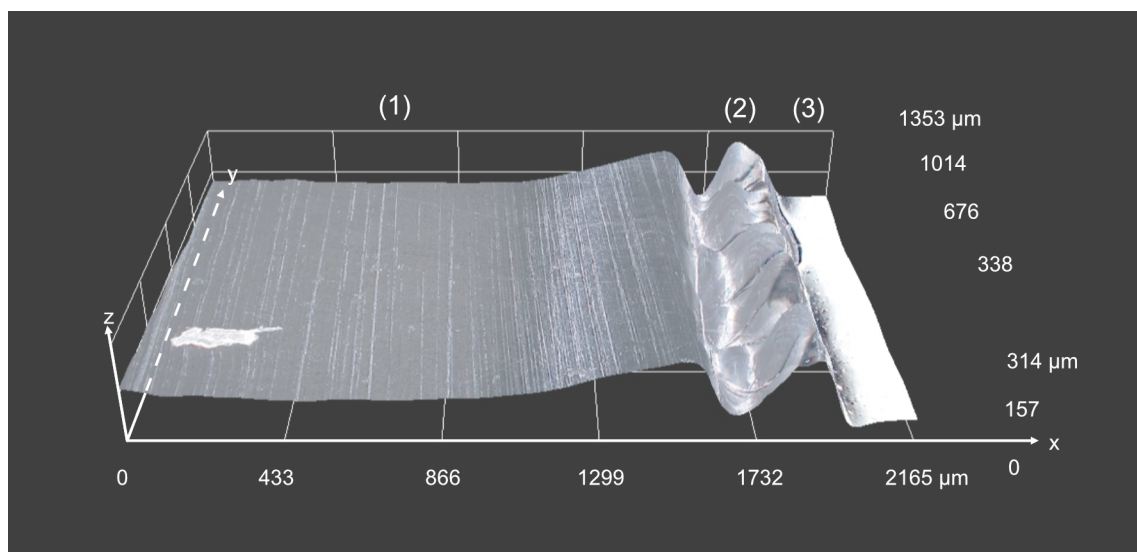


Figure 5.5: Light microscopy 3D multi focus image of an embedded sample with the resin surface damaged due to excessive heat development. The surface (plain-ground resin) is flat in the distance of the metallic sample (1). Close to the metallic sample (3) the surface has substantially bulged due to excessive heat development (2). This produces a significant step (irreproducible, on average above 100 μm) between the deformed resin (2) and the electropolished specimen surface (3) resulting in undefined fringes around the metal sample. Image adapted from [24].

5.4 Roughness analysis

5.4.1 Topography acquisition

Roughness is an important surface property and was investigated in the course of this work for different purposes and on different specimens. The chosen methods for topography acquisition and roughness determination depend on sample morphology and objective. The performed roughness investigations can be separated into three basic types:

- Height variations along cutting edge of the mill (two-dimensional profile extracted from optical image)
- Small smooth areas (sub 100 nm roughness) on electropolished Al5N-Poly (three-dimensional topography obtained by AFM) and extraction of two-dimensional profiles from these data
- Large areas of micro-machined AA6082 (three-dimensional topography acquired by confocal microscopy and extraction of two-dimensional profiles from these data)

Table 5.5 presents an overview of the samples on which roughness was measured, the extracted roughness parameters and the respective software used for analysis. The following section describes the exact procedure.

Table 5.5: Overview of the different techniques used for roughness determination

Topography acquisition method	Properties	Software
Optical microscopy	R_a	Fiji, ImageJ
AFM	R_q, R_t	Gwyddion
Confocal microscopy	R_q, R_t, S_q, S_z	Gwyddion

The roughness of smooth electropolished samples was measured with the AFM. This allows to measure surface height variations below 100 nm with sufficient accuracy. The Nanowizard AFM (Table B.1) equipped with a “Bruker MLCT” tip (20 nm tip radius) was used in contact mode to image the surface. Three 100 x 100 μm^2 square scans with a resolution of 1024 x 1024 pixels were taken. The resulting topographic images were processed with the Gwyddion software for statistical analysis. Surface profiles were extracted from which R_a was determined according to equation (5.1).

Surfaces with higher expected roughness were analyzed with optical confocal microscopy which allows to quickly and reliably acquire surface topography. This is especially important, when multiple samples must be compared. The “Leitz Ergoplan” confocal microscope with a 20 x lens was used. To determine the roughness of micro-milled surfaces three profiles perpendicular and parallel to the milling direction were extracted from three different confocal images. One-dimensional roughness parameters R_q and R_t were determined as described by equations (5.2) and (5.3). The contribution of the intermetallic compounds

was not further evaluated. Thus, the profiles were extracted by systematically avoiding large intermetallic phases. Likewise, imaging artifacts were excluded from the analysis.

For roughness analysis of the mill's cutting edge three optical images of the cutting edge were taken perpendicularly to the rake face (view field 160 μm). Reflected light microscopy was used preferentially to confocal microscopy or SEM, because of the shallow depth of field which yields better edge contrast. Only the inner 80% of the image width were used for analysis because image margins were not sufficiently sharp. Cutting edge profiles were extracted via an image recognition software ("Analyze_Stripes" plug-in of the Fiji software [81]). From the cutting edge profile one-dimensional roughness values, Root Mean Square Roughness R_q and Maximum peak-to-peak-valley height R_t , were determined according to ISO 4287-1997.

5.4.2 Determination of the roughness parameters

Roughness parameters were determined according to the available normatives which describe the exact meaning and derivation of these parameters. In the following, one-dimensional (profile) roughness parameters according to ISO4287 are presented.

Arithmetical mean deviation R_a with y_i being the vertical deviation from the mean line:

$$R_a = \frac{1}{n} \sum_{i=1}^n |y_i| \quad (5.1)$$

Root mean square roughness R_q :

$$R_q = \sqrt{\frac{1}{n} \sum_{i=1}^n y_i^2} \quad (5.2)$$

Maximum height of the profile R_t :

$$R_t = \left| \min_{1 \leq i \leq n} y_i \right| + \left| \max_{1 \leq i \leq n} y_i \right| \quad (5.3)$$

The aerial (surface) roughness parameters according to ISO52178 used in this work are defined as follows:

Average quadratic height S_q :

$$S_q = \sqrt{\frac{1}{A} \iint_A z^2(x, y) dx dy} \quad (5.4)$$

For AFM-data with discrete x-y-values the integral can be replaced with a sum:

$$S_q = \sqrt{\frac{1}{MN} \sum_{k=1}^M \sum_{i=1}^N |z(x_k, y_i)|^2} \quad (5.5)$$

Maximum height S_z (analogous to R_t , but referred to a surface):

$$S_z = \left| \min_{1 \leq i \leq n} y_i \right| + \left| \max_{1 \leq i \leq n} y_i \right| \quad (5.6)$$

5.5 Nanoindentation setup

5.5.1 Device installation and setup

The nanoindentation experiments were performed with the “Picodentor HM500” (Table B.1) shown in Figure 5.6. In the nanoindentation experiments force and displacement must be measured with sufficient accuracy to provide reliable results on the nanoscale. Every vibration source with potential influence on the measurement must be eliminated. As can be seen from Figure 5.6 (a) the device is placed in a glass housing for acoustic insulation. Additionally, the Picodentor is mounted on an actively damped piezoelectric table to minimize the influence of building vibrations. The device is equipped with sensors for measuring temperature and humidity. This is of essential importance, because temperature fluctuations have a profound influence on the measurement stability.

The Picodentor in Figure 5.6 (a) represent a typical microscope/nanoindenter arrangement which is shown in more detail in Figure 5.6 (b). The device features a computer controlled two-axis stage (x-y) which can translate the sample from the microscope to the indenter with a repeatability of below 500 nm. The test load (generated by an electromagnetic induction coil) can be varied over a wide range from 5 μN to 500 mN with a force resolution of $\Delta F \leq 100$ nN. Indentation depth is measured by an eddy-current probe with a resolution of $\Delta h \leq 40$ pm and a maximum measurable indentation depth of 150 μm .

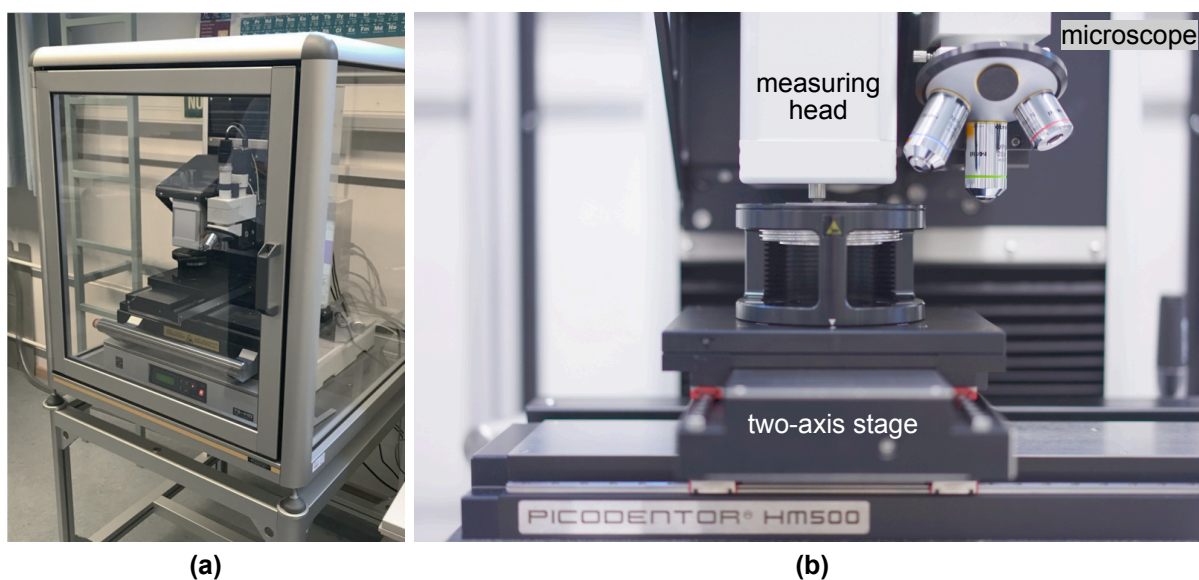


Figure 5.6: Photographs of the Picodentor HM500 at the installation site in the Laboratory of Materials Engineering, Munich University of Applied Sciences. (a) Device overview (b) Centerpiece of the instrument with measuring head, two-axis stage and microscope.

5.5.2 Sample fixation

As described in section 2.4.1, the instrument frame compliance C_f can have major influence on the nanoindentation results. Yet, this is not an issue for the Picodentor in contrast to other systems. C_f is usually measured on a reference sample and taken into account for actual measurements. This approach has one notable drawback: instrument compliance may change due to fluctuations of environment temperature, sample fixation or other factors. This problem is solved on the Picodentor by maximizing the frame stiffness to a level where the frame can be considered infinitely stiff in comparison to the indenter-sample contact. To achieve this a special sample down-holder (SDH) is used to minimize frame compliance and reduce the influence of sample fixation. Its working principle is shown in Figure 5.7. In contrast to the C-shape nanoindenter design (Figure 2.1), the complete indenter head is placed upon the sample with a SDH. This minimizes the frame size, thus the system's compliance. In addition, it presses the sample with a defined load against the measurement table which minimizes the compliance of the sample fixation.

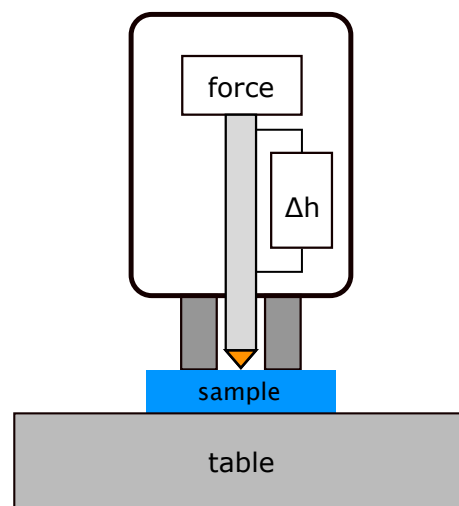


Figure 5.7: Sketch of the Helmut-Fischer frame design with a SDH. To be compared to the basic nanoindenter device layout shown in Figure 2.1. The device frame is excluded from the measurement by which the system compliance is reduced significantly.

Despite these advantages, the SDH can still have a negative influence on the measurement. Two effects concerning the nanoindentation of electropolished micro-sections are illustrated in Figure 5.8. One issue arises when the SDH is positioned on a different material than the indented specimen or on an uneven surface (Figure 5.8 (a)). The effect referred to as the edge influence, is crucial for electropolished microsections that possess a step between the metal specimen and the epoxy and can result in unstable mechanical contact and creep of the SDH compromising the indenter displacement measurement. The SDH can also cause direct surface damage when placed on ductile specimens. As the SDH

is placed on the sample surface at every measurement, it leaves a round impression i.e. a stamp (Figure 5.8 (b)). While unproblematic for a single measurement, during an array measurement this can lead to an indentation measurement on a pre-damaged region. Thus, the area available for array indentations is limited due to the stamp effect.

5.5.3 Berkovich and Vickers indenters

The Picodentor can be operated with various indenter types. In this work two sharp diamond indenters were used. The geometry of the Vickers indenter is based on a square pyramid (Figure 2.6 (left), actual tip radius 480 nm in as received condition). The Vickers indenter is also widely used for the Vickers macrohardness test. Therefore the results obtained with the Vickers indenter are valuable when a comparison of indentation hardness with macro- and microhardness is desired. The geometry of the Berkovich indenter is based on a tetrahedron (Figure 2.6, with an actual tip radius of 153 nm in unused condition).³ The Berkovich indenter is the quasi standard for nanoindentation experiments, because it can be produced with a sharper tip radius (< 100 nm is possible) than the Vickers indenter (Figure 2.6). Furthermore, the area function of the Berkovich is designed to be equivalent to the Vickers indenter, i.e. the same indentation depth results in an almost identical contact area for both indenter types.

5.5.4 Area function calibration

In the present thesis the indenter area function was calibrated on fused silica (“BK7”, optical borosilicate-crown glass by Schott AG, Mainz, Germany) with known hardness. For the indenter shape correction, at least five multi-step indentation measurements were performed on the fused silica to obtain depth-dependent hardness values. To determine the corrected indenter shape an average reference curve is calculated. The correction factor

³Tip radius data are taken from the calibration certificate (AFM-measurements)

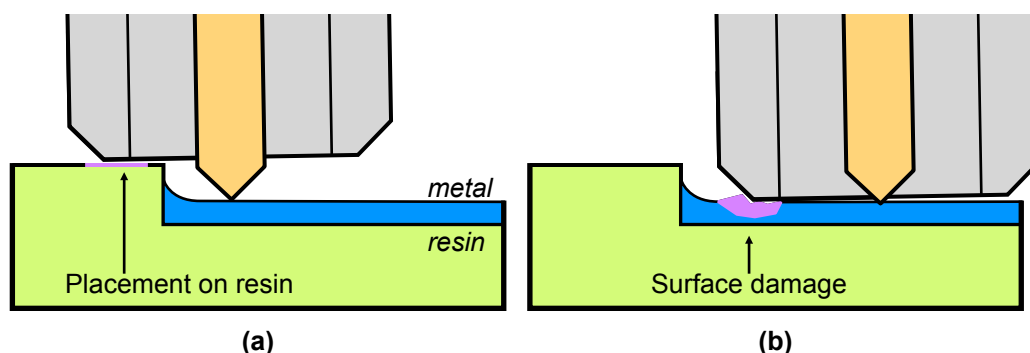


Figure 5.8: Sketch of two typical problems that occur when the SDH-unit is placed on an electropolished microsection surface (a) The SDH-unit rests on the resin, while the indenter is on the metal. (b) The SDH-unit damages the surface of ductile metal specimens.

is then automatically applied to the measurements. This procedure has to be performed for every newly installed indenter, after every indenter exchange and also on regular basis. Regular corrections are necessary compensate for indenter blunting due to tip wear. According to Fischer-Cripps [28], tip rounding becomes only critical when investigating thin films (thickness less than 500 nm) with a penetration depth of about 50 nm. Indentation depths used in this study are significantly larger than that. Therefore, the described tip calibration procedure on a fused silica reference is sufficient to take into account tip rounding of the Berkovich and Vickers indenters.

5.5.5 Basic indentation procedure

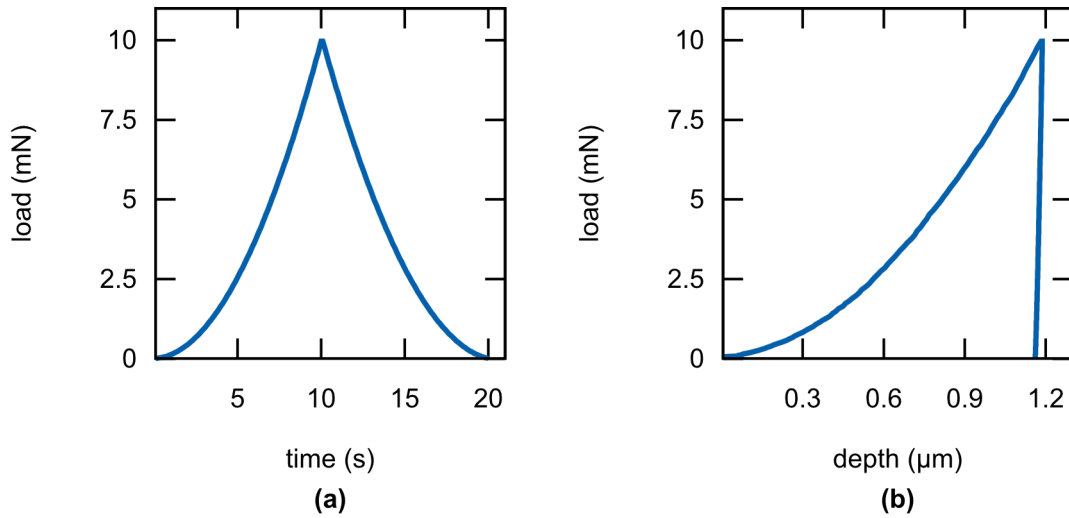
For all experiments, the distance between the indents was set according to the minimum value defined by DIN EN ISO 14577 or larger to avoid the mutual influence of indents. This corresponds to approximately ten times the indent diameter for experiments on single crystals, which is twice the value which is proposed by the ISO normative. The indentation experiments were performed in the center of the respective specimen to avoid edge effects. All experiments were carried out at room temperature. For indentation measurements, two sets of parameters were used. For basic indentation tests the procedure as described in chapter 2 was applied on the Picodentor:

1. The sample is fixated with the SDH by lowering the measurement head.
2. The indenter tip approaches the specimen surface
3. Displacement and the load zero point are determined on contact
4. The programmed indentation procedure is applied (load-depth curve is acquired)
5. The measurement is terminated by lifting the indenter and measurement head from the surface.

The exact indentation parameters used in this study for the basic indentation and for pop-in analysis are documented in Table 5.6. For the pop-in analysis, a lower F_{max} of 500 μN was used for the same t_{load} and t_{unload} . This results in a lower load rate which is advantageous for capturing pop-ins at low indentation depths. The experiments were load-controlled, while the square root of the load over time was held constant ($\sqrt{dF}/dt = const$) during the load and unload phase. This allows a very gentle load increase at low load phase of the indentation, which is especially important for indentation on ductile aluminum. This is evident from the sample indentation curve acquired from a mechanically polished aluminum single crystal (Figure 5.9 (a)). Apparently, the time-load curve appears different to the theoretic curve shown in Figure 2.2 (a) due to the mentioned $\sqrt{dF}/dt = const$ relationship for the load application. The load of 10 mN results in an indentation depth of approx. 1.2 μm on high purity aluminum with low dislocation density (Figure 5.9 (b)). In this thesis the indentation hardness H_{IT} and the indentation modulus E_{IT} were determined

Table 5.6: Indentation parameters used for the “basic” indentation and “pop-in”-analysis.

Parameter	Basic	Pop-in
t_{load}		10 s
t_{hold}		0 s
t_{unload}		10 s
F_{max}	10 mN	500 μ N

**Figure 5.9:** Exemplary indentation curve on a Al5N-SX-(110) sample obtained with the “basic”-parameters from Table 5.6. **(a)** Programmed time-load-curve. **(b)** Resulting load-depth curve.

by the Oliver-Pharr method (based on the work of Dörner and Nix) [19, 71], a method that complies with the DIN standard [18] as described in section 2.3.

To ensure complete removal of the deformation layer from Al5N by electropolishing the occurrence of the pop-in effect have been analyzed. For a quantitative analysis a recrystallized and an electropolished Al5N-SX sample were examined. The adapted F_{max} from Table 5.6 was applied, since pop-ins occur at penetration depths less than 100 nm.⁴ 100 individual measurements were performed in the course of this analysis (10 x 10 array with 10 mm). Subsequently, the load-displacement curves were manually checked for the presence of pop-ins.

⁴The chosen parameter set resulted in an indentation depth of approx. 230 nm on Al5N-SX surface (polished mechanically or electrolytically).

5.5.6 Multi-step indentation⁵

A multi-step indentation procedure is used in this work to determine depth-dependent material properties of strain hardened AA6082-surfaces (also “Enhanced Stiffness Procedure (ESP)”, as implemented in the Picodentor). F_{max} is applied in multiple partial load steps each one followed by a partial load relief of 50 %. An exemplary time-load diagram of the multi-step-procedure with $F_{max} = 500$ mN is shown in Figure 5.10 (a). Each intermediate indentation step of the resulting load-depth curve (Figure 5.10 (b)) is then evaluated with the Oliver-Pharr method to derive depth-dependent hardness or modulus. The entire measurement is performed at a single location until the maximum test load is reached. This is a clear advantage over traditional measurements, where a series of indentations are performed with different forces at different locations. Thereby not only the load, but also the local microstructure and surface roughness is varied. A Berkovich indenter is used to obtain multi-step indentation curves. The multi-step procedure is performed with the slightly varied F_{max} for all samples to achieve similar indentation depths (Table 5.7). The measurements were repeated at least five times per specimen. The curves were evaluated step-wise with the Oliver-Pharr method to determine the average hardness.

Table 5.7: Multi-step indentation parameters that were used for AA6082 and Al5N specimens to achieve similar indentation depths.

Parameter	AA6082	Al5N
Max. test load	500 mN	100 mN
Total time		420 s
True increase time		60 s
Creep		5 s
Unloading	50 % of F_{max}	
Number of unloadings		20

5.5.7 Pile-up and sink-in corrections

Correction for plastic deformation (i.e., pile-up or sink-in) of aluminum was discussed in section 2.4.3. Three methods to determine indentation hardness were compared in this work to evaluate the necessity of pile-up corrections:

- Oliver-Pharr method (benchmark) [71]
- McElhaney method based on SEM-images of indents [66]
- Tuck-method based on indentation work [93]

⁵Parts of the following section are adapted from Philippov, P.; Kaufeld, M.; Ebner, M.; Koch, U. Investigation of the effect of end mill-geometry on roughness and surface strain-hardening of aluminum alloy AA6082. *Materials (Basel)*. 2020, 1–16. [23]

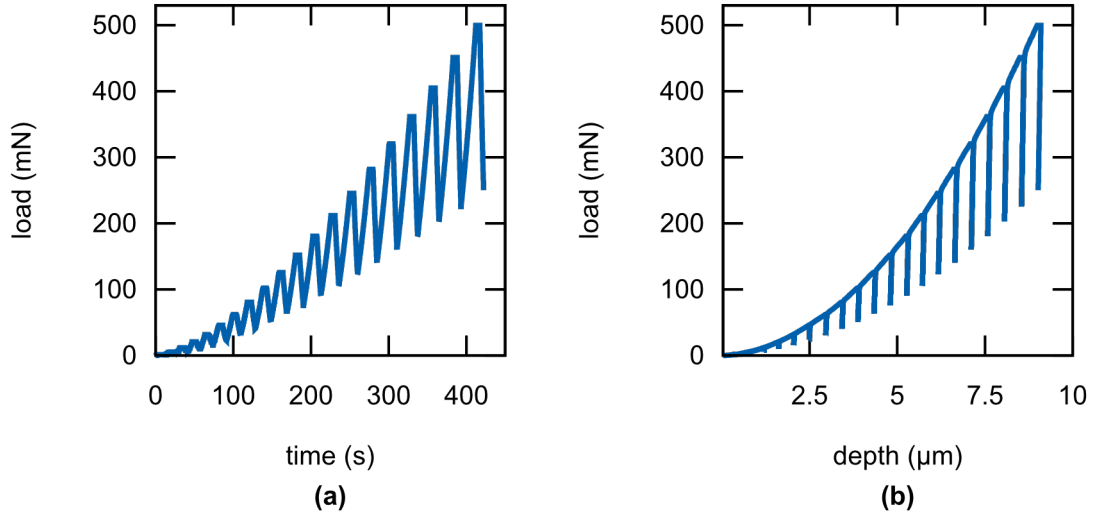


Figure 5.10: Exemplary multi-step indentation curves acquired on a Al5N-Poly (rod, as drawn) sample. (a) Programmed time-load-curve with parameters according to Table 5.7. (b) Resulting load-depth curve.

These methods are reviewed below. Indentation hardness from Vickers indentations of A5N-SX-specimens was representatively used for aluminum materials.

Oliver-Pharr method

The basic method to calculate indentation hardness H_{IT} is the Oliver-Pharr method (described in chapter 2). Hardness is determined from the cross-sectional area A_c which is derived from the indentation depth (according to the contact mechanics models incorporated in the method)[71]. Hence, hardness is solely determined from the indentation curves.

McElhaney method

McElhaney et al. observed a significant difference between the Oliver-Pharr A_c and projected area A_p determined from SEM images of the indents.[66] To account for this difference, they introduced a correction factor α :

$$\alpha = \frac{A_p}{A_c} \quad (5.7)$$

They propose to determine this factor once for a specific material. Then it can be universally applied to the Oliver-Pharr formula to correct hardness values determined from the indentation curves. To determine α , SEM images of three exemplary indents (crystallographically aligned / mis-aligned) for each crystallographic orientation and indenter-sample orientation were captured. A_p was determined manually based on the indenter

contour (real area) and A_c was calculated from the indent diagonals (ideal area). Then the hardness values were determined using the so derived correction factor.

Tuck method

An alternative method for hardness determination was proposed by Tuck et al. [93]. It is based on hardness calculation from the plastic work W_p and does not require the determination of contact area. The plastic hardness H_p is calculated on the basis of plastic and elastic indentation work.

$$H_p = \frac{kF_{\max}^3}{9W_p^2} \quad (5.8)$$

W_p is determined as the area enclosed by the load-depth curve. k is a constant depending on the indenter geometry (e. g. $k = 0.0378$ for Vicker's indenter [93]). H_p was calculated for the means of comparison for a representative indentation curve. The results of this comparison are presented and discussed in chapter 7.

5.6 Data fitting

Different functions were fitted to experimental data. For all instances, the least squares regression method was used for fitting. Since all functions used for data-fitting are non-linear, the Levenberg-Marquardt algorithm (LMA) is used to find the best fit (minimum residual sum of squares (RSS))[99]. The choice of the appropriate model and its mathematical expression is critical to achieve reasonable fits. The used equations are presented in the following.

Sine function

Preliminary experiments on aluminum single crystals demonstrated a periodic dependency of H_{IT} and M on the azimuthal orientation of the Vickers indenter. It is important to quantify the influence of the indenter orientation on the derive mechanical properties. As shown by Legendre and Dutilleul [57], mathematical expressions based on the sine functions are sometimes used to model periodic phenomena. Therefore, a sine function based on an damped oscillator (i.e., Meschede et al. [68]) in the following form was implemented:

$$y(x) = A + y_0 \sin(2\pi T^{-1}x + \phi_0) \quad (5.9)$$

In this equation x corresponds to the azimuthal angle, ϕ_0 is the phase, A the y -offset, T the period and y_0 the amplitude of the sine function. The function is fitted to the experimental data with the scaled Lavenberg–Marquardt algorithm by “SciDAVis 1.2” software. Additionally, the coefficient of determination R^2 (portion of the variance unexplained by the fit function) and standard deviation σ were determined by the software for each data set.

Korsunsky model

The film-substrate model developed by Korsunsky [53] as expressed in equation (2.20) was used for fitting the hardness-depth data. Thereby, the measured hardness H_{eff} is expressed as a function of indentation depth h . The model in a linear form is reproduced as follows:

$$H_{eff}(h) = H_s + (H_f - H_s) \left(1 + \alpha^{-1} h^2 t^{-1}\right)^{-1} \quad (5.10)$$

Exponential model

The exponential model presented in equation (2.21) was used for fitting of the hardness-depth data as an alternative to the Korsunsky model. In this thesis, it was used in a slightly adapted form:

$$H_{eff}(h) = H_s + (H_f - H_s) \exp(-h/m) \quad (5.11)$$

The parameters H_{eff} , H_f and h are analogous to the Korsunsky model and m is the factor describing the shape of the exponential function, i.e. the hardness decrease. Both, the Korsunsky and the exponential model were numerically fitted to the depth-hardness data with the nonlinear least squares (NLLS) LMA as implemented in the fit module of the Gnuplot software.

Chapter 6

Influence of the Nanoindenter Setup and Sample Preparation

Parts of the following section are adapted from Practical Metallography, Vol 57, Issue 6, 397-414, Filippov, P., Kiderlen S., Koch U., © Carl Hanser Verlag GmbH & Co.KG, München [24]

6.1 Introduction

To provide reliable experimental results possible sources of error must be eliminated or minimized. Influences which may have an effect on the nanoindentation of aluminum are examined in this chapter. Two aspects of the experimental setup are elaborated in this chapter. At first, the electropolishing procedure used for sample preparation is evaluated. The resulting surface roughness and the cold work introduced by grinding/polishing are quantified. Then the influence of the nanoindentation setup, especially the influence of the SDH described in section 5.5.2 (*edge influence* and *stamp effect* illustrated in Figure 5.8) are evaluated. Finally, a set of parameters for electropolishing as well as minimum sample dimensions are established to yield reliable results, is deduced from the results. This parameter set was verified by highly reproducible and low standard deviation measurements on an actual indentation array and was subsequently used for further investigations.

6.2 Results

6.2.1 Surface quality

Al5N-Poly samples were recrystallized, embedded and electropolished (section 5.3). To study the influence of sample preparation, at first the sample surface was investigated by light microscopy and SEM. For roughness analysis the AFM-method as described in section 5.4.1 was used. The influence of residual cold work from prior sample preparation steps

(separation, plane grinding) on electropolished surfaces was analyzed by pop-in analysis. Occurrence of the pop-in effect was analyzed in a 10×10 array with a Vickers indentation and using parameters from section 5.5.5.

Electropolishing of aluminum surfaces resulted in clean and scratch-free polycrystalline aluminum surfaces. Any visible traces of the mechanical pre-treatment were completely eliminated (Figure 6.1 (a)). Through electropolishing approximately $30 \mu\text{m}$ of the material thickness was removed (measured optically). Overall, the light microscopy and SEM images show randomly oriented equiaxial grains with evenly distributed grain size (Figure 6.1 (a),(b)).

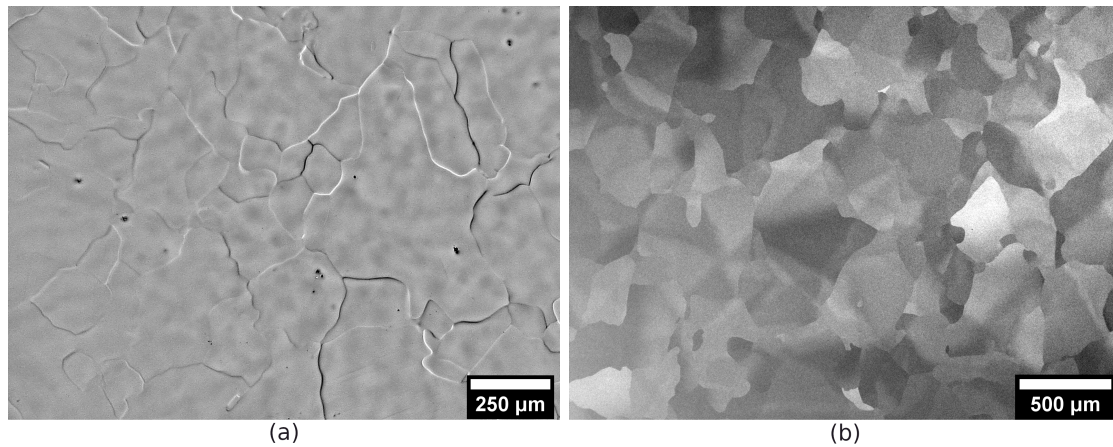


Figure 6.1: Images of electropolished Al5N surface: (a) Reflected light microscopy (b) SEM image

The three dimensional shape (topography) of Al5N-Poly surfaces has been imaged and roughness determined as described in section 5.4.1. A representative AFM image demonstrates a very smooth sample surface (Figure 6.2). Upon closer examination, grain boundaries can be recognized in the AFM image with a small height difference, typically below 20 nm . R_a calculated over a distance of $100 \mu\text{m}$ (vertical profile in the center of the image) is below 1 nm (Table 6.1).

Table 6.1: Roughness values determined based on three AFM images (one example shown in Figure 6.2)

Nr.	R_a (nm)	$20 \cdot R_a$ (nm)
1	0.61	12.2
2	0.95	19.0
3	0.79	15.8

As expected, pop-ins occur mostly at a very low penetration depth of approx. $20\text{-}40 \text{ nm}$. In load-displacement curves (Figure 6.3) the displacement bursts are recognizable at a load of approx. $50 \mu\text{N}$. The pop-in effect could be identified in 97% of the analyzed curves.

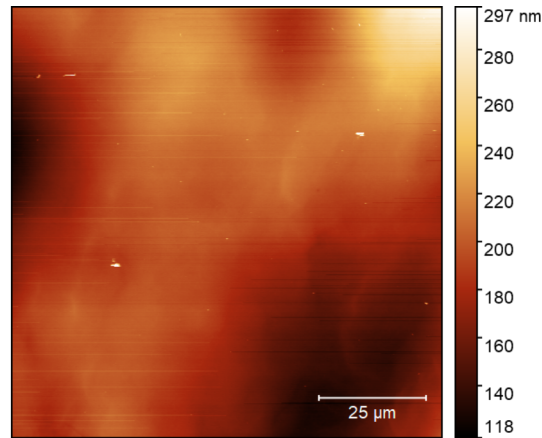


Figure 6.2: AFM image of an electropolished ultra-pure aluminum surface with a height difference of approx. 180 nm between the lowest and the highest point

6.2.2 Influence of the nanoindenter

The influence of the SDH was investigated experimentally by quantifying the edge-influence and the stamp-effect mentioned in section 5.5.2. The reliability of deduced mechanical properties was analyzed as the function of the distance to the edge. Then the maximum indentation area as restricted due to the stamp effect was determined by geometrical considerations (Figure 6.5) and experimentally.

The distance from the edge required to achieve reliable results was determined by performing a series of indentations starting on the resin and finishing on the metallic specimen with the “basic” indentation parameters. For each impression, H_{IT} and E_{IT} and the working distance h_0 (relative position of the indenter in the measurement head) were determined. The distance l is the denotes the position of the each indent. The resulting profile shown in Figure 6.4 can be divided into three sections: A, B, and C. This division becomes particularly apparent when the working distance h_0 changes (Figure 6.4 (c)). In the zone A the SDH and the indenter are placed on the resin. The interface between resin and metal sample can be identified at $l \approx 1$ mm. Zone B is a transition zone, where the indenter is already placed on the metal sample while the SDH is still placed on the resin. In zone C, the SDH and the indenter are both placed on the metal sample, whereby h_0 and E_{IT} only stabilize at $l \geq 5$ mm. This corresponds to a distance from the edge of at least 4 mm.

To quantify the stamp effect the area available for array indentation can be estimated by geometric considerations as shown in Figure 6.5. The indentation array is defined as the quadratic area between point A and B along the diagonal. The margin of the SDH which makes an impression on the specimen surface is shown as a black circle. The indentation array must fit into the black circle, otherwise indentation on a damaged surface can occur. With the SDH-radius r_A , L corresponds to the maximum array size. Based on simple geometric considerations for a quadratic array $L = r_A \cdot \sin(45^\circ)$. According to the specifications of the SDH dimensions $r_A = 1.3$ mm which results in $L = 0.9$ mm.

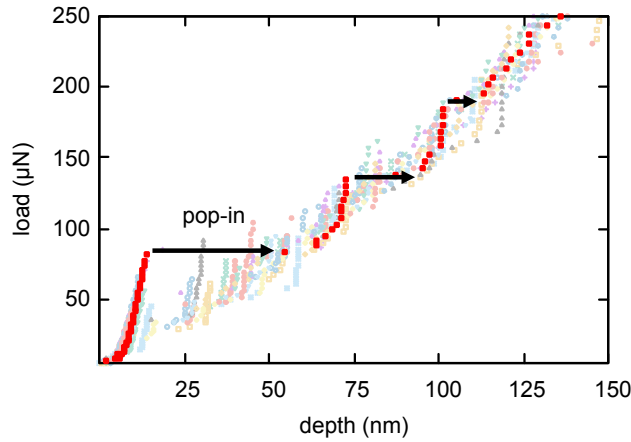


Figure 6.3: Typical load-depth curves used for the pop-in analysis (curves 1-15). Pop-ins on an exemplary data set (red rectangles) marking the transition from elastic (0-25 nm) to elastic-plastic deformation (> 25 nm) are marked with arrows. Multiple pop-ins observed on some curves can be attributed to subsequent dislocation events.

This represents the maximum size of a quadratic array which can be examined in ductile materials. This value was verified by determining the respective r_A from micrographs of square 10×10 arrays with an edge length of 1.0 mm. r_A^* , determined twice on three arrays, respectively, is between 2.1 mm and 2.7 mm which results in a L between 1.5 mm and 1.9 mm. Given $L_{min} = 1.5$ mm, an estimated surface of 2.2 mm^2 is thus available. Figure 6.6 presents an array on which r_A^* was determined (including the resulting surface area).

6.2.3 Indentation results on optimized sample geometry

Optimal sample dimensions have been deduced from the above findings and actual samples were produced and measured by an 1 mm wide 10×10 indentation array. An overview of the so obtained results is shown in Figure 6.6 where stamp effect (impressions from the SDH) is clearly visible. However, the impressions are located outside the indentation array. The variation of h_0 across this sample, illustrated as a heat map in Figure 6.7, shows no systematic behavior. Differences in height (minimum to maximum) within the indentation array remain below $1 \mu\text{m}$. This value is of the same order of magnitude as the height variation in the AFM measurement and thus represents the sample roughness (waviness). Figure 6.8 shows mean values of the mechanical properties H_{IT} and E_{IT} for three samples including the standard deviation. The values obtained for the three samples are well reproducible between samples and show little scattering without an indication of significant systematic effects. Fitting a Gaussian function to the distributions obtained from 300 measurements results in corresponding experimental values of $H_{IT} = 240.1 \pm 5.5$ MPa and $E_{IT} = 63.5 \pm 0.9$ GPa.

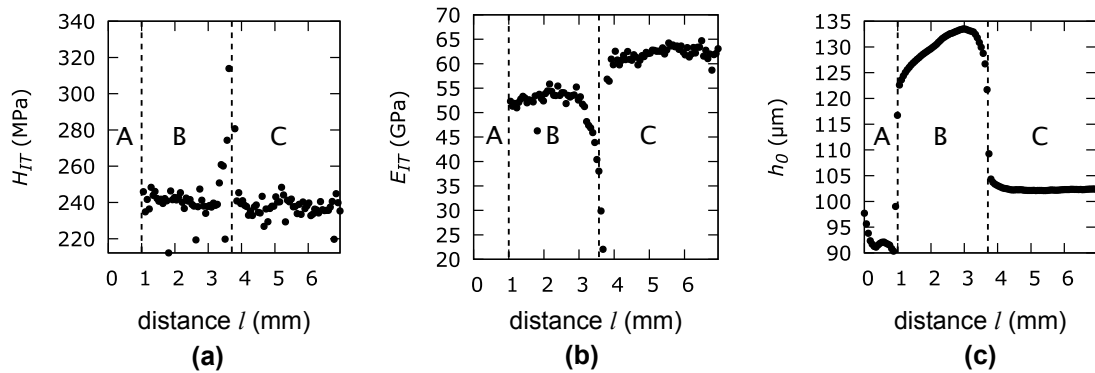


Figure 6.4: Indentation profile from the embedding epoxy to the specimen. Overall ca. 120 indentations over a distance l of 7 mm from start to the end were acquired. Different parameters are plotted as a function of the distance l : (a) Indentation hardness H_{IT} , (b) Indentation modulus E_{IT} and (c) Absolute indenter displacement h_0 .

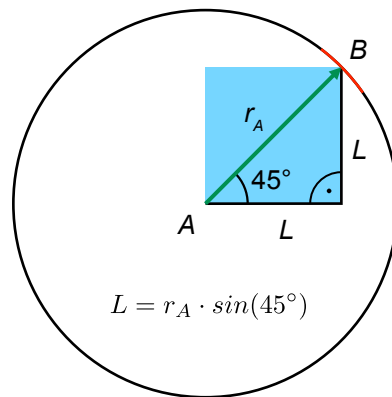


Figure 6.5: Illustration of the maximum allowed area of the indentation array due to the stamp effect. The array starts at the point A and ends at the point B. The circle corresponds to the inner rim of the SDH when the indenter tip is positioned in point A. L is the maximum allowed indentation array width and r_A is the SDH-radius. The available area is highlighted in blue (according to section 6.2.2).

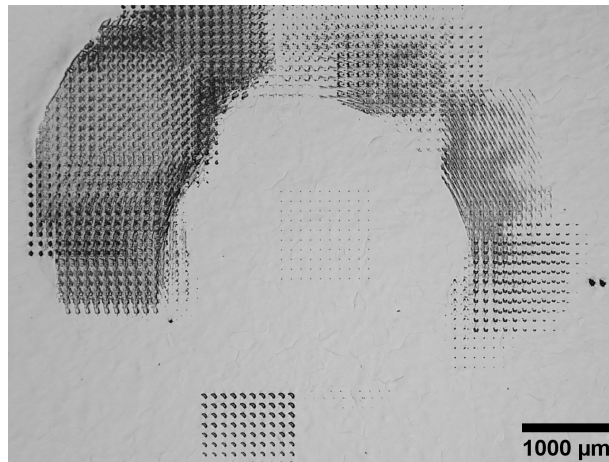


Figure 6.6: Reflected light microscopy image of a 10×10 indentation array on the Al5N-Poly sample surface subject to the stamp effect. The indentation array in the center is surrounded by impressions of the SDH.

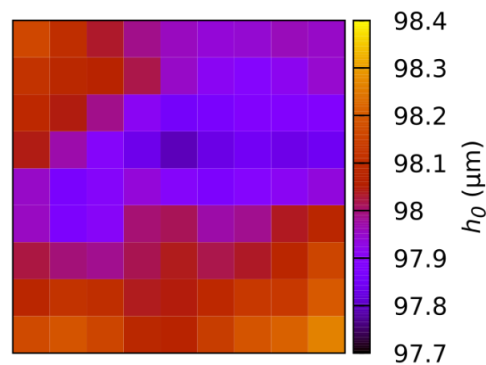


Figure 6.7: Mapping of the absolute vertical position of the indenter (working distance) h_0 . Square 10×10 1 mm wide nanoindentation array obtained on electropolished Al5N-Poly sample (recrystallized by the manufacturer). Maximum height difference is approx. 700 nm.

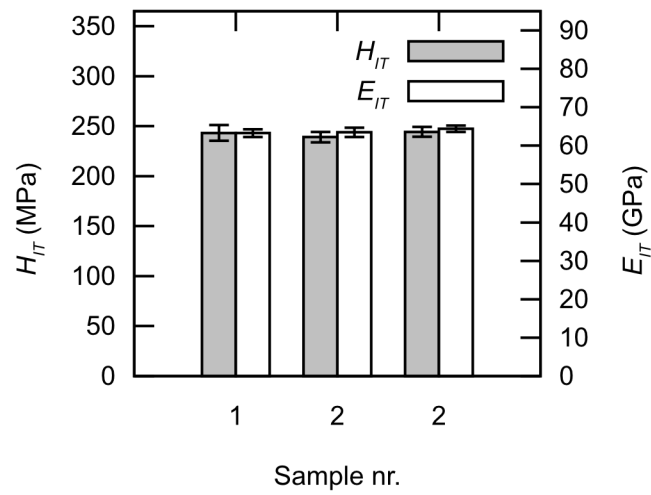


Figure 6.8: H_{IT} and E_{IT} of recrystallized Al5N acquired on three independent samples. Mean values are determined from 10×10 indentation arrays per sample. Error bars denote standard deviations. This plot confirms a low sample-to-sample variation, suggesting high reproducibility.

6.3 Discussion

Electropolishing provided scratch-free Al5N-Poly surfaces with low roughness. The brightness contrast in optical microscopy images outlines grain boundaries indicating an average grain size above 100 μm . The indent size is significantly smaller than the grain size. Accordingly, the impact of grain boundary strengthening on nanoindentation can be neglected. The differences in height at grain boundaries are negligibly small, therefore the differences in brightness at the grain boundaries visible on the optical images are an optical effect (different light reflection). To minimize measurement errors, ISO 14577-2 recommends the minimum indentation depth h_{min} to be at least 20 times the R_a of the measured surface ($h_{min} = 20 \cdot R_a$). For R_a of electropolished Al5N this results approximately in $h_{min} \approx 16 \text{ nm}$. This is about two orders of magnitude smaller than the average indentation depth on Al5N (approx. 1.2 μm), therefore the ISO requirement is more than met.

In their work Langitan and Lawn [56] found that the surface layer thickness impacted by the mechanical abrasion corresponds to approximately half of the nominal grit size of the abrasive. The smallest grit size used for mechanical sample preparation of aluminum samples in this work was 10 μm (P2500 abrasive paper). Hence, it would be sufficient to remove $> 5 \mu\text{m}$ of the surface to eliminate the deformation layer. With the applied electropolishing procedure approx. 30 μm from the aluminum surface was removed. Thus, the deformation layer was removed completely. This is supported by a pronounced pop-in effect observed in almost all measurements.¹

Concerning the edge influence of the SDH, H_{IT} is influenced only marginally. This is noticeable by the sudden H_{IT} -increase when the SDH is positioned at the interface between the resin and the metal. This is different for E_{IT} : It can only be measured reliably with the SDH positioned completely on the metal surface. This indicates that the main influence is on the measured contact stiffness, but not the contact area. Therefore, for reliable E_{IT} measurements on electropolished microsections a distance of 4 mm from the edge is necessary. The maximum array size is limited to 1.5 mm \times 1.5 mm by the stamp effect. This value was determined experimentally (Figure 6.6) and is different from the geometrically estimated value (based on the dimensions of the SDH provided by the supplier). The reason is that the SDH rather exerts pressure with its outer rim, whereas the manufacturer's specifications refer to its inner rim. This finding can be summarized in the minimum sample dimensions necessary to obtain reliable measurement with the given experimental setup. The minimum size of a quadratic sample is 9.5 mm \times 9.5 mm resulting from a 4 mm margin on each side due to the edge influence, plus 1.5 mm for the indentation array at the center of the sample.

As a result, the H_{IT} and E_{IT} measurements provide reproducible values with low variance. The remaining variance can be attributed to the measurement accuracy (noise of the electronics, remaining vibrations, accuracy of the zero-point determination). Another possible influence not further discussed in this section is the dependence of measured values

¹Although $F_{max} = 500 \mu\text{N}$ applied here is also sufficient for the study's objective, visibility of the pop-ins could be further improved by applying a smaller load. $F_{max} = 250 \mu\text{N}$ is recommended for recrystallized high purity aluminum.

on the grain and indenter orientation. Statistical evaluation of all measurements provided mean values that are readily comparable with data from literature for H_{IT} obtained from aluminum single crystals according to Liu et al. [60] and Vlassak et al. [95].

6.4 Conclusions

Ultra-pure aluminum was electropolished, whereby the deformed layer could be removed completely. A low dislocation density of the so prepared surfaces could be verified by means of the pop-in analysis. The obtained surfaces are extraordinarily smooth with sub-nanometer R_a values. Hence, electropolishing is well suitable as a preparation technique for nanoindentation of ultra-pure aluminum providing smooth low-defect surfaces.

Electropolishing leaves a step at the metal/resin interface. This step has an impact on the measurement result and in particular on E_{IT} . The negative influence can be avoided by working with a distance of more than 4 mm from the edge. In addition, the stamp effect restricts the measurable surface area to 1.5 mm \times 1.5 mm at most. For an indentation array of this size positioned in the sample center a square sample with an edge length of at least 9.5 mm is necessary.

The combination of electropolishing for sample preparation and careful choice of sample geometry to avoid edge influence and the stamp effect made it possible to unleash the full potential of the Picodentor. The indentation hardness of $H_{IT} = 240.1 \pm 5.5$ MPa as well as the indentation modulus $E_{IT} = 63.5 \pm 0.9$ GPa obtained by 10×10 arrays on three independent samples are reproducible and show a low standard deviation below 3 %. Additionally, these values are in good agreement with the literature sources.

Chapter 7

Impact of the Relative Orientation Between Indenter and Crystal Lattice

Parts of the following section are adapted from Filippov, P.; Koch, U. Nanoindentation of Aluminum Single Crystals: Experimental Study on Influencing Factors. Materials (Basel). 2019, 12, 3688. [25]

7.1 Introduction

In this chapter, the experimental base for indentation analysis of aluminum has been established by studies on surfaces of single crystals. Therefore, the effect of the relative orientation between crystal and indenter on measured hardness and modulus is evaluated. The objective was to transfer these results to polycrystalline aluminum that is examined in the next chapter. To achieve this, the magnitude of both effects, namely the orientation indentation direction and the azimuthal indenter orientation relative to the crystal lattice, must be studied separately.

At first, the effect of crystal orientation on H_{IT} and E_{IT} has been investigated (data set “crystal orientation”). Indentation hardness and modulus data were acquired by Vickers array indentation (6×6 array indentation procedure, section 5.5.5) on oriented Al5N-SX samples (orientations: (100), (110), (111)). The average hardness and modulus are then compared to the directional Young’s modulus (section 3.2.1) and estimated indentation modulus (calculated according to Delafargue and Ulm [15], section 3.2.3).

In a polycrystalline material the grains are oriented randomly, therefore the orientation of the indenter in respect to the lattice of the grain is also random. To model this experimentally via indentation of single crystals the combined effect of the azimuthal indenter orientation relative to the crystal orientation was quantified (data set “azimuthal orientation”). The experimental data were acquired by rotating the sample in respect to the Vickers indenter by 175° steps in increments of 5° (randomized). According to Wang et al. [98], a coupled effect of indenter geometry (Vickers, Berkovich, conical) and crystal-

lographic orientation of the indented material is expected. To quantify this effect a sine function from section 5.6 was fitted to the orientation dependent hardness and modulus data.

7.2 Results

7.2.1 Quality of sample preparation and pile-up corrections

The crystal orientation and integrity were verified prior to the actual measurements using microscopical images of the pile-up patterns indents made for this purpose. The surface preparation quality was investigated via pop-in analysis as discussed in section 5.5.5. These additional tests proved necessary because of the high susceptibility of aluminum to mechanical damage during sample preparation.

Two exemplary monocrystalline (111) oriented aluminum specimens were electrolytically and mechanically polished. The effect of surface preparation on the pop-in behavior is obvious from exemplary indentation curves of mechanically and electrolytically polished Al5N surfaces (Figure 7.1). The indentation curve of the mechanically prepared sample shows a continuous increase of depth with applied load. The electropolished sample showed a pronounced displacement burst at an applied load of 250 μN . This is also observable in-situ in the actual indentation curves shown in Figure 7.5.

To verify the quality of the surface preparation, the pop-in effect was analyzed quantitatively. The proportion of load-depth curves with pronounced pop-ins were determined from both curve sets: (1) crystal orientation and (2) azimuthal indenter orientation. This results in an average pop-in occurrence of 97% (Table 7.1). This observation is in accordance with the work of Pathak et al. [73], who compared two methods of sample preparation. They decided to use vibrational polishing in favor of electropolishing in order to suppress pop-ins. In our work this was not necessary since pop-ins affect indentation curves only at a low indentation depth below 200 nm. Here, we use the occurrence of the pop-in effect as an in-situ indicator for the sample preparation quality.

Table 7.1: Proportion of the load-depth curves that exhibit pop-ins. The analysis is based on the curves from two data sets dealing with the influence of relative (1) crystal orientation and (2) the azimuthal orientation between the indenter and the sample.

Data set	Orientation		
	(100)	(110)	(111)
(1) Crystal orientation	100%	98%	97%
(2) Azimuthal orientation	97%	100%	100%

The surface morphology around the indents was analyzed by optical microscopy. The original indents made with $F_{\text{max}} = 10 \text{ mN}$ and $h_{\text{max}} \approx 1.2 \mu\text{m}$ are too small to be captured optically. To overcome this problem, indents were made with a higher F_{max} of 60 mN

and analyzed in Figure 7.2. Kucharsky and Jarzabek [54] demonstrated in their work that the pile-up patterns with loads higher than 2 mN mainly resemble the crystal symmetry (Berkovich indentation of copper single crystals). This holds true in case of the original indents at 10 mN as well as in the case of higher load indents at 60 mN made for optical imaging where F_{max} is also above 2 mN. Therefore, no significant difference of pile-up patterns is expected. For this reason, it is acceptable to investigate pile-up patterns with a higher load and extrapolate the findings to the actual measurements. Microscopic images of pile-up patterns on (100)-, (110)-, and (111)-oriented specimens resemble to the four-, two-, and three-fold crystal symmetry of the respective surface. The images of mis-aligned indenter/crystal configuration (Figure 7.2 (d)-(f)) exhibit surface deformation patterns that are almost identical to the aligned indents. On one side the findings of Kucharsky and Jarzabek are verified. On the other side the sample preparation, including orientation of the single crystal and electropolishing succeeded in preserving integrity of the single crystal and the correct orientation.

Since pure low-defect aluminum has a high strain-hardening rate, pile-up corrections have to be considered. The usefulness of the corrections according to the McElhaney and Tuck method has been investigated as described in (section 5.5.7) and compared to the Oliver-Pharr method. Following the McElhaney method, the actual effect of material plasticity on the contact area has been investigated (Figure 7.3). The SEM image depicts an indentation on a (100)-oriented sample with A_p (solid line) being smaller than A_c (dashed line) resulting in an α -factor of less than 1. The summarized results for the α -factor (Figure 7.4) confirm this trend ($A_p < A_c$) for all indenter-sample configurations. Furthermore, α is dependent on the indenter orientation for the crystal orientation (100) and (110). No such dependency is observed for the more isotropic (111)-orientation. Further, h_p (plastic height) and H_p (true hardness) determined according to the Tuck method are shown in Table 7.2. Since no major differences in plasticity is expected between the indents made on the same single crystal, one representative indentation curve in the (110) orientation has been analyzed. The resulting h_p (Tuck) is higher than the cross sectional h_c determined by the Oliver and Pharr method which indicates a pile-up. The consequence of the different contact depth is that the determined H_p is slightly lower than H_{IT} .

Table 7.2: Determined h_p and H_t ($F_{max} = 10$ mN, (110) direction) in comparison to h_c and H_{IT} determined according to the method of Oliver and Pharr.

h_c	h_p	H_{IT}	H_p
1.24 μm	1.28 μm	249.5 MPa	235.2 MPa

7.2.2 Influence of the crystal orientation

The indentation curves from which the statistical data have been derived are shown in Figure 7.5. The curves show good reproducibility, no visible influence from vibrations and a recognizable pop-in effect in the low-load region. Average H_{IT} values for particular

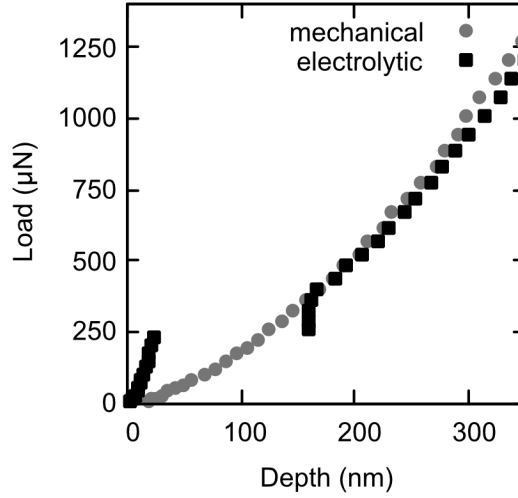


Figure 7.1: Indentation load-displacement curves on the aluminum (111)-single-crystal surface electrolytically (electropolished) and mechanically polished samples. A discontinuity at a load of approx. 250 μN can be observed only for the electropolished sample, whereas the mechanically polished sample shows a continuous load-depth behavior.

crystallographic orientations are summarized in Figure 7.6. Indentations on the (100)-, (110)-, and (111)-oriented samples result in hardness values ($H_{IT} \pm \sigma_{H_{IT}}$) of 256.0 ± 2.2 MPa, 269.6 ± 5.9 MPa, and 261.6 ± 2.7 MPa respectively. The (110)-oriented sample has not only the highest hardness, but also the highest standard deviation. The average hardness over all crystallographic orientations accounts to 262.4 MPa with a range $R_{H_{IT}} = H_{IT,max} - H_{IT,min} = 13.6$ MPa (5.1%). The range $R_{H_{IT}}$ is converted to a standard deviation according to the range rule of thumb mentioned by Mandel [65] with $R \approx 4\sigma$. The derived σ accounts to approximately 1.3% relative to the average hardness. Assuming that $R_{H_{IT}}$ originates solely from crystal orientation, the so derived σ can be expected for statistical indentation on polycrystalline material with randomly oriented grains.

Average values of M with the corresponding standard deviations are shown in Figure 7.7. The (100), (110), and (111) orientations result in the indentation modulus values ($M \pm \sigma_M$) of 73.6 ± 0.9 GPa, 75.5 ± 1.1 GPa, and 76.9 ± 1.4 GPa respectively. The absolute values for M differ from the theoretical values for $E_{uvw}/(1 - \nu^2)$ as shown in Table 7.4. However, the experimental values show the same trend with the (110) orientation being elastically the weakest and (111) the stiffest. Analogous to H_{IT} , the average indentation modulus over all orientations is 74.5 GPa with a range $R_M = 3.3$ GPa (4.4%), and the overall standard deviation derived from crystallographic orientations is approximately 1.1%. This corresponds to the expected σ for array indentation on polycrystalline material with randomly oriented grains.

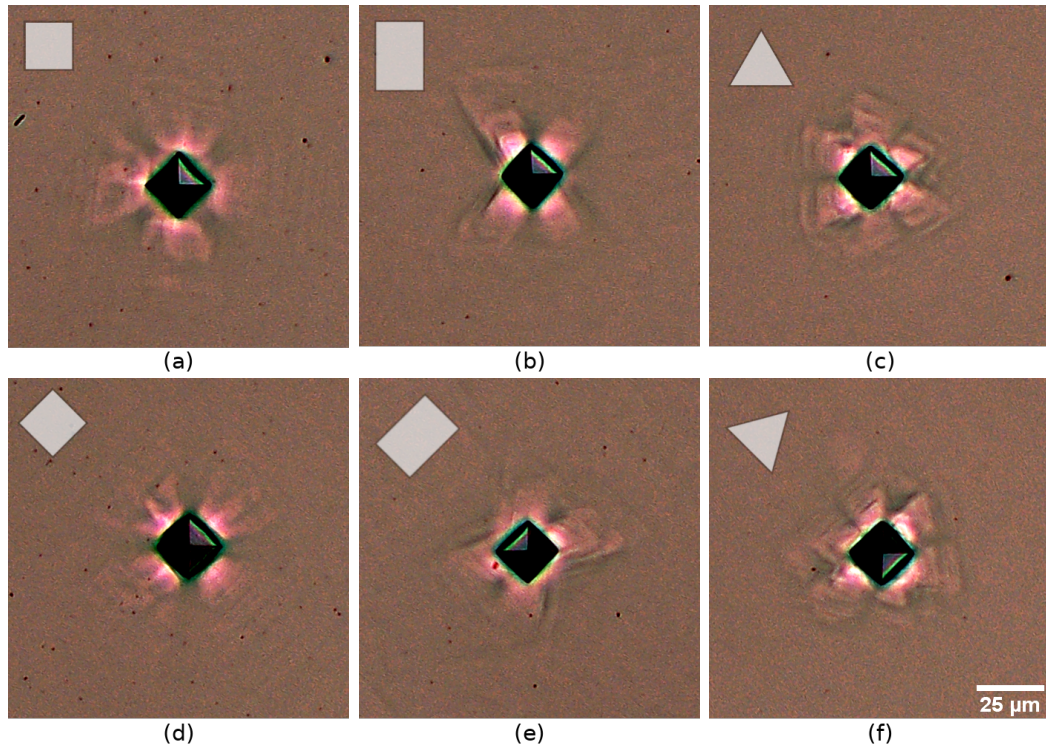


Figure 7.2: Optical images of pile-up patterns ($F_{\max} = 60 \text{ mN}$) on three crystallographic orientations of aluminum single crystals. Indenter and crystal lattice in aligned configuration: **(a)**: (100), **(b)**: (110), **(c)**: (111). Indents on the same surfaces with the sample azimuthally rotated by 45° clockwise resulting in mis-aligned patterns: **(d)**: (100), **(e)**: (110), **(f)**: (111). Although the relative orientation of the quadratic Vickers indenter relative to the crystal has been change, the resulting pile-up patterns still resemble the underlying crystal symmetry. The symbol in the upper left corner of each image (square, rectangle, triangle) illustrates the crystal symmetry and it's orientation in respect to the indentrr.

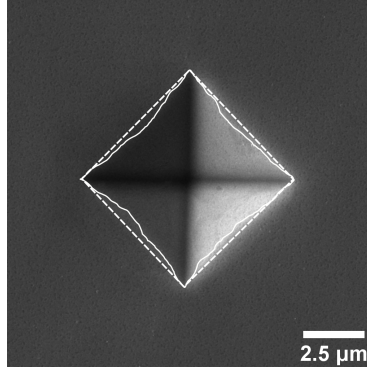


Figure 7.3: SEM image of the indented area ($F_{max} = 10$ mN) on the crystallographic (100) orientation of aluminum single crystal (aligned). A_p is outlined by the solid and A_c by the dashed line.

7.2.3 Influence of the indenter orientation

H_{IT} and M are plotted as a function of the azimuthal indenter orientation in Figures 7.8 and 7.9 respectively. The absolute values are normalized with respect to the average of the corresponding data-set for better comparison. The harmonic function from Equation 5.9 is fitted to the rotational data and is shown as a green line. The determination coefficient R^2 is plotted on each graph to represent fit quality.

Transferred to the effect of the azimuthal indenter orientation on H_{IT} and M the sine function parameters from equation (5.9) are interpreted as follows. In general, y represents either H_{IT} or M as the function of the orientation angle x . The y -axis-offset A represents the average value of H_{IT} or M (normalized in Figures 7.8 and 7.9). The amplitude y_0 is correlated to the magnitude of the combined effect of the crystal orientation and indenter geometry. The phase angle ϕ_0 is the phase shift of the azimuthal indenter orientation. The period T was fixed at 90° (quadratic Vickers-pyramid). H_{IT} and M vary periodically with the azimuthal indenter orientation for the (100)- and (110)-oriented samples, where two periods can be distinguished for these orientations for the investigated rotation range. By contrast, no periodicity is observed for the (111)-oriented sample i.e. the amplitude (if present) is below the scatter of the data.

Each data set has outliers. In the preliminary test, an attempt was made to remove the outliers manually, but there was no significant improvement of R^2 in the fitting result. Therefore, the fits were performed on the raw data sets. equation (5.9) could be fitted successfully to the experimental data from (100)- and (110)-oriented samples. The R^2 of the fits lies between 12% and 46%. No satisfactory fit result could be achieved for the (111) orientation ($R^2 < 10$). Additionally, residual analysis was performed (see Figure C.1 in chapter C). The error is evenly distributed along the indenter-sample orientation for H_{IT} and M on the (100) orientation, with no systematic effects. For the (110) orientation the spread increases slightly from 150° to 185° (E_{IT} and M). The residual analysis was not performed for the (111) orientation since it could not be fitted.

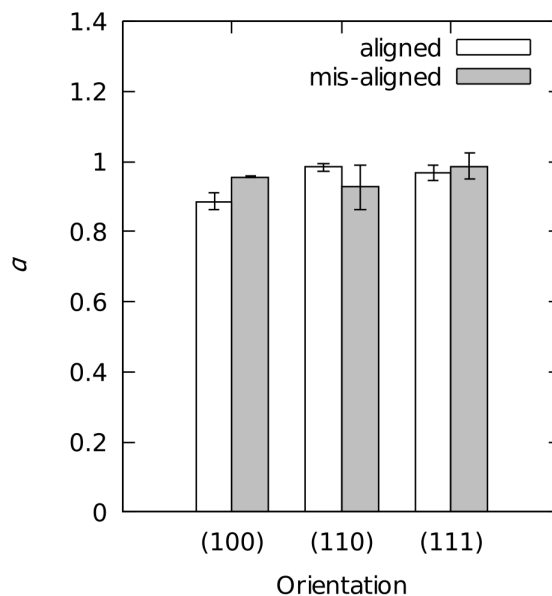


Figure 7.4: Dependence of the factor α on the crystal and indenter orientation. Average values with the error bar indicating the respective range ($\alpha_{max} - \alpha_{min}$).

The period of the fitted function is 90° for all sample orientations, which conforms to the geometry of the indenter (quadratic pyramid) which verifies, that the periodicity is associated with the indenter-lattice orientation. σ and the fitted x_0 values for the (100) and (110) orientations are shown in Table 7.3. The fitted x_0 is partially higher than half of the corresponding σ , hence the periodic effect is significant.

Table 7.3: Values of the fitted parameters x_0 in comparison to σ of the corresponding data sets from the measurement series of the azimuthal indenter orientation influence on H_{IT} and M .

Orientation	H_{IT}		M	
	σ	x_0	σ	x_0
(100)	1.7%	1.6%	2.6%	1.3%
(110)	2.0%	1.0%	2.6%	1.8%

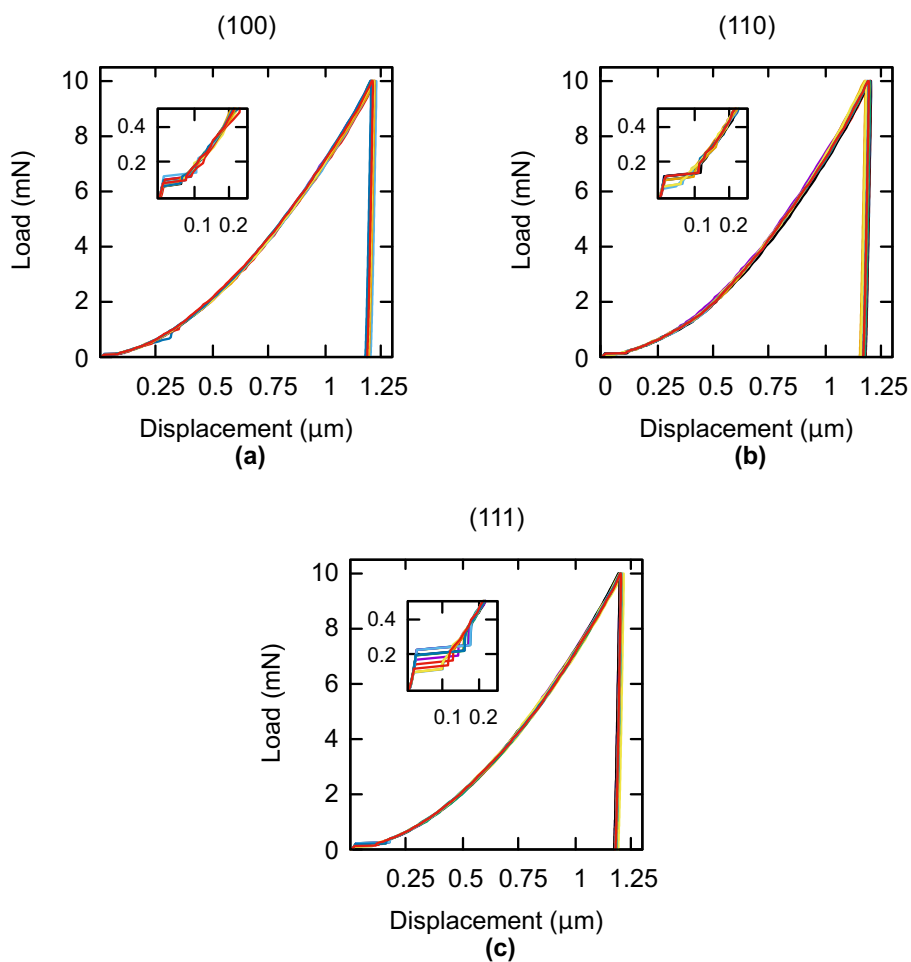


Figure 7.5: Indentation curves produced with the 6×6 arrays on differently oriented Al single crystal surfaces: (a) (100) orientation, (b) (110) orientation, and (c) (111) orientation. The initial portion of the curves is shown in the insets to visualize the pop-ins.

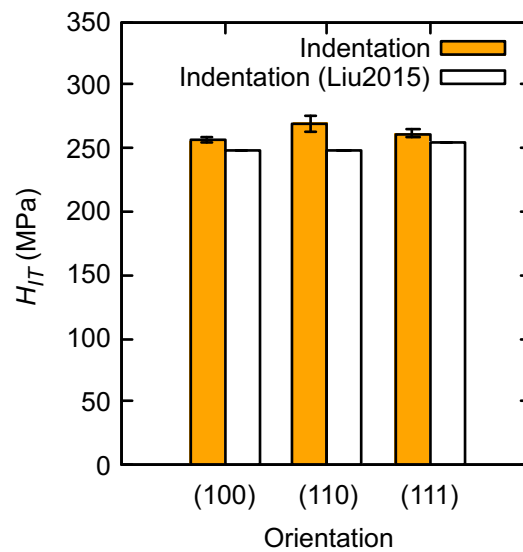


Figure 7.6: Comparison of experimental H_{IT} for three crystallographic orientations of the aluminum single crystal to literature values (orange: this study, white: Liu et al. [60]). No information about the measurement error was available for [60].

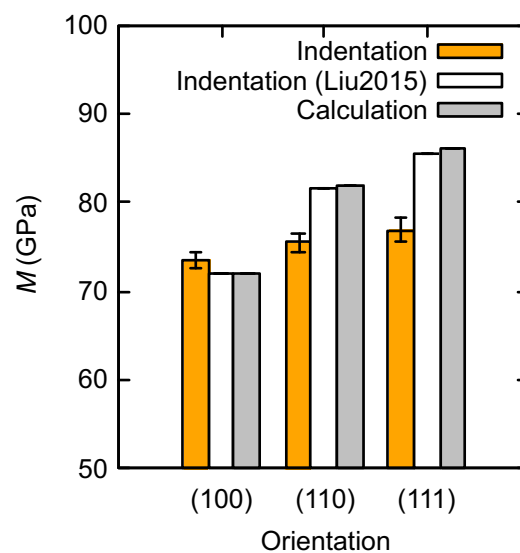


Figure 7.7: Comparison of experimental M for three crystallographic orientations of the aluminum single crystal with theory and literature values. Orange: this study (experimental M), white: Liu et al. [60] (experimental M), grey: calculated M according to equation (3.4). No information about the measurement error was available for [60].

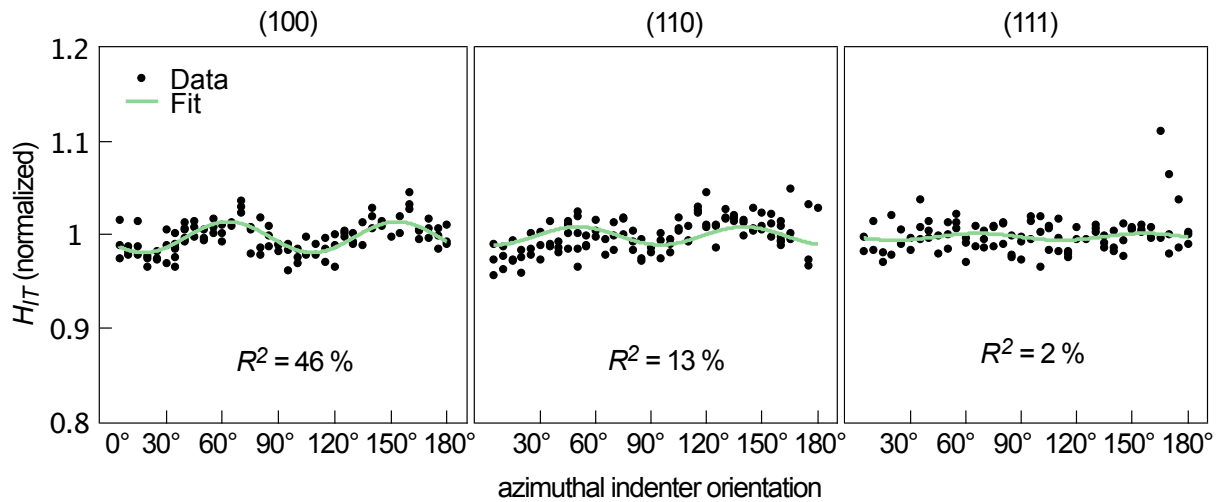


Figure 7.8: Measured H_{IT} (normalized to their respective mean values) as a function of the azimuthal indenter orientation on three crystallographic orientations. Black dots represent data points; solid lines represent fits according to equation (5.9).

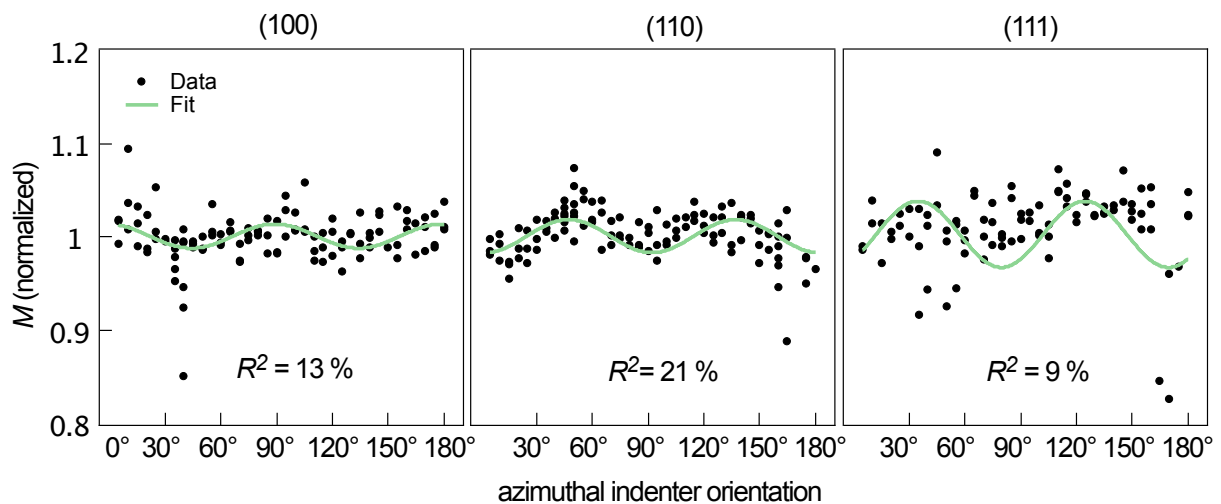


Figure 7.9: Measured M (normalized to their respective mean values) as a function of the azimuthal indenter orientation on three crystallographic orientations. Black dots represent data points; solid lines represent fits according to equation (5.9).

7.3 Discussion

As judged by the analysis of the pop-in behavior, i.e. pronounced pop-ins in 97% of load–depth curves, the applied sample preparation is appropriate. On the other side pop-ins affect the first 100–200 nm of the indentation curves. However, this influence is negligible since typical indentation depth used to determine H_{IT} and M was above 1100 nm. Further, possible influences from surface oxides and the remains of the polishing agents are not expected to significantly influence mechanical properties at applied indentation depths and therefore are not part of these studies.

The correct sample orientation and the integrity of the crystal lattice can be confirmed on the basis of the pile-up patterns. Characteristic pile-up patterns on all three crystallographic orientations indicate the respective crystallographic surface orientation almost independently from the azimuthal indenter orientation. Therefore, plastic deformation depends mainly on the crystallographic orientation, but not on the indenter orientation. This applies for the chosen indentation depth of approx. 1200 nm which complies with the findings of Wang et al. [98] and Kucharski and Jarzabek [54].

Methods for contact area correction delivered contradictive results. From both, the SEM image of the indent (Figure 7.3) and α factors determined according to the McElhaney method (Figure 7.4), sink-ins are evident. The magnitude of the sink-in depends on azimuthal indenter orientation. In contrast to this, h_p and H_p values determined according to the Tuck method as in [93], clearly indicate a pile-up, not a sink-in. However, the McElhaney method based on SEM images is more reliable, hence the calculation of H_p according to Tuck must be error-prone. Since α shows a complex behavior depending on both the crystallographic orientation of the sample and the azimuthal orientation of the indenter, H_{IT} and M results cannot be corrected with a single factor. To reasonably apply the α -factor for corrections, an SEM-images of every indent has to be acquired and evaluated according to the proposal of McElhaney et al. [66]. However, this was not necessary in our work, because α deviates only slightly from 1. Therefore, the pile-up/sink-in correction can be neglected. Nevertheless, it should be kept in mind that the deduced H_{IT} and M values are slightly underestimated because of the observed sink-in effect.

The acquired hardness data are in good agreement with the results reported by Liu et al. in 2015 [60], but are systematically lower than the results reported by Liu in 2014 [59]. In these references, however, the surface quality was not analyzed through pop-in analysis and no information about data scatter is provided. It is assumed that the deviation of our hardness values to reported ones originates in different sample preparation.

On the (111)-oriented samples the indentation direction is perpendicular to the slip direction of the fcc slip system, as mentioned by Rösler et al. [76] (slip plane of the type $\{111\}$, slip direction of type $\langle 1\bar{1}0 \rangle$). Therefore, this crystallographic orientation should exhibit the highest hardness. Instead, in our results, the (110)-oriented sample exhibits the highest average H_{IT} . One possible explanation may be that the hardness anisotropy is not very pronounced on Al and the effect is partially covered by higher data scatter on the (110)-oriented sample. Overall, the experimentally determined hardness values are

probably close to the intrinsic material properties. In addition, the standard deviation achieved in this study is very low relative to the absolute hardness values.

To evaluate the magnitude of the averaging effect and crystal anisotropy the experimental data are compared with the calculated Young's moduli in the respective direction (according to Equation 3.4), indentation moduli (according to Equations 3.6 and 3.7), and two literature sources (see Table 7.4). Additionally, a ratio of the stiff to the weak direction M_{111}/M_{100} has been introduced in Table 7.4 to compare the derived anisotropy of the different elastic moduli. The absolute indentation moduli are slightly lower than predicted which can be attributed to the sink-in effect. Nevertheless, the resulting experimental M_{111}/M_{100} ratio shows a very good agreement with theory and it is only slightly higher than M_{111}/M_{100} approximated indentation moduli.

Table 7.4: Comparison of M_{uvw} values obtained in this study compared to the literature. The values are given with the precision of the corresponding original publication.

Method	Equation	(100)	(110)	(111)	M_{111}/M_{100}	Ref.
$\frac{E_{[uvw]}}{1-\nu^2}$, calculated	3.4	72.6	82.5	86.5	1.191 (E_{111}/E_{100})	
$M_{[uvw]}$, calculated	3.6, 3.7	79.1	82.5	86.5	1.019	this study
M , experimental	2.12	73.6 ± 0.9	75.5 ± 1.1	77.0 ± 1.4	1.046	
M , experimental	2.12	71.8	81.6	85.4	1.189	[60, 59]
M , experimental	2.12	77		79	1.015	[94]
M , numeric approx.	-	79	80	81	1.029	[94]

A significant difference of the M_{111}/M_{100} ratios obtained in this study to values by Liu et al. [60, 59] must be noted. Their results almost completely agrees with the value of the directional Young's modulus. However, this does not consider the averaging effect, neither experimentally nor by FEM. Accordingly, the M_{111}/M_{100} should be lower than the E_{111}/E_{100} ratio, as discussed in Section 3.2.3. This relation is corroborated by our results. Furthermore, the obtained data are in good agreement with the experimental and theoretical results of Vlassak and Nix [94]. The information about how elastic anisotropy is altered by the averaging effect is very important, because it is necessary to understand and describe the behavior of material close to the real-life conditions. These results are an important prerequisite for a better understanding of material behavior and as such can be implemented in the indentation data spread analysis of polycrystalline material.

The influence of the indenter orientation on the indentation modulus was calculated by Vlassak and Nix [94] for cubic single crystals indented with a flat triangular punch indenter (three-fold symmetry). However, to the best of our knowledge no experimental studies on the influence of the azimuthal indenter orientation on mechanical properties of single crystal aluminum are reported. The chosen sine function has proven suitable for describing the influence of the azimuthal indenter orientation on hardness for the (100)- and

(110)-oriented specimens. Consequently, large part of the data scatter could be explained by the periodic influence of the azimuthal indenter orientation.

We demonstrate experimentally that the indenter orientation has a measurable effect on H_{IT} and M (Figures 7.8 and 7.9). Clear evidence is provided by the match of the observed effect to the indenter symmetry. Additionally, the periodic modulation of hardness and indentation modulus only occurs on (100)- and (110)-oriented specimens whose symmetry (four-fold and two-fold) is compatible to the four-fold symmetry of the quadratic pyramid of the Vickers indenter. Therefore, the periodic behavior of the measured parameters is attributed to the combined effect of indenter and surface symmetry. These findings extend the results of Wang et al. [98] on copper single crystals to aluminum, and quantify the effect on H_{IT} and M . The further analysis of the slip systems, elastic anisotropy in three dimensions, as well as possible determination of elastic constants from the nanoindentation experiments, which are the physical basis for the observed anisotropy, is beyond the scope of this study.

7.4 Conclusions

Sample preparation quality has been investigated based on pile-up patterns (crystal integrity) and the pop-in effect (dislocation density). It could be demonstrated, that the used combination of mechanical and electrolytic sample preparation does not affect the hardness and modulus measured by nanoindentation. Regarding the contact area correction, it must be noted, that none of the prevalent methods could be applied due to the direction dependent pile-up and sink-in behavior.

The indentation hardness was found to increase by 7.3% relative to the average hardness due to the effect of crystallographic orientation. This would result in a data scatter of polycrystalline material with randomly oriented grains of $\sigma = 1.8\%$. The variation of indentation modulus on three different crystallographic orientations was attributed to elastic anisotropy. The anisotropy of the indentation modulus is diminished due to the indentation averaging effect which is correctly predicted by the data analysis model.

The interplay of 2 and 4 fold symmetries of the crystal and the indenter results in periodic behavior. By fitting a harmonic function to these data, a significant part of variation could be explained by the effect of the azimuthal orientation of the indenter. For the first time, it is possible to quantify this effect on based on experimental Vickers-indentation data of aluminum single crystals.

In order to transfer single influences found in this study to pure polycrystalline aluminum, respective samples should be examined by array nanoindentation. The variation of hardness and indentation modulus on polycrystalline aluminum should be compared with the influences determined in on single crystals in the current chapter. Further insights which could be gained from the influence of dislocation density on plastic behavior should be considered.

Chapter 8

Evaluation of Stress Induced Microstructures and Mechanical Properties of Polycrystalline Aluminum

8.1 Introduction

Important influencing factors on indentation hardness and modulus of monocrystalline aluminum were studied in chapter 7. These results build a basis for understanding nanoindentation experiments of aluminum. In the next step, complexity of the investigated material must be increased towards technical alloys. To face this objective, polycrystalline aluminum was compressed to different states of deformation and investigated. The results were interpreted in the context of prior findings obtained on monocrystalline aluminum which are published in [25] (chapter 7) and general continuum plasticity theory.

Polycrystalline aluminum consists of differently oriented grains i.e. crystallites. Due to low concentration of contaminants, the material complexity is increased only by two factors as compared to monocrystalline aluminum. These are the grain orientation with respect to the indentation direction and the grain boundaries (see grain boundary strengthening described in section 3.4.1). To take these studies one step further towards technical alloys, the material has been uniaxially deformed by a degree of deformation η of 10%, 20%, 30%, 40% 50% and 75 %. This introduces different densities of dislocations into the material by strain-hardening as discussed in section 3.4.1 and induces changes in the microstructure.

The specimens were separated, embedded and electropolished to remove the deformation layer. Stress-induced microstructure evolution of electropolished specimens was also studied by optical microscopy. Indentation hardness and modulus at the indentation depth was determined analogous to [25] via Berkovich indentation using the “basic” parameter set. Additionally, a multi-step indentation technique was performed on the material to

acquire depth-dependent mechanical properties and thus establish a reference for further experiments.

8.2 Results

8.2.1 Microstructure of compressively deformed polycrystalline aluminum

The microstructure observed in compressed aluminum specimens is inhomogeneous as illustrated in Figure 8.1. Two types of grains can be observed in optical microscopy. Based on the appearance in optical micrographs (reflected light) the grains are described as smooth u-type grains (undeformed) and rough d-type grains (deformed). The evolution of the microstructure of recrystallized aluminum with the degree of deformation η ranging from 0% to 75% is shown in Figure 8.2. Grain size measurements shown no significant change of the grain size with the degree of deformation. However, the relative amounts of u-type and the d-type grains show a certain development. Notably, a few d-type grains are discernible in the recrystallized sample (Figure 8.2) which can be related to residual cold work from the production process. These d-type grains are almost indiscernible for recrystallized unstrained aluminum ($\eta = 0\%$), and became only visible for specimens with $\eta \geq 20\%$. Complementary, proportion of smooth grains (u-type, undeformed) decreases with the degree of deformation.

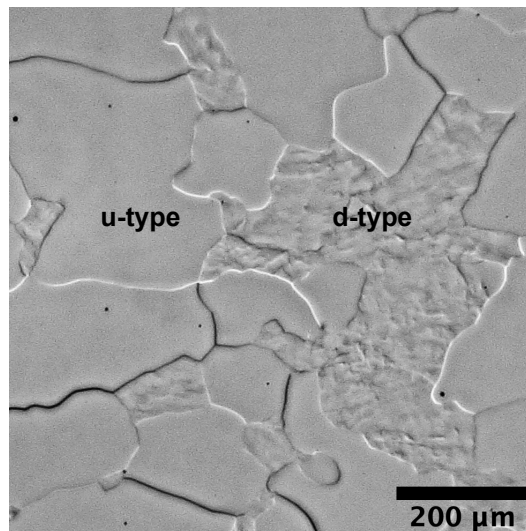


Figure 8.1: Optical microscopy image (reflected light) of a recrystallized and uniaxially compressed Al5N-Poly specimen. Two types of grains are apparent: the smooth u-type and rough d-type.

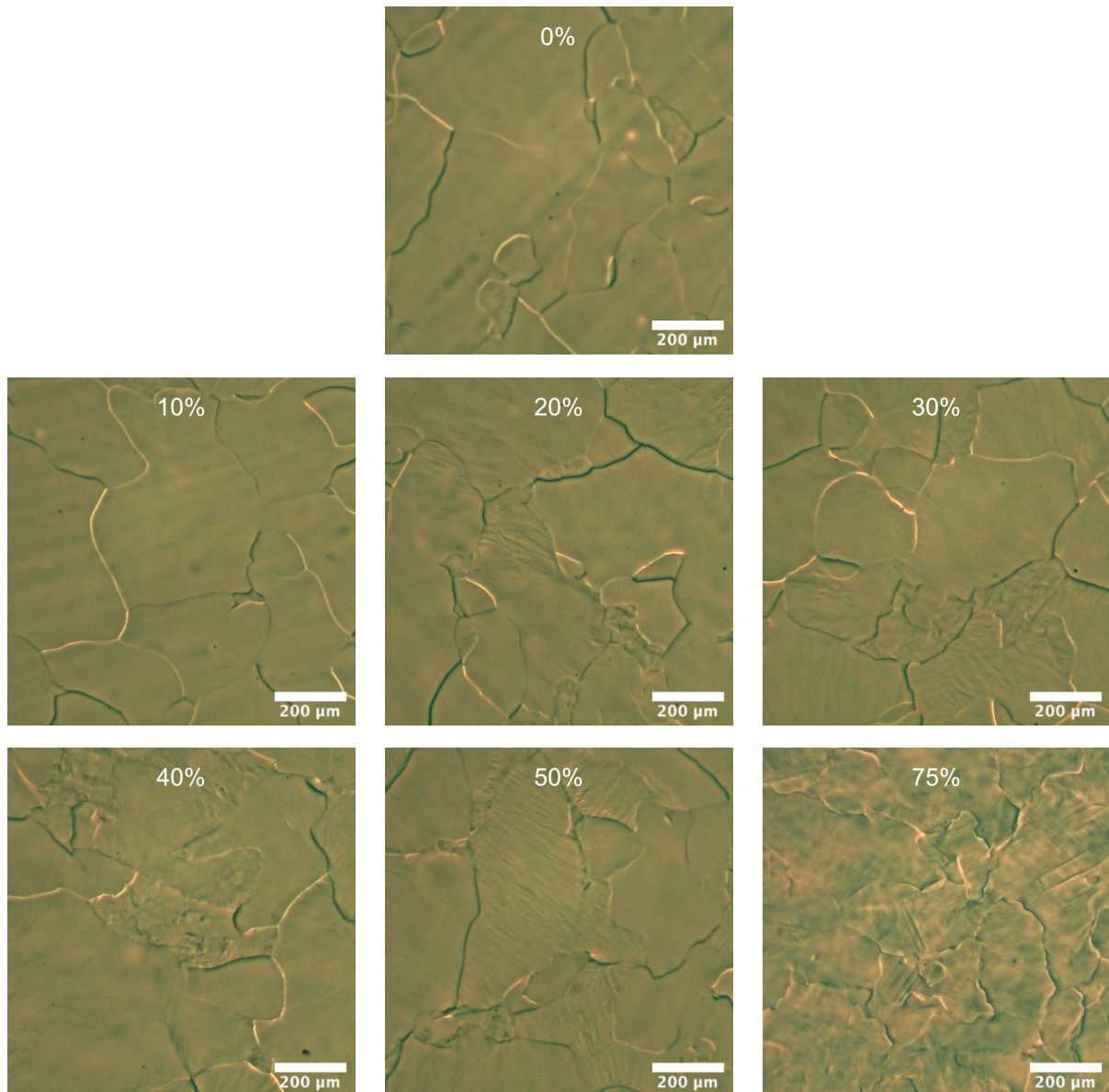


Figure 8.2: Optical microscopy images demonstrating the evolution of the microstructure of polycrystalline aluminum subject to uniaxial compression. The η in % is denoted in the top of the respective image. The compression direction is perpendicular to the image plain.

8.2.2 “Basic” indentation

1 mm wide 10×10 indentation arrays with the “basic” parameter set from Table 5.6 (section 5.5.5, $F_{max} = 10\text{mN}$) in the center each specimen were performed to obtain experimental data. H_{IT} and E_{IT} values from 100 Berkovich indentations on each specimen exhibit pronounced data scatter for each degree of deformation (Figure 8.5). Two main sources of these variations have been identified: the influence of “indentation creep” (see explanation below) and significantly different hardness values of the u-type versus d-type grains.

In Figure 8.3 E_{IT} is plotted as the function of the post-indentation creep C_{IT} , i.e. relative change of the indentation depth while F_{min} is held constant for 20 s after unloading. A clear dependency between E_{IT} and C_{IT} is visible for data points with $C_{IT} < -1\%$ (Figure 8.3, red circles) as a roughly linear increase of E_{IT} with C_{IT} . However, E_{IT} is stable for data-points with $C_{IT} > -1\%$ (Figure 8.3, blue circles) i.e. scatters around a certain average value without considerable slope. Consequently, only data points with $C_{IT} > -1$ have been included in further analysis to minimize this effect. It must be noted, that no dependency of H_{IT} on C_{IT} and was observed indicating that the H_{IT} measurement is less susceptible to drift than E_{IT} .

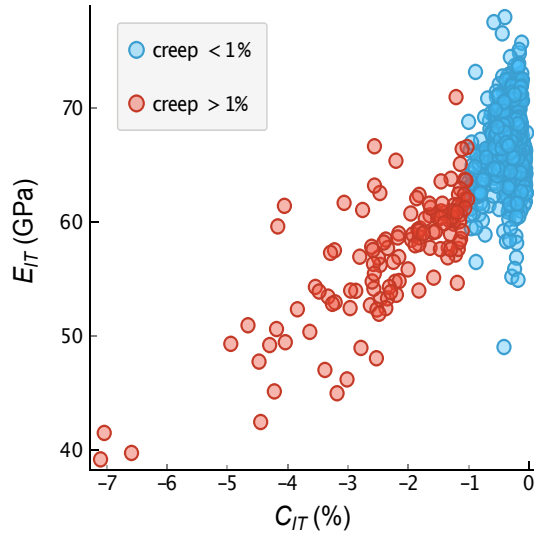


Figure 8.3: Plot of E_{IT} as a function of post-indentation creep C_{IT} demonstrating non-desired dependency of E_{IT} on C_{IT} . Data with $C_{IT} < -1\%$ were excluded from the analysis. Data jittering along the x-axis is added to prevent overlay of single data points.

Microscopic characterization of indentations made with an increased $F_{max} = 100$ mN revealed significant differences in the morphology of pile-up patterns around the indent. Two types of indent morphologies already apparent in the microstructural images (Figure 8.2) also can be distinguished from the optical microscopy images of the indents (Figure 8.4). Indentations on the d-type grains show smaller contact areas with the pile-up pattern largely dependent on the indenter geometry (three-sided Berkovich pyramid) and orienta-

tion. By contrast, indents on the u-type grains have larger contact areas and the respective pile-up morphology depends on the crystal orientation of the indented grain relative to the indentation direction. These two types of indent morphologies correspond to two different classes of hardness values with d-type indents having systematically higher H_{IT} and u-type indents lower H_{IT} . The properties of both types of indents are summarized in Table 8.1.

Table 8.1: Characteristic features of indentation on the u-type and d-type grains.

	u-type:	d-type:
Contact area	large	small
Pile-up patterns	crystal oriented	indenter oriented
Hardness	low	high
Morphology	smooth	rough

According to the microscopy images, each data point has been assigned either to d-type or u-type grains. Moreover, each data point has been classified according to the observed creep value ($C_{IT} > -1\%$ or $C_{IT} < -1\%$) and indent morphology (u-type or d-type). The completely assigned data-set is summarized in Figure 8.5. Based on this data set, average H_{IT} and E_{IT} with their standard deviations were determined for each pile-up and grain type. Data-points with $C_{IT} < -1\%$ (red circles in Figure 8.5) were discarded.

The calculated average values of H_{IT} and E_{IT} are shown in Figure 8.6 for different η . The data scatter has decreased significantly after filtering and separating data into subsets. Averaged H_{IT} values demonstrate correlation of the d-type grain hardness to the degree of deformation up to 75%. At the same time, H_{IT} of the u-type grains remains unaffected showing a constant value for all degrees of deformations. The E_{IT} -data shown in Figure 8.6 (b) acquired on specimen with different η show pronounced data scatter which varies from specimen to specimen. This effect is attributed to the not optimal sample geometry, as discussed in chapter 6. Nonetheless, there is no systematic dependency of E_{IT} on different η .

8.2.3 Multi-step indentation

Depth-dependent H_{IT} obtained by multi-step indentation with $F_{max} = 100\text{mN}$ applied in 20 intermediate loading steps (section 5.5.6) demonstrate a correlation between the degree of deformation and hardness analogous to the “basic” indentations with a single F_{max} (Figure 8.7). Additionally, a measurable increase of H_{IT} is observed with decreasing indentation depth which also increases with the degree of deformation. It is especially pronounced for $\eta = 75\%$ i.e. the largest deformation. Two groups of curves are observable for $\eta > 50\%$ while the gap between them is most significant at $\eta = 75\%$. This corresponds well with the microstructure evolution and the “basic” indentation. Analogous to the “basic” indentation we do not find a dependency between η and indentation modulus M (Figure 8.8). Additionally, M exhibits a significant decline at lower indentation depth. This effect increases with the degree of deformation and is most pronounced for $\eta = 50\%$.

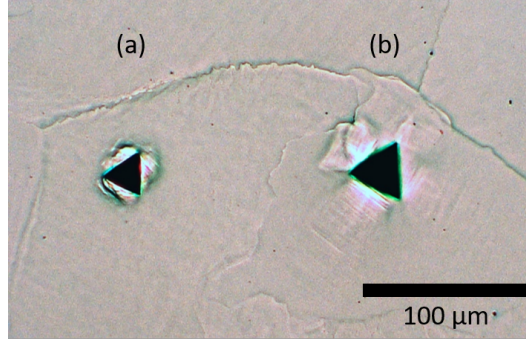


Figure 8.4: Optical microscopy of indentations with $F_{max} = 100mN$ on recrystallized and compressed ($\eta = 50\%$) Al5N-Poly. **(a)** Indent on a d-type grain (smaller area, pile-up patterns depend on indenter geometry, $H_{IT} = 559$ MPa). **(b)** Indent on a u-type grain (larger area, pile-up patterns depend on the crystallographic grain orientation, $H_{IT} = 207$ MPa).

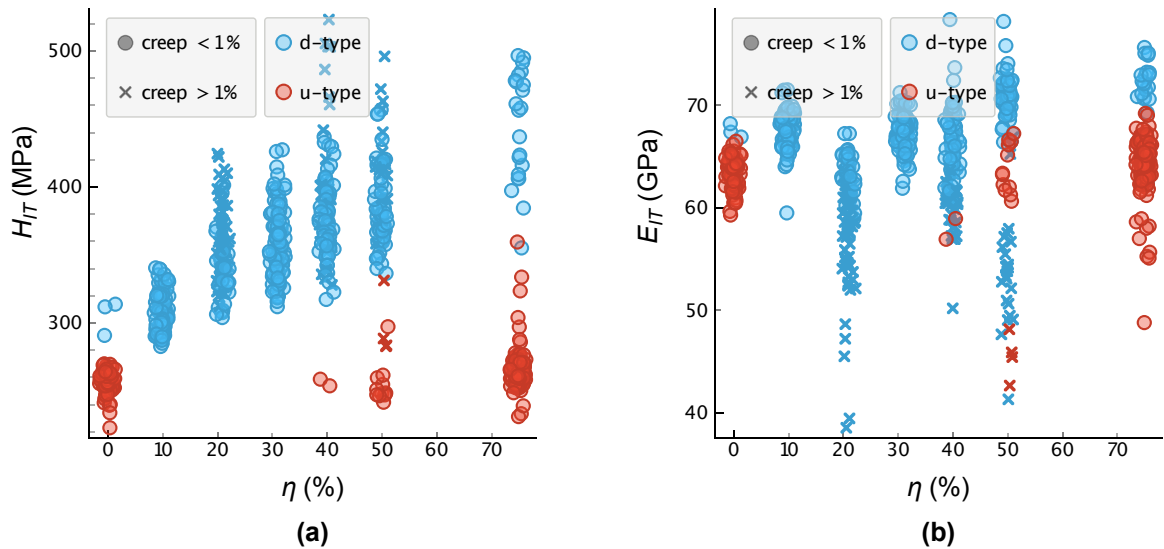


Figure 8.5: Summary of H_{IT} and E_{IT} data as a function of the degree of deformation η . Data points for which $C_{IT} < -1\%$ are excluded from the analysis. Indents of the d-type (blue) are excluded from the 0%-deformation data set, since they are thought to be non-recrystallized regions originating from deformation during sample manufacturing. The u-type indents (red) are excluded from the data sets with $\eta > 0\%$. The Data jittering (x-axis) was applied for better visibility i.e. to prevent overlap of single data points.

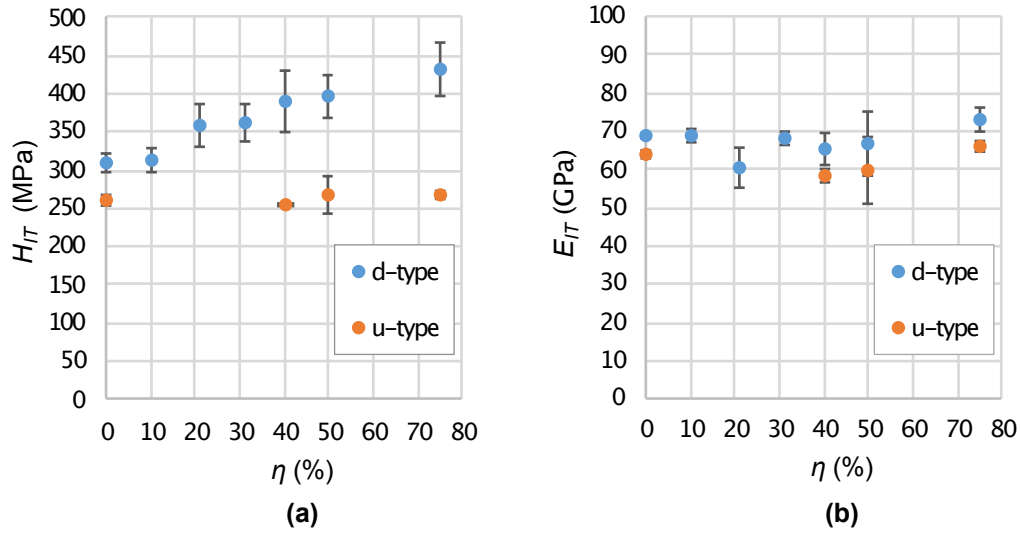


Figure 8.6: Average values for H_{IT} and E_{IT} of compressed Al5N-Poly specimen. The error bars correspond with respective standard deviation. The average values are calculated from low-creep data exclusively.

For $\eta = 75\%$ a significant separation of the curves into two groups with different M is observed. Both curve groups converge to identical M at low indentation depth.

The difference between multistep indentation results of both grain types can be summarized as follows. The d-type grains are relatively hard with H_{IT} increasing with η due to strain-hardening. The mean value of M is independent of η but the results separate into two groups which can be associated with two grain types: the u-type and the d-type. The u-type grains with smooth morphology in optical microscopy images show constant low hardness for all η . The actual H_{IT} values are comparable to that of the recrystallized undeformed material.

8.2.4 Review of the experimental setup

A small fraction of the d-type grains observed on the undeformed recrystallized Al5N-Poly specimen ($\eta = 0\%$ in Figure 8.2) is assigned to residual cold work from rod manufacturing (pulling). This also indicates that the applied recrystallization procedure was insufficient. To resolve this issue, measurements made on these spots have been identified and were excluded from the analysis. The requirements for optimal sample dimensions discussed in chapter 6 could not be met in these experiments because of the limited raw material size (diameter < 10 mm). This is the origin of the indentation creep (Figure 8.3) and the resulting inconsistencies in the indentation modulus ($\eta > 0\%$ in Figure 8.6). The affected data points have also been excluded from the analysis.

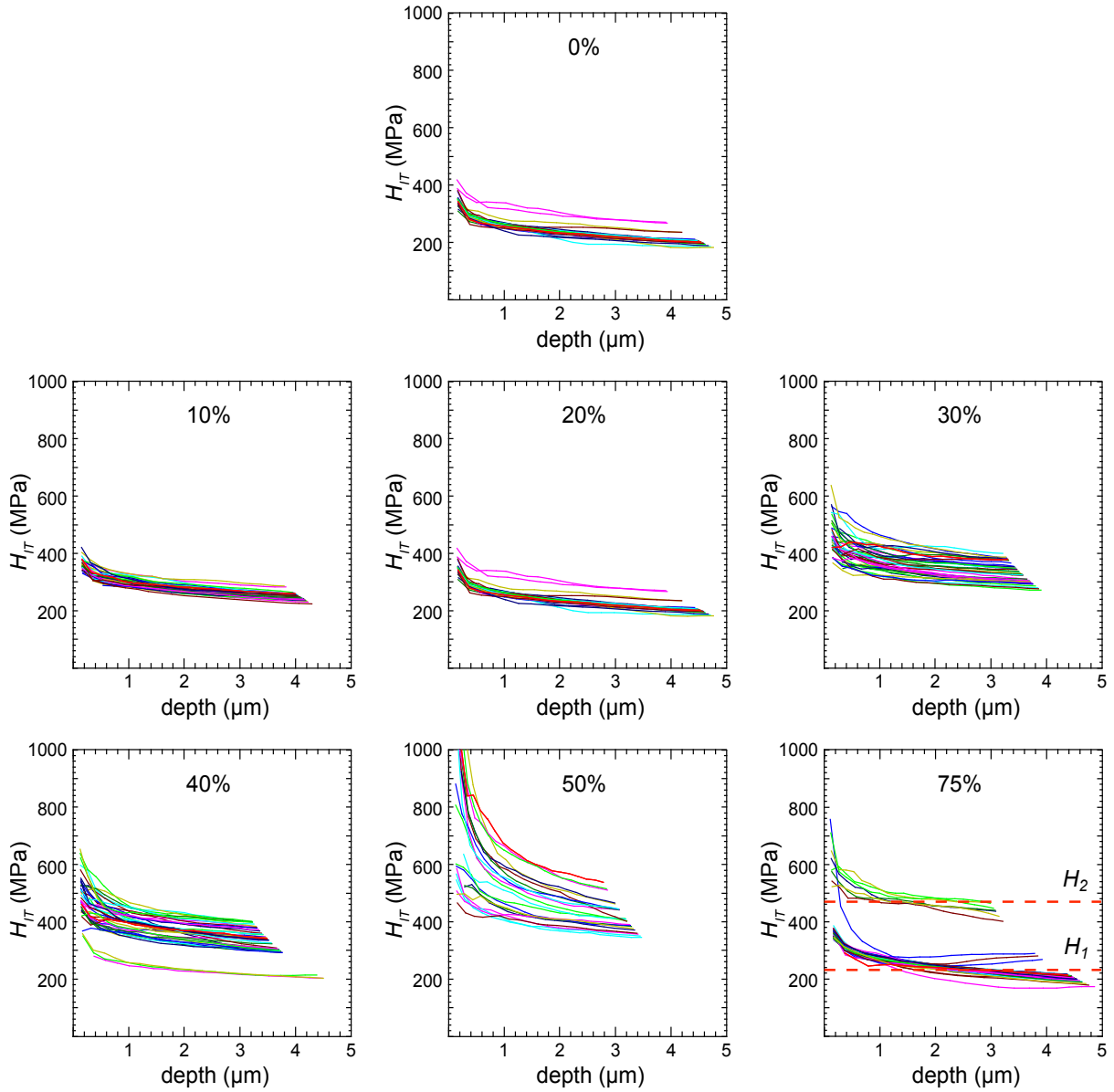


Figure 8.7: H_{IT} versus indentation depth curves obtained from multistep indentations of Al5N-poly specimen with η from 0% to 75% (denoted in the top of the respective graph). For $\eta = 75\%$ the H_{IT} at maximum indentation depth of both groups of curves is approximated as $H_1 = 230$ MPa and $H_2 = 740$ MPa.

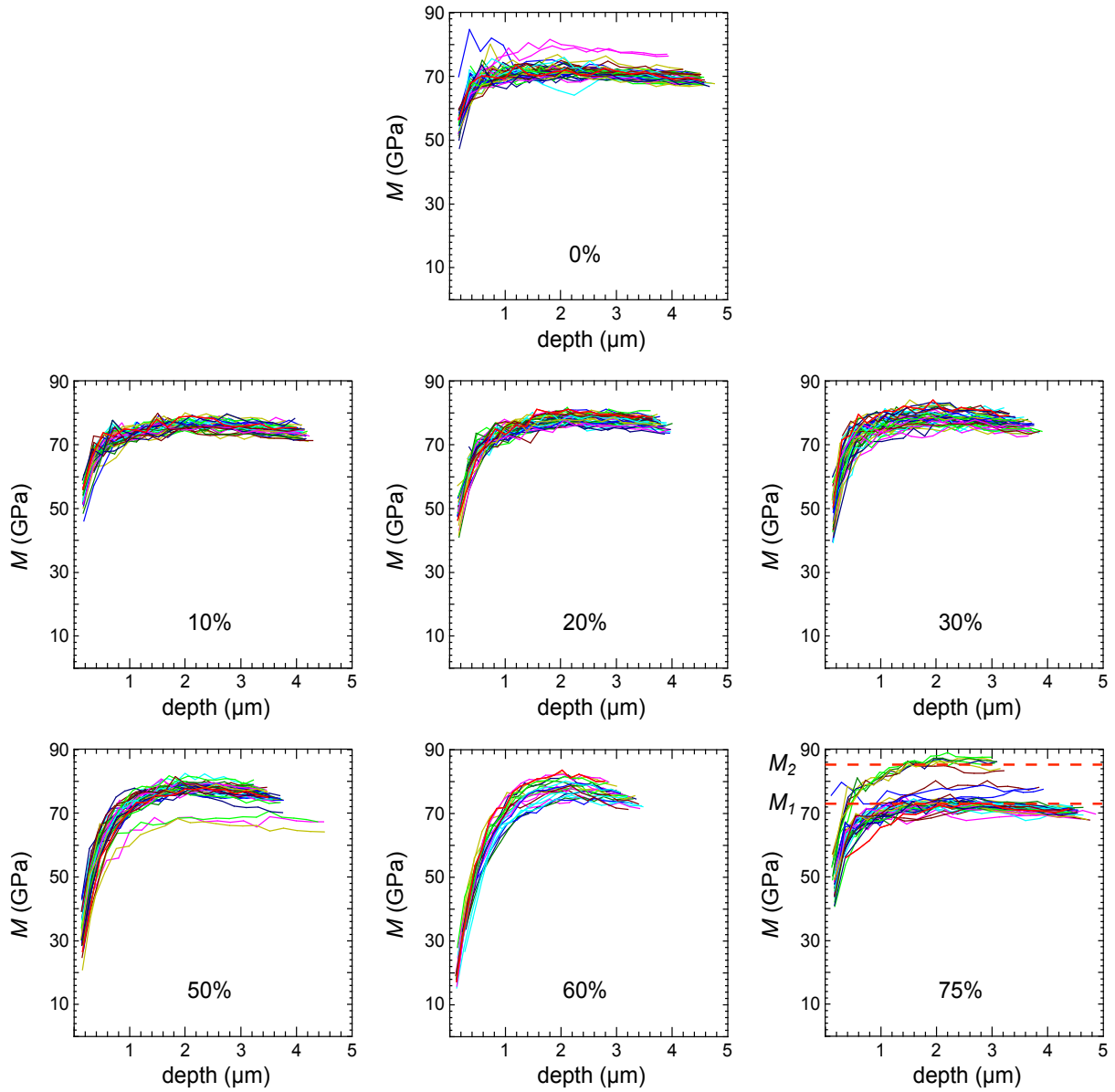


Figure 8.8: M versus indentation depth curves obtained from multistep indentations of Al_5N -poly specimen with η from 0% to 75% (denoted in the top of the respective graph). For $\eta = 75\%$ M at maximum indentation depth of both groups of curves is approximated as $M_1 = 73$ GPa and $M_2 = 85$ GPa.

8.2.5 Influence of indenter geometry

A Berkovich indenter has been used for these experiments. This is different from the experimental procedure used for Al5N-SX crystals described in the previous chapter, where a Vickers indenter was used. However, the H_{IT} and E_{IT} values obtained with both indenter types are in excellent agreement with each other. The mean hardness value obtained on recrystallized Al5N-Poly sample $H_{IT,polycrystalline} = 257$ MPa corresponds well with the single crystal values obtained with the Vickers indenter of $H_{IT,monocrystalline} = 262$ MPa (Figure 7.6 [25]). The same holds true for the indentation modulus obtained with the Berkovich indenter on Al5N-poly with $E_{IT,polycrystalline} = 66.6$ GPa (Figure 8.6) which is in very good agreement with the modulus obtained with the Vickers indenter on Al5N-SX of $E_{IT,monocrystalline} = 66.2$ GPa (Figure 7.7). Hence, the influence of indenter shape on hardness and modulus is insignificant.

8.3 Discussion

Upon uniaxial compression the microstructure and mechanical properties undergo several drastic changes. Generally, the following microstructural processes are expected:

- Homogeneous strain redistribution over the microstructure resulting in strained grains only depending on η .
- Texture/grain rotation in a preferred direction affecting the effective elastic modulus which depends on the preferred crystallographic orientation.
- Homogeneous increase of hardness/dislocation density over all grains and statistic distribution of hardness values.
- Highest hardness for maximum deformation due to strain hardening.

In the experiment, several deviations from theoretical expectations have been observed. Both, the microstructure and mechanical properties evolve heterogeneously throughout the deformation process. A clear separation of microstructure and mechanical properties into two subcategories is evident. To better understand the results, underlying processes of plastic deformation are discussed first.

In the course of uniaxial compression, the grains are flattened in the load direction, resulting in the “pancake” structure (well known from rolled aluminum products; recognizable in a cross-section normal to load direction). Additionally, the crystal lattice of each grain is rotated under stress to accommodate plastic strain. The lattice rotation depends on the orientation of the slip-system with respect to the load direction. During uniaxial compression, the strain direction (i.e. material flow) is normal to the load vector. According to Khan, the highest stress release through dislocation slide in a bcc structure proceeds over a slip-system normal to the load direction ($\{111\}$ slip plane normal to load direction) [50]. The grains in which the $\{111\}$ slip plane is almost normal to the load direction can

accommodate more plastic strain (smooth u-type grains). Accordingly, the grains with the orientation of the $\{111\}$ slip plane being almost parallel to the load direction can accommodate less plastic strain. Dislocation slips occur over sub-optimal slip-systems with the highest Schmidt factor (d-type grains).

The coherent plastic strain along the $\{111\}$ slip plane explains the smooth appearance of u-type grains. This is supported by the parallel slip steps on the surface of the u-type for $\eta = 75\%$ (Figure 8.2). The unfavorably oriented grains of the d-type rely on multiple sub-optimal active slip systems which results in slip steps on the surface, with mixed orientation, producing the rough appearance.

Despite the expected plastic anisotropy of plasticity, the dislocations are distributed homogeneously in the initial stage of deformation. This is evidenced by the statistical distribution of hardness values obtained by “basic” and multistep indentation. Also, the progressing lattice rotation is still not pronounced enough to influence the indentation moduli at this stage. For higher degrees of deformation ($\eta \geq 40\%$), the heterogeneous plastic deformation extends in its effect even on the mechanical properties. Analogous to microstructure, mechanical properties associated with the respective grains separate into two distinct groups i.e. soft, elastically weak u-type and the hard, elastically stiff d-type.

Heterogenization of the microstructure and mechanical properties is anticipated to depend significantly on the initial grain orientation relative to the load direction. As has been mentioned above, the orientation of the slip-plane to the load direction is key to accommodate plastic strain. It is also conceivable, that the initial grain orientation also promotes its lattice rotation to adopt the optimal orientation i.e. $\{111\}$ normal to load direction. This leads to a more effective dislocation slip and therefore higher strain accommodation. Unfavorably oriented grains lag behind since the plastic strain can only be accommodated over sub-optimal slip systems. Hence, the morphology and mechanical properties of the respective grains are different.

Hence, the strain is distributed unevenly throughout the microstructure depending on the relative orientation of the crystal lattice of the grains and the load direction. This also implies that the global degree of deformation η_{global} (applied by the machine) is not equally distributed resulting in local degrees of deformation η_u and η_d for the respective grains. Depending on the orientation of the slip-system relative to the load direction this results in $\eta_d < \eta_{global}$ or $\eta_u > \eta_{global}$. This also implies, that the amounts of strain energy stored in both grain types are different.

However, this would only explain the different grain appearance and orientation dependent strain-hardening of the respective grains. The most unexpected effect is grain softening at higher degrees of deformation. This phenomenon is difficult to explain with grain size, pancaking or uneven direction dependent plastic deformation. According to Sakai and Jonas, dynamic recrystallization (DRX) and dynamic recovery (DRV) both offer possible explanations for high purity aluminum at room temperature [79]. DRX is less probable since it generally requires higher activation energy [7, 6, 104]. Additionally, smaller newly formed grains would be observable on the micrographs, which is not the case. During dynamic recovery the rearrangement and annihilation of dislocations takes

place upon deformation[78]. The resulting reduction of dislocation density is observable as grain softening.

A similar behavior has been observed in ref. [13] on compressed Al single crystals and in ref. [105] during multi-forging process of polycrystalline aluminum (both at room temperature). As mentioned above, the amount of strain energy stored in each grain depends on the initial crystallographic orientation of the grain relative to the load direction. To activate DRV certain activation energy is necessary, therefore DRV is at first activated in favorably oriented grains, which have more stored strain energy. Accordingly, this could explain the effect of heterogeneous grain softening.

The microstructure heterogenization and increasing DRV is most significant for the largest degree of deformation (75%). All microstructural and mechanical properties have entirely separated into two groups depending on the lattice orientation of the respective grain. The orientation with respect to the load direction of the u-type grains increases to a level, where the effect of lattice orientation on the indentation modulus becomes significant. This is evident from the “basic” as well as from the depth-dependent indentation experiments. Because of the clear separation into two groups, the ratio of the indentation moduli can be determined to $M_2/M_1 = 1.16$. It corresponds well with the anisotropy ratio of the single crystal in Table 7.4. Therefore the lattice rotation leading to the different crystallographic orientation of both grain types is evident.

In summary it should be noted, that the maximum achievable strength of aluminum is not limited by the strength/ductility trade-off (i.e. embrittlement upon extensive cold work). The limiting factor turns out to be the softening of the material which counteracts the obtained strain-hardening.

8.4 Conclusions

The influence of uniaxial deformation of high purity polycrystalline aluminum on the microstructure, plastic flow and the resulting mechanical properties has been investigated up to $\eta = 75\%$ including intermediate stages by microscopy and nanoindentation. The plastic flow is strongly anisotropic resulting in heterogeneous microstructure and mechanical properties. The plastic flow of high-purity aluminum is strongly dependent on the orientation of the slip system of each grain with respect to the direction of the load. This results in an uneven distribution of the deformation between favorably and unfavorably oriented grains. In consequence, both the microstructure and mechanical properties separate into two distinct groups. The final orientation of individual grains through lattice rotation and pancaking leads to texturization. For grains oriented with the $\{111\}$ slip system normal to the direction, we observe an anisotropy in the indentation modulus. For the largest degree of deformation ($\eta = 75\%$), pronounced softening counteracts strain hardening. This effect is attributed to dislocation annihilation by discontinuous dynamic recovery.

Chapter 9

Mechanical Characterization of Micromilled AA6082

Parts of the following section are adapted from Filippov, P.; Kaufeld, M.; Ebner, M.; Koch, U. Investigation of the effect of end mill-geometry on roughness and surface strain-hardening of aluminum alloy AA6082. Materials (Basel). 2020, 1–16. [23]

9.1 Introduction

The continuation of the work is to transfer the findings on pure mono- and polycrystalline aluminum to micromilled engineering aluminum alloy AA6082. Since micromilling introduces cold work into the surface leading to hardening, the depth dependence of mechanical properties on micromilled AA6082 surfaces is investigated via nanoindentation. The complexity of the now investigated alloy is notably increased in comparison to pure mono- and polycrystalline aluminum. The main differences of these materials as compared to AA6082 are:

- AA6082 (AlSi1MgMn) is composed of several chemical elements. In addition to the nominal chemical composition, contaminants are also present (Table A.3). These alloying elements significantly influence the microstructure and the mechanical behavior.
- In contrast to Al5N-Poly, AA6082 is precipitation hardened with a profound influence on mechanical properties (i.e. hardness and yield strength) and on the microstructure.
- The thermo-mechanical treatment of the AA6082 plate material leads to a certain texture in the rolling direction. This also affects the microstructure considerably.
- The applied micromilling process affects the microstructure as well as mechanical properties of the surface due to strain hardening.

The impact of process parameters on mechanical properties of micromilled AA6082 surfaces has been investigated. Particular attention was paid on the influence of tool sharpness and roughness as well as the uncut chip thickness, on strain-hardening and roughness of the so produced surfaces. Surface strain-hardening (analogous to the deformation zone) due to micromilling is governed by the micromilling ploughing effect (section 4.3). It is mainly influenced by the tool sharpness (cutting edge radius) and the thickness of the material removed per tool revolution (uncut chip thickness). The effect of uncut chip thickness is related to the cutting edge radius. The ploughing effect becomes stronger, when the uncut chip thickness is close to the cutting edge radius.

To research the effect of the tool sharpness, AA6082 surfaces were peripherally micromilled either with the solid carbide tool (SC-tool) or the mono crystalline diamond tool (MD-tool) and compared to an electropolished reference surface. To investigate the influence of the uncut chip thickness, the cutting parameter single tooth feed f_z of $3\ \mu\text{m}$, $8\ \mu\text{m}$ and $14\ \mu\text{m}$ was used. Multi-step indentation was applied as it is an appropriate and available technique to extract depth-dependent mechanical properties. To approximate the depth of the strain-hardened zone, two data analysis models (Korsunsky model, equation (5.10) according to [53], exponential model, equation (5.11)) were fitted to the experimental data.

In addition to the mechanical properties, the morphology of the produced surfaces has been analyzed. Similar to the mechanical properties, surface quality is expected to be mainly influenced by the tool sharpness (i.e. cutting edge roughness) and to a lesser extent by the uncut chip thickness. In this context, tool geometry was determined microscopically. Confocal light microscopy was used to determine the overall morphology and roughness of the micromilled surfaces, because of the large field of view and the ability to extract height data of the surface.

9.2 Results

9.2.1 Tool geometry

The SEM images of the cutting edge in Figure 9.1 (investigated as described in section 5.2.3) show flank and rake face (see Figure 5.3) of both tools for comparison. The cutting edge of the SC-tool in Figure 9.1 (a) demonstrates grinding traces both on the rake and the flank face. Additionally, embedded tungsten carbide particles can be distinguished in the cutting edge. By contrast, the MD-tool in 9.1 (b) appears very smooth and almost featureless. The visible contamination is not decisive for the quality of the milling process, since the contaminants are usually mechanically weak.

The wedge angles (Figure 5.3) of both tools were determined from optical microscopy images. While the SC-tool has an acute wedge angle of approx. 54° , the wedge angle of the MD-tool is almost a right angle, i.e. approx. 83° . SEM images of both tools revealed significant differences in tool sharpness. It was necessary to use more the ten times the magnification used for the SC-tool (Figure 9.2 (a)) to determine the radius of the MD-tool

(Figure 9.2 (b)). Cutting edge radii approximated from the these SEM images are 671 nm for the SC-tool and 17 nm for the MD-tool, a difference of almost factor 40.

The SC-tool has an appreciable roughness (Figure 9.3 (a)), whereas it is difficult to recognize any features along the cutting edge of the MD-tool (Figure 9.3b). Subsequently, R_q and R_t were determined based on these images. The resulting roughness values are shown in Table 9.1. It is remarkable, that the cutting edge roughness R_q of both tools differ by more than a factor of 25. In fact, the cutting edge of the MD-tool is so smooth, that the resulting R_q and R_t values probably correspond the measurement error instead of the actual roughness. Thus, the most important tools parameters, cutting edge radius and roughness are extremely different for both used tools. Other measured geometric parameters of the tools (i.e. wedge angle, rake face and flank morphology) are less relevant for the interpretation of the results.

Table 9.1: Average values of the cutting edge roughness R_q and R_t for the SC- and MD-tool with the standard deviation σ .

Tool	$R_q \pm \sigma$ (nm)	$R_t \pm \sigma$ (nm)
SC-tool	2355 ± 1551	8881 ± 5208
MD-tool	90 ± 48	661 ± 363

9.2.2 Roughness of the machined surfaces

The micromilled structure is shown in Figure 9.4. The measurements are performed in the middle of the horizontal surface. As discussed in the following, roughness and radius of the milling tools have significant influence on the quality of the produced surfaces. The MD-milled surfaces are generally very smooth and show only few defects in comparison to the SC-milled surfaces (Figures 9.5 to 9.7). Due to its smaller cutting edge radius, high hardness, high stiffness and low friction coefficient, the MD-tool is even able to cut through intermetallic phases. In case of the SC-tool these compounds are dragged through the surface, whereby scratches and surface defects are produced.

Confocal microscopy images of the produced surfaces are depicted in Figures 9.5 to 9.7. The blue arrow next to the scale bar represents f_z and also indicates the milling direction. Based on these images, surface features can be categorized with respect to the orientation of milling direction. Height variations parallel and perpendicular to the milling direction are described as “vertical roughness” and “horizontal roughness”, respectively. The one-dimensional roughness parameters R_q and R_t are measured both in “vertical” and “horizontal” directions. Vertical roughness is mainly determined by f_z , which should be visible in the form of lines perpendicular to the milling direction. Horizontal roughness is mainly governed by the roughness of the cutting edge. Additionally, there are non-directional features, namely the intermetallic phases and other inclusions in the base material.

In all images vertical grooves are observable and indicate the milling direction. Deep vertical grooves are evident on the SC-tool machined surfaces (Figures 9.5 and 9.7 (a)).

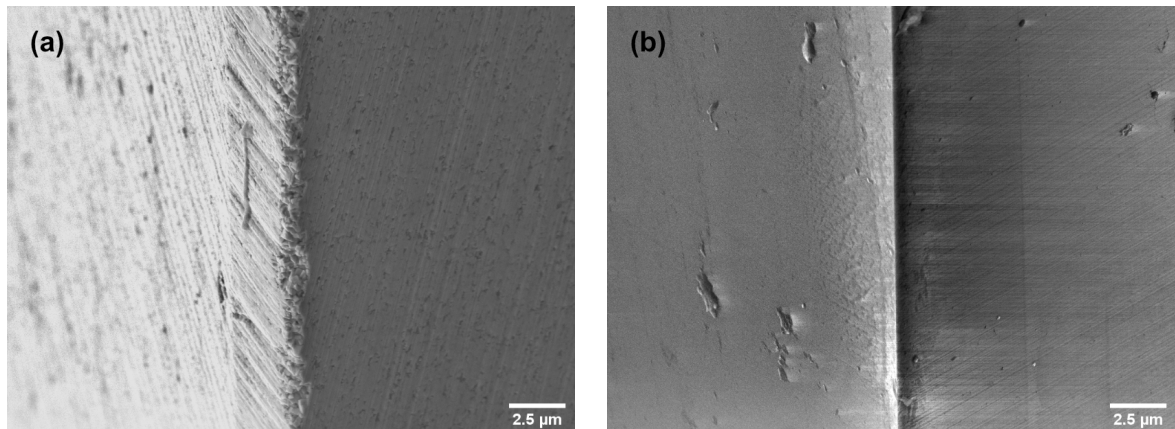


Figure 9.1: SEM-images on the flank (left hand side) and rake face (right hand side) of the utilized tools. (a) SC-tool, (b) MD-tool.

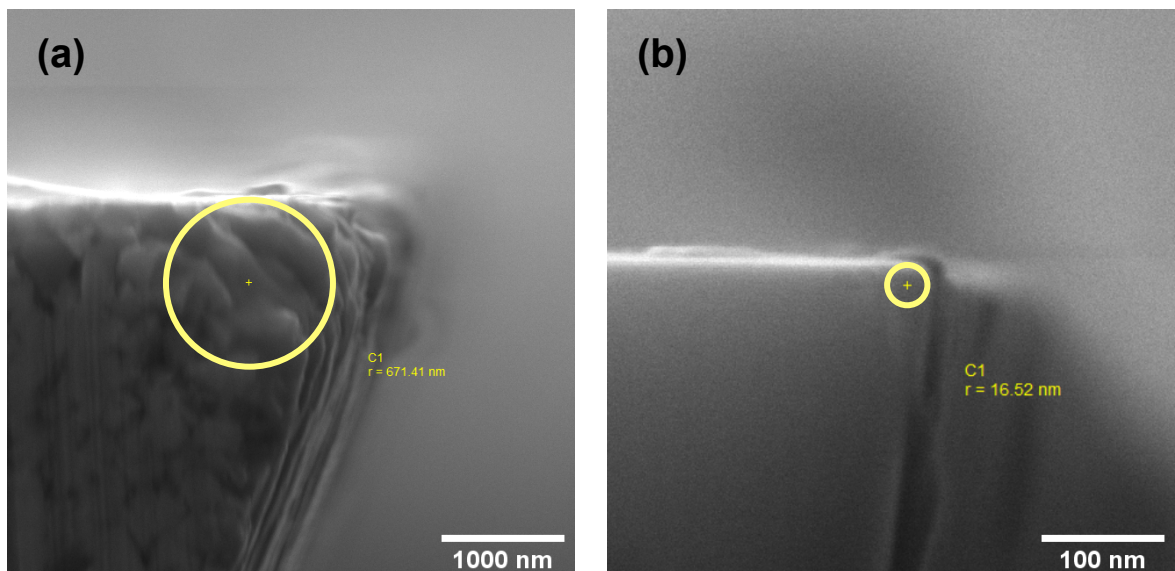


Figure 9.2: SEM-images of the cutting edge radius, acquired parallel to the tool axis. The yellow circles indicate the measured tool radius. (a) SC-tool, $r = 671$ nm. (b) MD-tool, $r = 17$ nm. The image (b) (MD-tool) has a ten times higher magnification (note the scale bar).

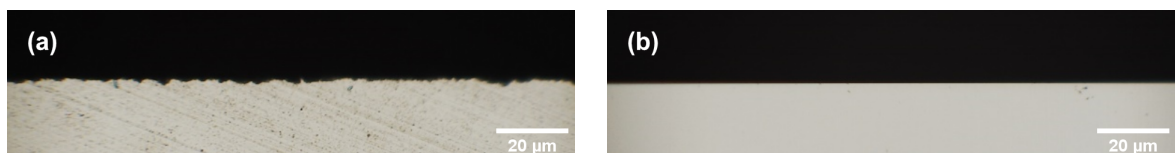


Figure 9.3: Optical microscopy images of the cutting edges for the evaluation of the cutting edge roughness. The images are taken from the direction of the rake face. (a) SC-tool, (b) MD-tool.

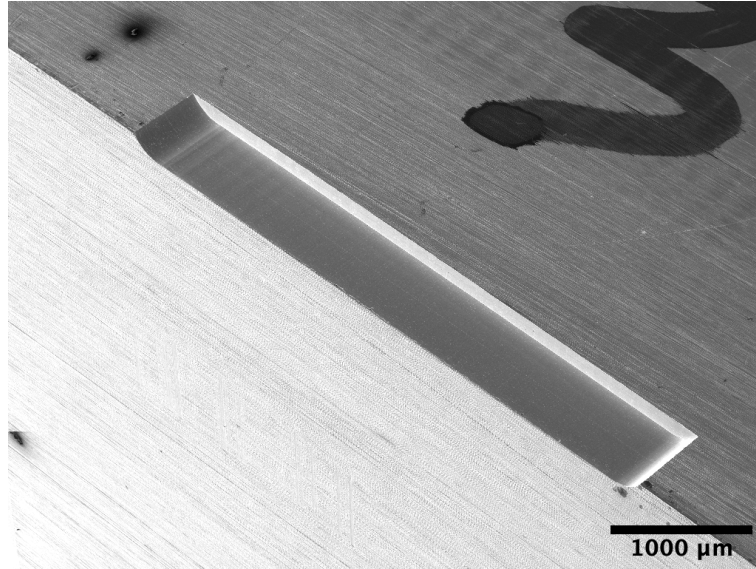


Figure 9.4: Example of micromachined structures. The roughness and indentation measurements have been performed on the horizontal surface.

At the same time, only a few significantly flatter grooves can be observed on the MD-tool machined surfaces (Figures 9.5 and 9.7 (b)). This difference is also reflected in the horizontal roughness (Figure 9.9). Here, the resulting R_q and R_t -values of the surfaces machined with the MD-tool are almost five times lower than those for the SC-tool. For all surfaces produced with the same tool (SC or MD), no significant dependency of horizontal roughness on f_z could be determined. The f_z -steps can be seen perpendicular to the milling direction on the surfaces produced with the MD-tool (Figures 9.5 and 9.7 (b)), but these are unrecognizable on surfaces produced with the SC-tool (Figures 9.5 and 9.7 (a)).

Vertical roughnesses are summarized in Figure 9.8. Both R_q and R_t are almost equal, regardless of the used tool. Yet, R_t seems to correlate with f_z at least for MD-milled surfaces. The measured vertical roughness values are much lower as compared to the horizontal roughness from Figure 9.9. Thus, only a slight influence of undeformed chip thickness on vertical roughness and no effect on horizontal roughness could be observed.

9.2.3 Depth dependent hardness of micromilled surfaces

The depth-dependent hardness data acquired from the multi-step-curves are shown in Figure 9.11. Additionally, min. and max. H_{IT} values along with an 8%-onset depth (i.e. depth at which hardness increases by 8% relative to the bulk value at max. indentation depth) are summarized in Table 9.2. $H_{IT,min}$ of all AA6082 samples (milled or electropolished) converge to a value of approx. 1250 MPa at higher indentation depths (Table 9.2). This value also agrees well with the overall average H_{IT} of the electropolished AA6082 reference, and corresponds to the bulk hardness of the AA6082 alloy. The electropolished Al5N sample exhibits the lowest hardness of $H_{IT} \approx 240$ MPa, while this value increases at

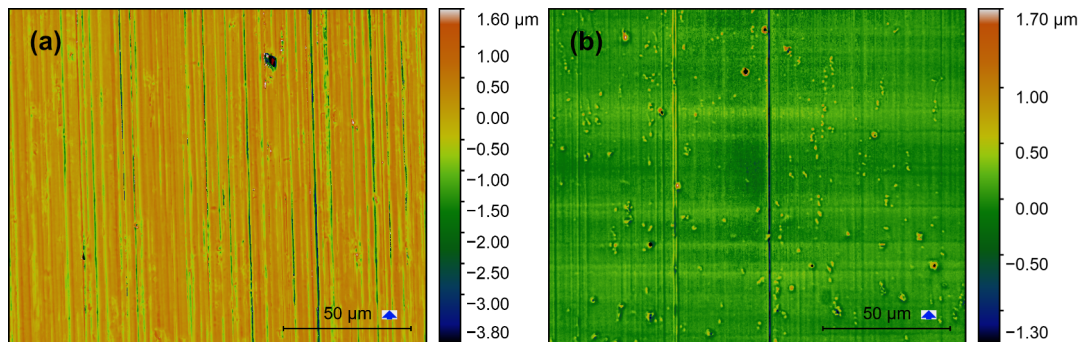


Figure 9.5: Confocal microscopy images of AA6082 surfaces milled with $f_z = 3 \mu\text{m}$: (a) SC-tool, (b) MD-tool.

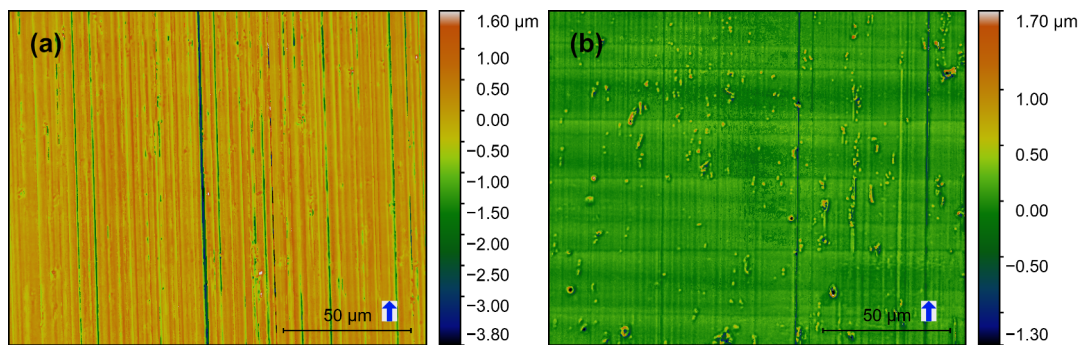


Figure 9.6: Confocal microscopy images of AA6082 surfaces milled with $f_z = 8 \mu\text{m}$: (a) SC-tool, (b) MD-tool.

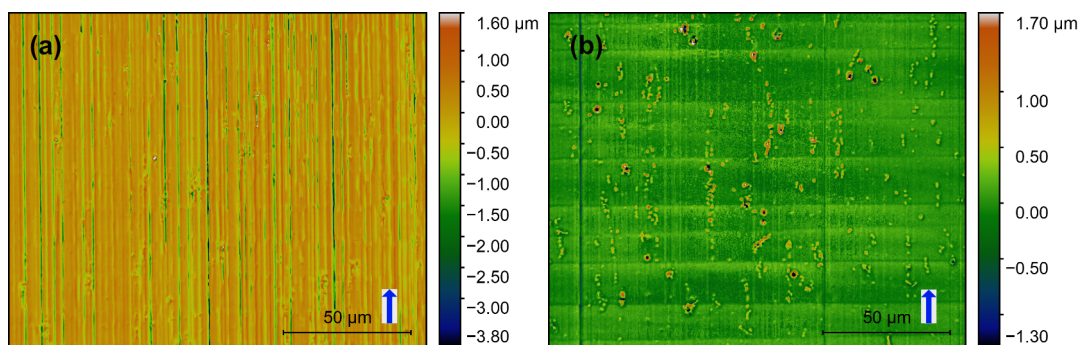


Figure 9.7: Confocal microscopy images of AA6082 surfaces milled with $f_z = 14 \mu\text{m}$: (a) SC-tool, (b) MD-tool.

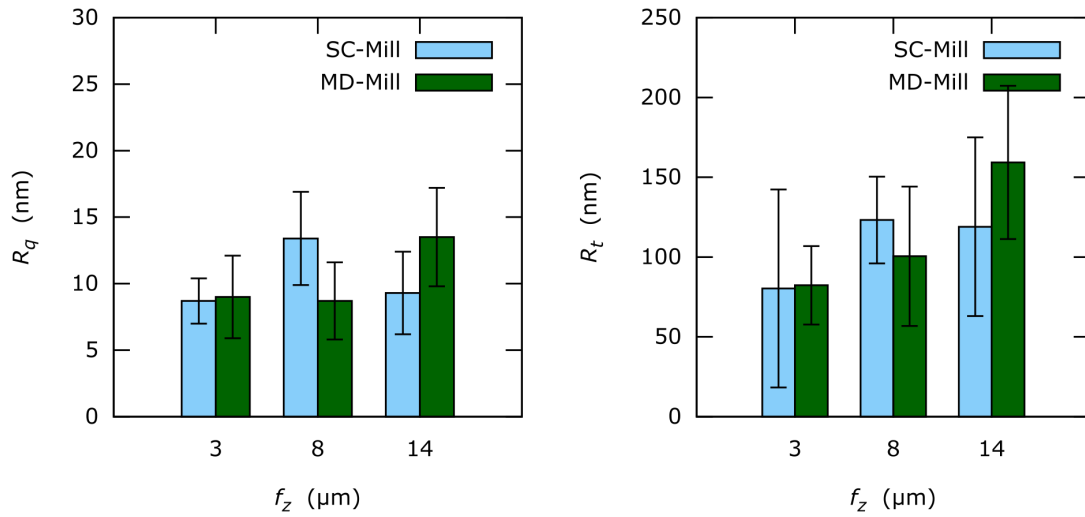


Figure 9.8: Summary of vertical one-dimensional roughness R_q and R_t for the different feeds f_z .

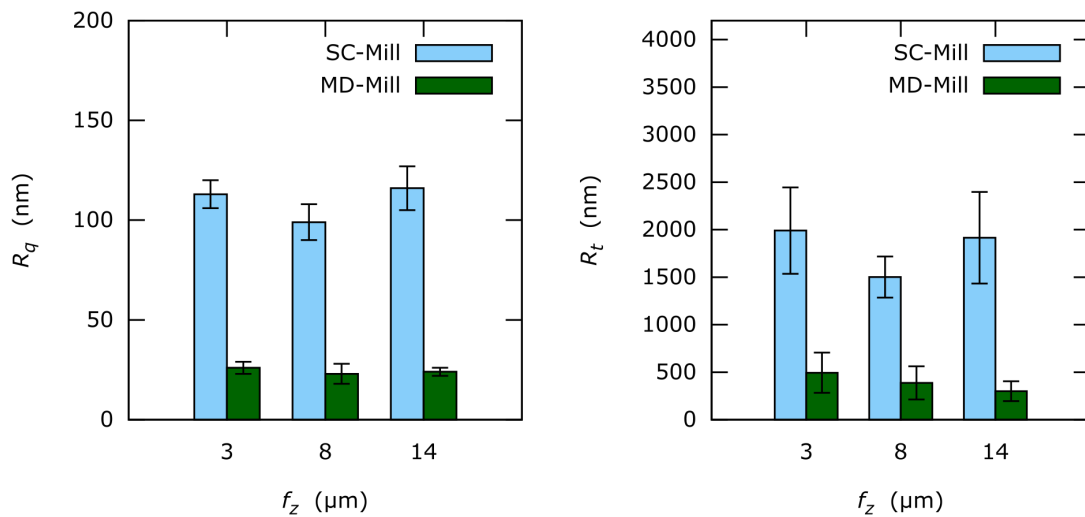


Figure 9.9: Summary of horizontal one-dimensional roughness R_q and R_t for the different feeds f_z .

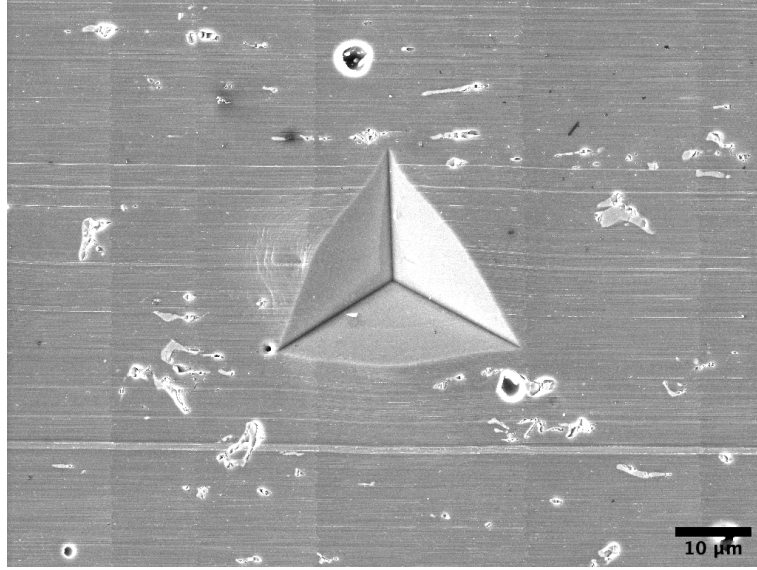


Figure 9.10: Exemplary SEM image of the AA6082 surface milled by the MD-tool and the indentation made according to the ESP-protocoll.

lower indentation depths due to the indentation size effect (ISE). The AA6082 reference has an almost constant $H_{IT} \approx 1195$ MPa for all indentation depths with no indications of the ISE.

As expected, all milled surfaces show strain-hardening in form of increasing H_{IT} at low depths. This effect is particularly prominent on the SC-tool machined surfaces (Figure 9.11a). Here the 8%-onset of hardness is reached at the indentation depth of $2.5 \mu\text{m}$. Maximum H_{IT} of more than 2000 MPa is reached at lowest indentation depths (Table 9.2).

Table 9.2: Summary of the minimum (at max. depth) and maximum (at min. depth) hardness values and the onset depth of strain-hardening for all machined samples. Average 8%-onset values are presented in the table.

Tool	f_z	$H_{IT,min}$ (MPa)	$H_{IT,max}$ (MPa)	8%-onset depth (μm)
SC-tool	3	1261 ± 62	1949 ± 313	2.03
	8	1233 ± 24	2166 ± 430	2.26
	14	1262 ± 77	1858 ± 543	1.62
MD-tool	3	1205 ± 20	1376 ± 79	0.61
	8	1227 ± 37	1505 ± 141	0.81
	14	1249 ± 37	1464 ± 90	0.60
AA6082-ref		1187 ± 35	1197 ± 46	-

Strain hardening is less pronounced for MD-milled surfaces, but still distinguishable in comparison to the AA6082 reference (Figure 9.11). The 8%-onset appears at a lower depth of approx. 500 nm and reaches its maximum H_{IT} of about 1500 MPa. The min. and max.

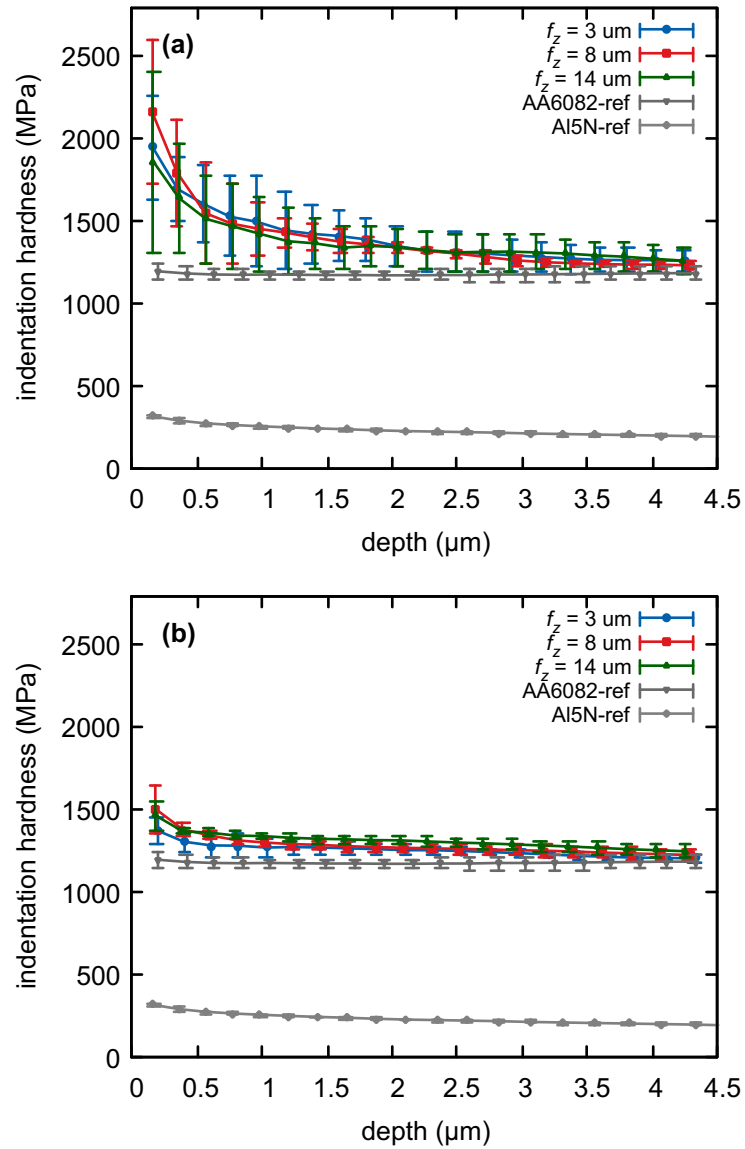


Figure 9.11: Indentation hardness-depth-curves of machined surfaces in comparison to electropolished AA6082 and polycrystalline Al5N surface as a reference. (a) SC-tool and (b) MD-tool machined surface.

values of H_{IT} together with the 8%-onset depth are summarized in Table 9.2. Variations of f_z do not appear to have an impact on the strain-hardening. However, this effect is difficult to assess from the multi-step-curves only.

9.2.4 Film-substrate-model fit

Two different film-substrate models are fitted to the depth-hardness curves shown in Figure 9.11; the respective fit-parameters can be found in Table D.1. The fits of the Korsunsky-Model from Equation (5.10) and the exponential model form equation (5.11) are presented in Figure 9.12. The Korsunsky-model shows a reasonable fit for larger depths above approx. 500 nm. The fitted parameters shown in Table D.1 appear reasonable and the H_s and H_f values are in the expected range (average $H_s = 1215 \text{ MPa} \pm 31 \text{ MPa}$), however, there is a significant deviation between fits and experimental data at indentation depth below 500 nm (blue in Figure 9.12). The total sum of the RSS is 9.0. The exponential fit produced equally good agreement of fits to experimental data for indentation depths above 500 nm. But the exponential fit deviates significantly from the Korsunsky model at indentation depths below 500 nm resulting in a lower H_s of $1195 \text{ MPa} \pm 40 \text{ MPa}$. While the Korsunsky-model (red in Figure 9.12) converges to a certain hardness at low depth, the exponential model results in a progressive hardness increase (no threshold value). This is in better agreement to the experimental data which is reflected in the lower RSS of 5.3 as compared to the Korsunsky-Model.

9.2.5 Evolution of indentation harness of aluminum

Measurements of indentation hardness at approx. $1.2 \mu\text{m}$ with either single or multi-step indentation are comparatively shown in Figure 9.13. The low-defect monocrystalline aluminum (Al5N-SX) exhibits the lowest hardness and σ values. After introducing multiple grains with various orientations (Al5N-Poly (RX)) σ increases significantly, but the mean value remains on the level of the monocrystalline sample. The uni-axially deformed aluminum (Al5N-Poly (def.)) with increased dislocation density (due to strain-hardening) shows a significant increase in hardness and a tenfold increase in σ . This is attributed to the dynamic recovery leading to a heterogeneous microstructure, as discussed in section 8.3. Finally, the largest hardness increase of almost 500 % relative to monocrystalline aluminum and about 300 % relative to pure aluminum deformed by 75 % is observed for electropolished AA6082. This is due to the strengthening methods applied during production of the alloy. Additionally, the data scatter increases by approx. 20 times relative to monocrystalline aluminum due to highly complex microstructural composition.

Machining with the MD-tool results in average hardness and data scatter almost indiscernible from electropolished surfaces. Thus, the MD-tool introduces only a minimal amount of strain hardening and roughness. After milling with the SC-tool, indentation hardness increases further up to the peak value of 600 % relative to monocrystalline sample accompanied by a slight increase of the data scatter. This clearly indicates the ploughing

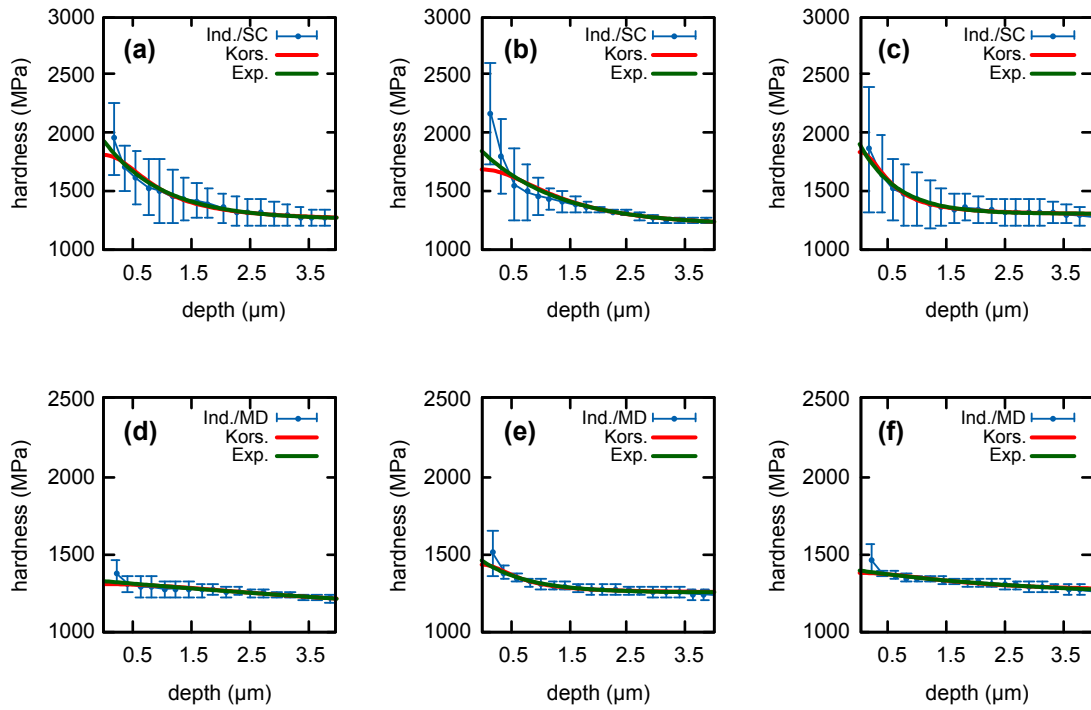


Figure 9.12: Film-substrate-models fitted to experimental multi-step indentation data. Multi-step indentation data (Ind.) of surfaces produced with two different tools (SC/MD) is fitted to the Korsunsky-Model from Equation (5.10) [53] and the exponential model from equation (5.11). (a),(d): $f_z = 3 \mu\text{m}$, (b),(e): $f_z = 8 \mu\text{m}$, (c),(f): $f_z = 14 \mu\text{m}$.

effect leading to significant strain hardening as well as increased surface roughness which results in an increase of the data scatter.

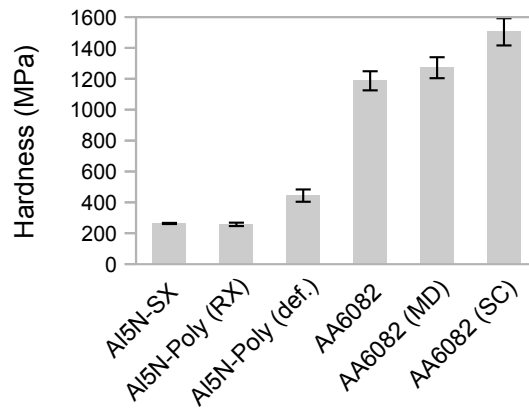


Figure 9.13: Summarized indentation hardness of aluminum with different microstructures and after different treatments and surface preparation procedures. All hardness values were obtained for the indentation depth of approx. $1.2 \mu\text{m}$

9.3 Discussion

Surface roughness

The results summarized in Figures 9.8 and 9.9 demonstrate significant differences for one-dimensional horizontal roughness (perpendicular to the milling direction) of surfaces machined with both mills. Vertical surface features i.e. scratches in the milling direction are generated by the roughness of the cutting edge which is replicated on the machined surface, while the original roughness is smoothed out significantly during milling.

In the case of the SC-tool, the cutting edge geometry is replicated on the sample surface and yields comparably high roughness with random scratches in the milling direction (probably due to tungsten carbide particles). However, the roughness of the machined surfaces is 20 times lower than the roughness measured along the tool's cutting edge. Thus, the roughness of the micromachined surfaces is mainly influenced by the cutting edge geometry and not the processes parameters (i.e. tooth feed f_z).

The MD-tool produces very smooth surfaces with systematic features. The roughness of the MD-tool machined surfaces is difficult to compare to the cutting edge roughness of the MD-tool. The reason is that the cutting edge is so smooth, that its roughness could not be determined neither by light microscopy nor by SEM. Since the MD-tools cutting edge is smooth, the remaining low roughness is mainly caused by two factors: small intermetallic phases (non-directional) and f_z (parallel to the milling direction). Additionally, systematic vertical lines are visible on confocal microscopy images of the MD-milled surfaces. These are generated by the few defects of the MD-tools cutting edge. SEM-images (not shown here) confirm that these features completely run through the milled surface.

Large intermetallic phases produce notably large height differences, exceeding the effect of the mill geometry ($\Delta h > 10 \mu\text{m}$). This constitutes a potential problem for coating of the so produced component. However, this can be only dealt with by changing from AA6082

to a purer material with less intermetallic phases. Other process and tool parameters such as f_z , β and flank morphology have no significant influence on roughness. In case of f_z the chosen parameter range is significantly larger than tool radius. Thus, the ploughing effect does not change with f_z (compare to different cutting modes in figure 4.3 and the below discussion).

Surface strain-hardening

According to Filitz et al. the specific cutting energy increases with decreasing undeformed chip thickness due to the micromilling size effect [26]. In the present context, this means that the size effect should increase when f_z (corresponding to undeformed chip thickness) converges to the minimum uncut chip thickness h_{min} . Kim et al. suggests that h_{min} can be approximated from the tool's radius r by $h_{min} \approx r/3$ [51].

Both mills investigated in this study have different radii and therefore h_{min} depends on the used tool. For the MD-tool, $f_z = 3 \mu\text{m}$ was used, which is already 500 times greater than the corresponding h_{min} . This h_{min} -value is beyond reach ($<10 \text{ nm}$), implying that in case of the MD-tool the milling process remains in a pure cutting regime. This is consistent with the multi-step indentation results, where only a minimal hardness increase at depths below 500 nm can be observed. This hardness increase can be attributed to surface strain-hardening and not to the ISE by comparison to the electropolished AA6082 reference. Here, no significant ISE i.e., no hardness increase at low depths is observable. This is different for the SC-tool. Estimated from the cutting edge radius, the used $f_z = 3 \mu\text{m}$ here is only 15 times h_{min} . Therefore, the undeformed chip thickness is much closer to h_{min} and a significant ploughing effect can be anticipated. This is verified by the experimental results, which demonstrate significant strain-hardening (hardness increase) at depths below 1 μm .

The Korsunsky film-substrate model assumes that hardness at low indentation depth is dominated by the film. Therefore, a plateau at low depths is expected, as it is also demonstrated by Tuck [92, 93]. Yet, this behavior cannot be observed in the present data set (Figure 9.11). Apparently, the hardness increases with decreasing indentation depth, while the maximum (which would be indicated by a plateau) could not be detected.

As mentioned above, indentation hardness is averaged from the plastic zone beneath the indenter [20]. According to the Bückle-Rule, this zone extends into the indentation direction for at least 10 times the indentation depth [11]. This leads to three options for interpreting the experimental data, that in any case lead to a progressive hardness increase at low depths. Figure 9.14 illustrates three principal possibilities of strain-hardening at the surface:

- Uniformly hard surface film on top of softer bulk material (Figure 9.14 (a)). This model corresponds to the Korsunsky film-substrate model [53]
- Gradually hardened surface (Figure 9.14 (b)). This model assumes maximum hardness at the surface with a continuous decrease towards bulk. It is represented by the exponential model.

- Combination of the above two models consisting of a very thin, uniformly hard film and gradually hardened bulk underneath (Figure 9.14 (c)).

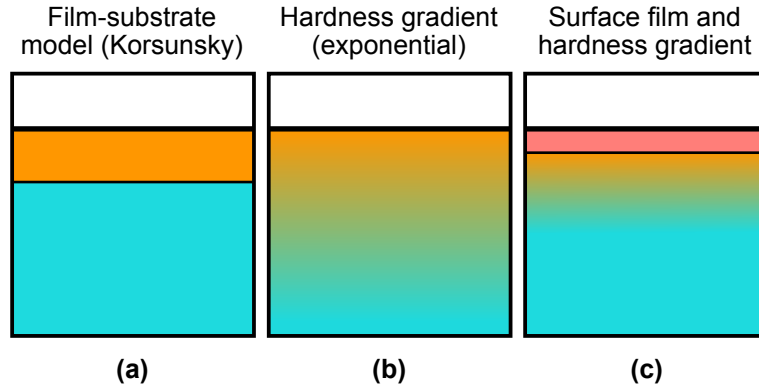


Figure 9.14: Different models for the interpretation of the indentation results. (a) Uniformly hard film on softer substrate. (b) Gradually hardened surface. (c) Combination of a hard thin surface film and gradually hardened bulk.

The stress in the material underneath the tool was analyzed for micromilling by Lai et al. [55]. Using FEM simulations they demonstrated that the stress decreases progressively with depth. Since the stress applied to the material correlates with strain-hardening, the uniformly hard surface layer modeled by Korsunsky (Figure 9.14 (a)) can be discarded.

The model of the gradually hardened surface (Figure 9.14 (b)) corresponds well with the stress-analysis by Lai et al., and also results in a better fit than the Korsunsky model ($RSS_{sum,korsunsky} > RSS_{sum,exponential}$). However, it is neglecting the potential influence of the hard native surface oxide layer. This surface layer could be implemented in the combined model (Figure 9.14 (c)) but no mathematical expression of this model suitable for our purpose was available in the literature by the time of writing. According to Evertson et al. the thickness of such layers is usually below 10 nm [22]. The influence of such a thin layer is assumed to be insufficient to significantly affect effective hardness. For this reason the model (c) can be practically reduced to quality of model (b).

The exponential model resulted in fits of sufficient quality. Based on these fits and stress data from the literature, it can be concluded that the surfaces generated by micromilling are gradually strain-hardened. From the 8%-onset of the hardness increase and the Bückle-Rule it can also be approximated, that the hardened layer is very thin. To estimate the thickness of the strain-hardened layer, the average height of the 8%-onset is divided by 10 according to the Bückle-Rule. This results in the affected thickness of less than 200 nm for surfaces machined with the SC-tool and less than 70 nm with the MD-tool.

The variation of f_z seems to have no effect of strain-hardening (no significant differences between experimental hardness-depth-curves with different f_z and same tool). It should be noted, that the H_{IT} -error is particularly high for low depths. The reason is that surface roughness affects the results at lower depth. The ISO 14577-1 proposes $h \geq 20 \cdot R_a$ for the minimum indentation depth and roughness of the analyzed surface. Accordingly,

the minimum indentation depth amounts to 340 nm for the MD-tool and to 1380 nm for the SC-tool. Hardness values obtained for depths below these values are beyond the recommendation of the normative, hence they have to be interpreted cautiously. Therefore, a different approach is required to determine the hardness values, especially of the SC-tool machined surfaces at very low depth.

9.3.1 Indentation hardness evolution of aluminum

As presented in Figure 9.13, the indentation hardness of aluminum undergoes several changes. The effects of crystal orientation and strain hardening in pure aluminum turn out to be rather subtle in comparison to the impact of the strengthening techniques applied during manufacturing of the AA6082 alloy. The combined effect of strain-hardening and precipitation strengthening results in a hardness increase of up to five times the indentation hardness of monocrystalline aluminum. This value is virtually unchanged after micromilling with the MD-tool, i.e. almost no strain hardening of the surface occurs due to the tool's high sharpness. By contrast, the SC-tool which introduces more strain-hardening to the surface, resulting in a greatly enhanced hardness value.

9.4 Conclusions

Amongst investigated parameters, the cutting edge roughness turned out to have the largest impact on the roughness of micromilled surfaces. This is demonstrated by the serrations along the SC-tool cutting edge which directly are reproduced on the micromilled surface. Conversely, the sharper MD-tool with smooth cutting edge produces very smooth surfaces. The still present surface features are attributed to intermetallic phases and defects of the cutting edge. We did not observe a correlation of the uncut chip thickness to the roughness. Additionally, we observed that the MD-tool is able to cut through the intermetallic phases, with a great impact on surface quality. This is especially relevant for micromilling of miniature parts with tolerances in the sub-micrometer range. All these findings are important for micromilling of roughness-critical components whose roughness is important for its function, e.g. radio frequency components for terahertz applications.

The indentation hardness of AA8062 is higher than that of Al5N due to the strengthening mechanisms at play. In addition to bulk hardness, the surface is considerably strain-hardened by the ploughing effect with an increase of max. hardness by ca. 100 %. Tool sharpness is the main influencing factor for the surface ploughing effect is tool sharpness. The affected surface layer produced with a sharper MD-tool is five times thinner and ca. 30% harder as estimated by the Bückle's 1/10-rule. We did not observe an influence of the uncut chip thickness due to the chosen parameter range and large error at indentation depths below 500 nm.

The Korsunsky model of a uniformly hard film (i.e., strain-hardened layer) is acceptable for determining hardness at indentation depths > 500 nm. Below that limit, the exponential model of a gradually hardened film provided a better fit. This suggests that the surface

is modified by micromilling resulting in a hardness gradient. Apparently, the MD-tool can produce very smooth surfaces, even preserving the intermetallic phases by just cutting through them. Also the strain-hardening introduced by the MD-tool is negligible in comparison to the electropolished surface. In summary, a sharp tool with low friction coefficient and high stiffness is invaluable for micro-manufacturing applications, where low roughness, high dimensional accuracy and repeatability of the micromilling process is required.

Chapter 10

Summary and Outlook

Micromilling features an excellent prospect for producing complex miniature metal components. To meet the high industrial standards in terms of repeatability, tolerances and surface quality the milling process and the behavior of the material at small scales subject to micromilling must be understood in detail. With this objective in mind the evolution of microstructure and mechanical properties of aluminum on the micro- and nanometer scale has been explored in this thesis. The focus was especially on the impact of plastic deformation of aluminum on mechanical properties.

Commercial aluminum alloys are considered quasi-homogeneous on the macro-scale, however, their microstructure is very complex. It consists of features with different characteristic length-scales from few nanometers (i.e. Guinier-Preston zones) to several micrometers (i.e. intermetallic phases). Thus, the macro-mechanical response is a combination of the contributions of these microstructural features. To understand the composite mechanical properties of AA6082 and furthermore the effect of micromilling on surface properties, the single microstructural features have been investigated mechanically on the nanoscale. The material complexity was increased systematically, whereby the respective findings could be transferred from single crystals to plastically deformed polycrystalline aluminum and further to micromilled engineering alloy AA6082. Nanoindentation was the main tool to determine hardness and elastic modulus of aluminum surfaces on different length scales.

Beginning with the most fundamental material with only few sources for variation of mechanical properties, the effect of crystal orientation and indenter orientation on indentation hardness and modulus were investigated on high-purity monocrystalline aluminum. Both, the effect of crystal orientation ((111), (110) and (100) normal to load direction) and azimuthal indenter orientation are in the range of 1-2 %. This corresponds well with theoretical considerations and calculations. With these results, the literature gap on systematic, theoretically backed up experimental anisotropy analysis for aluminum by nanoindentation is closed. Although measurable, these variations are deemed technologically non-relevant. Nevertheless, nanoindentation is a powerful tool to reliably measure variations in hardness and modulus in the range of just a few percent. This capability was further exploited for investigations on plasticity of polycrystalline aluminum.

During micromilling, the machined surface undergoes strain-hardening. To investigate the effect of crystal anisotropy on strain-hardening, high-purity aluminum was deformed uniaxially. The complex plastic flow and the evolution of polycrystalline grain structure were investigated by metallography, nanoindentation and theoretical considerations. Unexpectedly, intermittent grain softening was observed with increasing strain. This process was characterized mechanically at the single-grain level by nanoindentation. Upon reaching of 75 % deformation the initial strain hardening was annihilated, reverting the hardness of most single grains to the level of a low-defect single crystal. Grain softening is ascribed to the discontinuous dynamic recovery. Thus, the highest achievable strength of polycrystalline aluminum is not limited by embrittlement due to strain hardening, but rather by the softening effect. In summary, it could be demonstrated that high-purity polycrystalline aluminum demonstrates a unique behavior when subjected to uniaxial compression.

In the light of these findings, the engineering alloy AA6082 was micromilled with two different cutters: the extremely sharp (radius of 17 nm) monocrystalline diamond and a relatively blunt (radius of 671 nm) solid carbide tool. The so obtained surfaces were investigated by light and electron microscopy as well as by nanoindentation. The tool's sharpness and smoothness/roughness of the cutting edge are shown to have the most impact on surface morphology. A significantly better surface quality was achieved with the monocrystalline diamond tool, which generated surfaces with an average roughness well below 100 nm and preserved brittle intermetallic phases by cutting through them. The surface strain-hardening was also significantly affected by the tools geometry. The solid carbide tool caused strain-hardening of the surface, resulting in an increase of indentation hardness of approximately 27 % (measured at 1.2 μm depth). The monocrystalline diamond tool, however, left the surface almost unaffected, thus leading to a hardness increase of just 7 %. Additionally, depth-dependent hardness profiles could be extracted from nanoindentation. Deconvolution of these data by modeling the surface layer yielded new insights into surface strain-hardening by micromilling. Especially, micromilling produced a strain-hardened surface layer with its hardness decreasing gradually towards the bulk. The above findings on the evolution of mechanical properties of aluminum subjected to complex mechanical load have the potential to improve industrial micromilling processes performed on commercially available materials. In particular, the performance of sharp and smooth monocrystalline diamond tools is trend-setting for micromanufacturing of miniature parts with high precision and repeatability.

Although the first characterization step of such surfaces is done, there is still much undiscovered. To verify the driving force behind the dynamic recovery of pure aluminum we suggest repeating the compression experiments with aluminum samples of different purity grades (up to commercially pure 99.5 % Al). This should enforce gradual homogenization of crystal anisotropy by lattice distortion through impurities and provide additional sources for dislocation nucleation. The experiments can be supported with electron backscatter diffraction maps to obtain additional insights into preferred grain orientation and microstructure evolution. The milling experiments should be performed in the critical mode where the largest ploughing effect is anticipated. According to Kim this is expected for the uncut chip thickness of about one-third of the cutting edge radius [51].

Depth-dependent strain-hardening as measured by indentation could not be interpreted satisfactorily with available film-substrate models, hence an improved data analysis model is necessary. Here, we suppose to implement the approach presented by Göken et al. [37] where the Sneddon-equation can be employed to determine hardness H independently from the contact area. The main drawback of this method, i.e. that the Young's modulus of the examined material must be known, can be overcome by a combination with the McElhaney method [66]. Hence, the missing part of the Sneddon-equation can be compensated by optical measurement of the contact area on the material under investigation.

In summary, nanoindentation has the potential not only to determine mechanical properties of single microstructural constituents, but also to provide critical insights into the impact of micromilling process parameters on local plastic deformation and even to quantify the activated strengthening mechanisms.

Appendix A

Employed materials and their chemical composition

Table A.1: Contamination analysis of Al5N-Poly (plate) (from the data-sheet provided by the supplier, HMW Hauner GmbH & Co. KG, Röttenbach, Germany, obtained by optical emission spectroscopy)

Element	Ca	Fe	Mn	Si	Cr	Mg	Na	Ti	Zr
wt. ppm	< 0.02	0.83	0.056	1.51	0.049	0.73	< 0.005	0.067	0.013

Table A.2: Contamination analysis of Al5N-Poly (rod) (from the data-sheet provided by the supplier, Goodfellow GmbH, Hamburg, Germany)

Element	Fe	K	C	Cu	Mg	Hg	Pd	P	Pt	S	Si	Th	U
wt. ppm	0.38	<0.1	<2	<0.2	0.39	<0.1	<0.1	0.27	<0.1	<0.1	0.87	<0.1	<0.1

Table A.3: Chemical composition of AA6082 (from the data-sheet provided by the supplier, ALRO S. A, Slatina, Romania)

Element	Si	Fe	Cu	Mn	Mg	Cr	Ni	Zn	Ti	Ga	V
Content (wt.%)	1.05	0.47	0.09	0.66	0.97	0.17	0.016	0.076	0.026	0.011	0.017

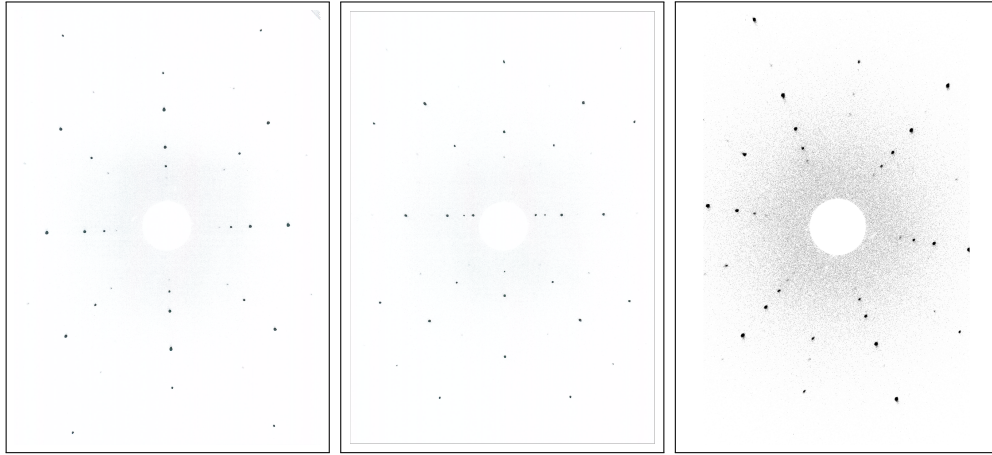


Figure A.1: Laue diffractograms acquired along $[100]$ (left) $[110]$ (center) and $[111]$ (right) directions of the aluminum single crystals. The crystal integrity is verified by the observed sharp reflexes. The crystallographic orientations are confirmed by the respective symmetries.

Appendix B

Devices and chemicals

Table B.1: List of used devices

Device	Description	Manufacturer
Dap-7	Polisher with rotating specimen mover “Pandemin-S”	Struers ApS, Ballerup, Denmark
Electromet III	Electrolytic polisher / etcher	Buehler Inc., Lake Bluff, USA
Hirox RH2000	Optical incident light microscope	Hirox Co. Ltd., Tokyo, Japan
JPK Nanowizzard	AFM equipped with Bruker MLCT tip (20 nm tip radius)	JPK Instruments, Berlin, Germany
KERN Pyramid Nano	CNC machining center at Rohde & Schwarz, Teisnach plant, Germany	Kern Mikrotechnik GmbH, Eschenlohe, Germany
Leitz Ergoplan	Confocal microscope	Leica Microsystems GmbH, Wetzlar, Germany
Picodentor HM500	Nanoindenter equipped with either a Vickers or a Berkovich tip	Helmut-Fischer GmbH, Sindelfingen, Germany
Tescan LYRA3	Scanning electron microscope with fo- cused ion beam for in-situ cross-sections and EDX analysis	Tescan Orsay Holding, a.s., Brno - Ko- houtovice, Czech Republic
Zwick Retro Line	Universal testing machine (used for compression experiments)	ZwickRoell GmbH & Co. KG, Ulm, Germany

Table B.2: Chemical agents and materials used for polishing

Material	Description	Provider
Grinding paper	Silicon carbide grinding paper for wet grinding materials (Grit 600 - 2500)	Struers ApS, Ballerup, Denmark
CT Dia Twin Poly	Water based polycrystalline diamond suspension (grain size: 6 μm , 3 μm , 1 μm)	Cloeren Technology Inc., Wegberg, Germany
OP-S	Standard colloidal silica suspension (Grain size 0.04 μm)	Struers ApS, Ballerup, Denmark
CT A2	Electrolyte for electropolishing	Cloeren Technology Inc., Wegberg, Germany

*Figure B.1: “Electromet III” with customized sample holder used for electropolishing of aluminum microsections.*

Appendix C

Residual analysis of the fitted sine function

The residuals e are calculated as the difference of the measured value y and the modelled value y' :

$$e = y - y' \tag{C.1}$$

The respective residuals shown in Figure C.1 are calculated from the difference of the measured H_{IT} and M data (normalized to their respective mean values) and the fitted sine function both shown in Figures 7.8 and 7.9.

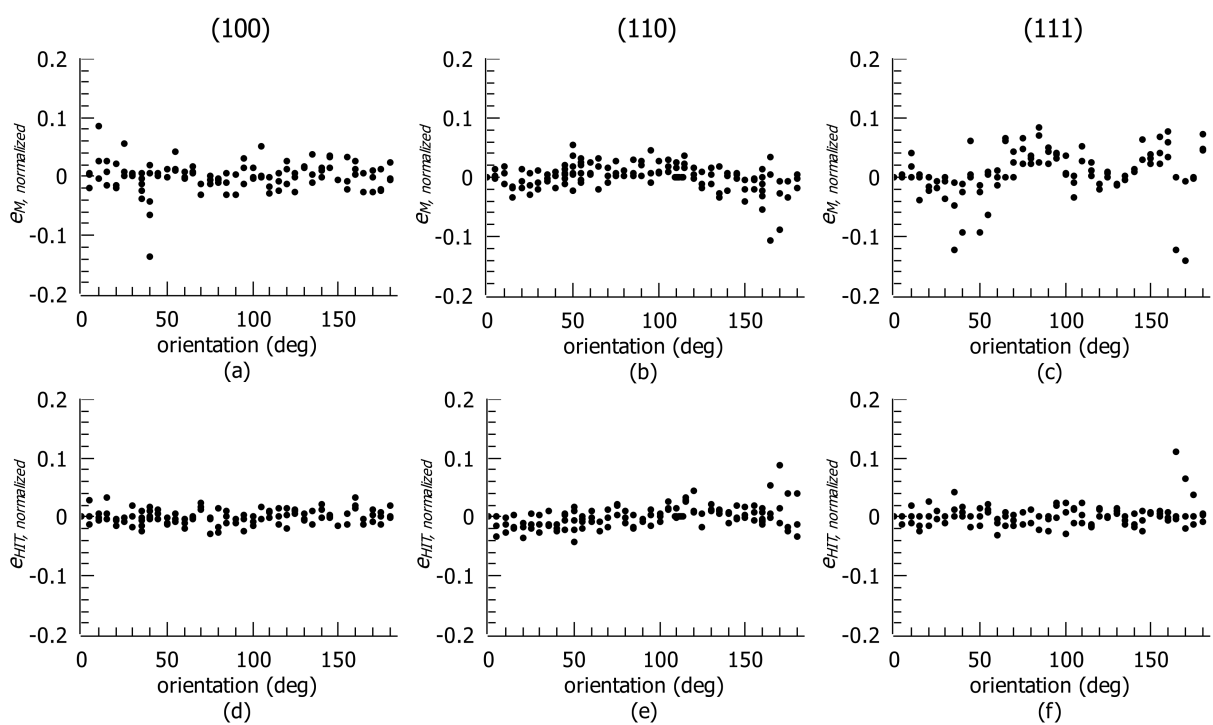


Figure C.1: Residual analysis of the fit to the azimuthal indenter orientation data. $e_M, \text{ normalized}$ (a)-(c). $e_{HTT}, \text{ normalized}$: (d)-(f).

Appendix D

Depth-dependent hardness models: Summary of the fit parameters

The resulting values of numerical fits to depth-dependent hardness data (from multi-step indentation) of AA8082 surfaces peripherally micromilled with the MD-tool and the SC-tool are summarized in table D.1. Two models were fitted to the experimental data as follows:

1. The Korsunsky model from equation (5.10):

$$H_{eff}(h) = H_s + (H_f - H_s) \left(1 + \alpha^{-1} h^2 t^{-1}\right)^{-1}$$

2. The exponential model from equation (5.11):

$$H_{eff}(h) = H_s + (H_f - H_s) \exp(-h/m)$$

Plots of the original data are shown in Figure 9.12. Each fit parameter is accompanied by the respective asymptotic standard error. For each data set the final sum of squares *RSS* is shown additionally.

Table D.1: Fitted parameters of the Korsunsky and the exponential fitted to the depth-hardness data from Figure 9.11.

Tool	f_z (μm)	H_s (MPa)	$H_{s,err}$ (MPa)	H_f (MPa)	$H_{f,err}$ (MPa)	t	t_{err}	α	α_{err}	RSS
Korsunsky model										
SC	3	1236.0	13.3	1803.2	54.1	0.2	82.5	0.2	90.9	0.54
	8	1184.3	16.8	1707.5	114.4	0.3	141.4	0.2	82.7	2.70
	14	1275.0	8.8	1764.2	100.4	0.7	393.7	1.5	845.8	0.37
MD	3	1141.8	102.2	1303.7	10.6	1.3	1552.1	0.1	131.7	1.24
	8	1239.4	7.4	1406.0	36.9	0.5	348.7	0.7	487.7	1.79
	14	1235.7	39.0	1371.6	6.1	2.4	1922.8	0.5	406.2	2.34
Exponential model										
SC	3	1242	4	1835	19	1.2	0.1	-	-	0.1
	8	1199	9	1779	58	1.4	0.1	-	-	1.0
	14	1275	8	1700	57	1.0	0.1	-	-	0.3
MD	3	1039	150	1325	10	7.8	5.7	-	-	0.9
	8	1239	6	1431	19	1.0	0.2	-	-	1.5
	14	1173	60	1387	5.5	4.6	2.0	-	-	1.5

Bibliography

- [1] A. Aramcharoen and P. T. Mativenga. Size Effect and Tool Geometry in Micromilling of Tool Steel. *Precis. Eng.*, 33(4):402–407, 2009.
- [2] R. W. Armstrong. Hall-Petch Relationship: Use in Characterizing Properties of Aluminum and Aluminum Alloys. In G. E. Totten, M. Tiryakioğlu, and O. Kessler, editors, *Encycl. Alum. Its Alloy*. CRC Press, 2018.
- [3] A. Augustyn, P. Bauer, B. Duignan, A. Eldridge, E. Gregersen, A. McKenna, M. Petruzzello, M. Rafferty, J. P. Ray, K. Rogers, A. Tikkanen, J. Wallenfeldt, A. Zeidan, and A. Zelazko. Mohs Hardness. In T. E. o. E. Brittanica, editor, *Encycl. Br. Encyclopaedia Britannica*, Inc., 2017.
- [4] J. C. Aurich, M. Bohley, I. G. Reichenbach, and B. Kirsch. Surface Quality in Micro Milling: Influences of Spindle and Cutting Parameters. *CIRP Ann. - Manuf. Technol.*, 66(1):101–104, 2017.
- [5] H.-J. Bargel and G. Schulze, editors. *Werkstoffkunde*. Springer-Lehrbuch. Springer Berlin Heidelberg, Berlin, Heidelberg, 2018.
- [6] B. Bay and N. Hansen. Recrystallization in Commercially Pure Aluminum. *Metall. Trans. A, Phys. Metall. Mater. Sci.*, 15 A(2):287–297, 1984.
- [7] S. P. Belyayev, V. A. Likhachev, M. M. Myshlyayev, and O. N. Sen’kov. Dynamic Recrystallization of Aluminium. *Phys. Met. Metallogr.*, 52(3):143–152, 1981.
- [8] D. Biermann and E. E. Özkaya. Gratcharakterisierung und -simulation. *VDI-Z Integr. Produktion*, 154(9):70–73, 2012.
- [9] L. Böhme, A. Keksel, F. Ströer, M. Bohley, S. Kieren-Ehse, B. Kirsch, J. C. Aurich, J. Seewig, and E. Kersch. Micro Hardness Determination on a Rough Surface by Using Combined Indentation and Topography Measurements. *Surf. Topogr. Metrol. Prop.*, 7(4):045021, 2019.
- [10] E. Broitman. Indentation Hardness Measurements at Macro-, Micro-, and Nanoscale: A Critical Overview. *Tribol. Lett.*, 65(1):1–18, 2017.

- [11] H. Buckle. Progress in Micro-Indentation Hardness Testing. *Metall. Rev.*, 4(13):49–100, 1959.
- [12] H. Bückle. Use of the Hardness Test To Determine Other Material Properties. In C. H. Westbrook, J. H., editor, *Sci. Hardness Test. Its Res. Appl.*, pages 453–494. American Society for Metals, Metals Park, Ohio, 1971.
- [13] Y. S. Choi, K. I. Kim, K. H. Oh, H. N. Han, S. H. Kang, J. Jang, and J. H. Han. Dynamic Recrystallization in High-Purity Aluminum Single Crystal Under Frictionless Deformation Mode at Room Temperature. *J. Mater. Res.*, 28(20):2829–2834, 2013.
- [14] D. H. Chung and W. R. Buessem. The Voigt-Reuss-Hill Approximation and Elastic Moduli of Polycrystalline MgO, CaF₂, β -ZnS, ZnSe, and CdTe. *J. Appl. Phys.*, 38(6):2535–2540, 1967.
- [15] A. Delafargue and F. J. Ulm. Explicit Approximations of the Indentation Modulus of Elastically Orthotropic Solids for Conical Indenters. *Int. J. Solids Struct.*, 41(26):7351–7360, 2004.
- [16] P. Delobelle, S. Dali, and F. Richard. Interprétation du module d'indentation dans le cas des matériaux anisotropes et/ou actifs. *Matériaux Tech.*, 99(2):185–196, 2011.
- [17] Y. Dikmelik, J. B. Spicer, M. J. Fitch, and R. Osiander. Effects of Surface Roughness on Reflection Spectra Obtained by Terahertz Time-Domain Spectroscopy. *Opt. Lett.*, 31(24):3653, 2006.
- [18] DIN Deutsches Institut für Normung e. V. Metallische Werkstoffe - Instrumentierte Eindringprüfung zur Bestimmung der Härte und anderer Werkstoffparameter, 2015.
- [19] M. M. F. Doerner and W. D. W. Nix. A Method for Interpreting the Data From Depth-Sensing Indentation Instruments. *J. Mater. Res.*, 1(04):601–609, 1986.
- [20] K. Durst, B. Backes, and M. Göken. Indentation Size Effect in Metallic Materials: Correcting for the Size of the Plastic Zone. *Scr. Mater.*, 52(11):1093–1097, 2005.
- [21] W. Eberhard and W. Weislo. Plenty of Room at the Bottom? *Am. Sci.*, 100(3):226, 2012.
- [22] J. Evertsson, F. Bertram, F. Zhang, L. Rullik, L. R. Merte, M. Shipilin, M. Soldemo, S. Ahmadi, N. Vinogradov, F. Carlà, J. Weissenrieder, M. Göthelid, J. Pan, A. Mikkelsen, J. O. Nilsson, and E. Lundgren. The Thickness of Native Oxides on Aluminum Alloys and Single Crystals. *Appl. Surf. Sci.*, 349(April 2019):826–832, 2015.

- [23] P. Filippov, M. Kaufeld, M. Ebner, U. Koch, M. Kaufeld, and M. Ebner. Investigation of The Effect of End Mill-Geometry on Microstructure and Indentation Hardness of Aluminum Alloy AA6082. *Materials (Basel)*., 13(14):3078, 2020.
- [24] P. Filippov, S. Kiderlen, and U. Koch. Preparation of the Surfaces of High-Purity Polycrystalline Aluminum for the Mechanical Analysis by Means of Nanoindentation. *Pract. Metallogr.*, 57(6):397–414, 2020.
- [25] P. Filippov and U. Koch. Nanoindentation of Aluminum Single Crystals: Experimental Study on Influencing Factors. *Materials (Basel)*., 12(22):3688, 2019.
- [26] S. Filiz, C. M. Conley, M. B. Wasserman, and O. B. Ozdoganlar. An Experimental Investigation of Micro-Machinability of Copper 101 Using Tungsten Carbide Micro-Endmills. *Int. J. Mach. Tools Manuf.*, 47(7-8):1088–1100, 2007.
- [27] A. C. Fischer-Cripps. A Review of Analysis Methods for Sub-Micron Indentation Testing. *Vacuum*, 58(4):569–585, 2000.
- [28] A. C. Fischer-Cripps. *Nanoindentation*. Mechanical Engineering Series. Springer New York, New York, NY, third edit edition, 2011.
- [29] N. A. Fleck, G. M. Muller, M. F. Ashby, and J. W. Hutchinson. Strain Gradient Plasticity: Theory and Experiment. *Acta Metall. Mater.*, 42(2):475–487, 1994.
- [30] N. Gane and F. P. Bowden. Microdeformation of Solids. *J. Appl. Phys.*, 39(3):1432–1435, 1968.
- [31] N. Gane and J. M. Cox. The Micro-Hardness of Metals at Very Low Loads. *Philos. Mag.*, 22(179):0881–0891, 1970.
- [32] H. Gao and Y. Huang. Geometrically Necessary Dislocation and Size-Dependent Plasticity. *Scr. Mater.*, 48(2):113–118, 2003.
- [33] Q. Gao, Y. Gong, Y. Zhou, and X. Wen. Experimental Study of Micro-Milling Mechanism and Surface Quality of a Nickel-Based Single Crystal Superalloy. *J. Mech. Sci. Technol.*, 31(1):171–180, 2017.
- [34] Y. Geng, J. Zhang, Y. Yan, B. Yu, L. Geng, and T. Sun. Experimental and Theoretical Investigation of Crystallographic Orientation Dependence of Nanoscratching of Single Crystalline Copper. *PLoS One*, 10(7):e0131886, 2015.
- [35] W. W. Gerberich, N. I. Tymiak, J. C. Grunlan, M. F. Horstemeyer, and M. I. Baskes. Interpretations of Indentation Size Effects. *J. Appl. Mech. Trans. ASME*, 2002.
- [36] M. Göken. Nanoindentierungsprüfung. In H. Biermann and L. Krüger, editors, *Mod. Methoden der Werkstoffprüfung*, volume 49, chapter 9, pages 299–351. Wiley, 2014.

- [37] M. Göken and M. Kempf. Pop-Ins In Nanoindentations - The Initial Yield Point. *Zeitschrift für Met.*, 92(9):1061–1067, 2001.
- [38] M. Göken, M. Kempf, M. Bordenet, and H. Vehoff. Nanomechanical Characterizations of Metals and Thin Films. *Surf. Interface Anal.*, 27(5-6):302–306, 1999.
- [39] G. Gottstein. *Materialwissenschaft und Werkstofftechnik*. Springer-Lehrbuch. Springer Berlin Heidelberg, Berlin, Heidelberg, 2014.
- [40] G. Guillonueau, J. M. Wheeler, J. Wehrs, L. L. Philippe, P. Baral, H. W. Höppel, M. Göken, and J. Michler. Determination of the True Projected Contact Area by in Situ Indentation Testing. *J. Mater. Res.*, 34(24):4086–4086, 2019.
- [41] P. Haušild, A. Materna, and J. Nohava. Effect of crystallographic orientation on hardness and indentation modulus in austenitic stainless steel. *Key Eng. Mater.*, 586:31–34, 2013.
- [42] H. Hofmann and J. Spindler. Verfahren in der Beschichtungs- und Oberflächentechnik. In *Verfahren der Beschichtungs- und Oberflächentechnik*, pages 1–10. Carl Hanser Verlag GmbH & Co. KG, München, 2020.
- [43] Holger Schnarr. Strom ist die Lösung - oder die Lösung ohne Strom?: Gemeinschaftsversuch des Arbeitskreises Probenpräparation der DGM zum Thema Elektrolytische Präparation. In G. Petzow, editor, *Fortschritte der Metallogr.*, Sonderbände der Praktischen Metallographie, pages 25–30, Sankt Augustin, 2017. Inventum GmbH.
- [44] E. Hornbogen and H. Warlimont. *Metalle: Struktur und Eigenschaften der Metalle und Legierungen*. Springer Berlin Heidelberg, Berlin, Heidelberg, 2016.
- [45] IBM. IBM Unveils World’s First 2 Nanometer Chip Technology, Opening a New Frontier for Semiconductors, 2021.
- [46] T. Inamura, H. Hosoda, K. Wakashima, and S. Miyazaki. Anisotropy and Temperature Dependence of Young’s Modulus in Textured TiNbAl Biomedical Shape Memory Alloy. *Mater. Trans.*, 46(7):1597–1603, 2005.
- [47] A. Inoue. Bulk Glassy Alloys: Historical Development and Current Research. *Engineering*, 1(2):185–191, 2015.
- [48] T. Iwai, D. Mizutani, and M. Tani. The Effect Of Surface Roughness on High Frequency Transmission Line. In *2013 3rd IEEE CPMT Symp. Japan*, pages 1–4. IEEE, 2013.
- [49] R. H. T. J. E. Field. The Young Modulus and Poisson Ratio of Diamond. Technical report, Cavendish Laboratory, Cambridge, 1999.

- [50] A. S. Khan and S. Huang. *Continuum Theory of Plasticity*. John Wiley & Sons, Inc., New York, NY, 1995.
- [51] C. J. Kim, J. R. Mayor, and J. Ni. A Static Model of Chip Formation in Microscale Milling. *J. Manuf. Sci. Eng. Trans. ASME*, 126(4):710–718, 2004.
- [52] F. Klocke, K. Gerschwiler, and M. Abouridouane. Size Effects of Micro Drilling in Steel. *Prod. Eng.*, 3(1):69–72, 2009.
- [53] A. Korsunsky, M. McGurk, S. Bull, and T. Page. On the Hardness of Coated Systems. *Surf. Coatings Technol.*, 99(1-2):171–183, 1998.
- [54] S. Kucharski and D. Jarzabek. Depth Dependence of Nanoindentation Pile-Up Patterns in Copper Single Crystals. *Metall. Mater. Trans. A*, 45(11):4997–5008, 2014.
- [55] X. Lai, H. Li, C. Li, Z. Lin, and J. Ni. Modelling and Analysis of Micro Scale Milling Considering Size Effect, Micro Cutter Edge Radius and Minimum Chip Thickness. *Int. J. Mach. Tools Manuf.*, 48(1):1–14, 2008.
- [56] F. B. Langitan and B. R. Lawn. Hertzian Fracture Experiments on Abraded Glass Surfaces as Definitive Evidence for an Energy Balance Explanation of Auerbach’s Law. *J. Appl. Phys.*, 40(10):4009–4017, 1969.
- [57] P. Legendre and P. Dutilleul. Introduction to the Analysis of Periodic Phenomena. In *Rhythm. Fishes*, pages 11–25. Springer US, Boston, MA, 1992.
- [58] M. Lenz, Y. M. Eggeler, J. Müller, C. H. Zenk, N. Volz, P. Wollgramm, G. Eggeler, S. Neumeier, M. Göken, and E. Spiecker. Tension/Compression Asymmetry of a Creep Deformed Single Crystal Co-Base Superalloy. *Acta Mater.*, 166:597–610, 2019.
- [59] M. Liu. *Crystal Plasticity and Experimental Studies of Nano-Indentation of Aluminium and Copper*. Dissertation, University of Wollongong, Wollongong, Australia, 2014.
- [60] M. Liu, C. Lu, K. A. Tieu, C.-T. T. Peng, and C. Kong. A Combined Experimental-Numerical Approach for Determining Mechanical Properties of Aluminum Subjects to Nanoindentation. *Sci. Rep.*, 5(1):15072, 2015.
- [61] Y. Liu, S. Varghese, J. Ma, M. Yoshino, H. Lu, and R. Komanduri. Orientation Effects in Nanoindentation of Single Crystal Copper. *Int. J. Plast.*, 24(11):1990–2015, 2008.
- [62] Y.-Y. Lv, L.-F. Zhang, G.-X. Wang, and Y. Xiong. Effect of Rolling and Annealing on Microstructure and Mechanical Properties of High Purity Aluminum. In *Proc. 3rd Annu. Int. Conf. Adv. Mater. Eng. (AME 2017)*, volume 110, pages 93–98, Paris, France, 2017. Atlantis Press.

- [63] E. Macherauch, H.-W. Zoch, E. Macherauch, and H.-W. Zoch. Aushärtung einer AlCu-Legierung. *Prakt. Werkstoffkd.*, pages 250–256, 2011.
- [64] N. Maluf and K. R. Williams. *An Introduction to Microelectromechanical Systems Engineering*. Artech House, Inc., Norwood, 2nd edition, 2004.
- [65] J. Mandel. Measurement Statistics. In J. Mandel, editor, *Eval. Control Meas., Quality and reliability*, pages 5–13. Dekker, New York, NY, 1991.
- [66] K. W. McElhaney, J. J. Vlassak, and W. D. Nix. Determination of Indenter Tip Geometry and Indentation Contact Area for Depth-Sensing Indentation Experiments. *J. Mater. Res.*, 13(5):1300–1306, 1998.
- [67] E. Merson, R. Brydson, and A. Brown. The Effect of Crystallographic Orientation on the Mechanical Properties of Titanium. *J. Phys. Conf. Ser.*, 126:012020, 2008.
- [68] D. Meschede, H. Vogel, and C. Gerthsen. 1.3.3 Die harmonische Schwingung. In D. Meschede, H. Vogel, and C. Gerthsen, editors, *Gerthsen Phys.*, Springer-Lehrbuch, pages 23–24. Springer, Berlin, 2010.
- [69] Z. Niu, F. Jiao, and K. Cheng. An Innovative Investigation on Chip Formation Mechanisms in Micro-Milling Using Natural Diamond and Tungsten Carbide Tools. *J. Manuf. Process.*, 31:382–394, 2018.
- [70] W. D. Nix and H. Gao. Indentation Size Effects in Crystalline Materials: A Law for Strain Gradient Plasticity. *J. Mech. Phys. Solids*, 46(3):411–425, 1998.
- [71] W. Oliver and G. Pharr. An Improved Technique for Determining Hardness and Elastic Modulus Using Load and Displacement Sensing Indentation Experiments. *J. Mater. Res.*, 7(6):1564–1583, 1992.
- [72] W. Oliver and G. Pharr. Measurement of hardness and elastic modulus by instrumented indentation: Advances in understanding and refinements to methodology. *J. Mater. Res.*, 19(1):3–20, 2004.
- [73] S. Pathak, J. Michler, K. Wasmer, and S. R. Kalidindi. Studying Grain Boundary Regions in Polycrystalline Materials Using Spherical Nano-Indentation and Orientation Imaging Microscopy. *J. Mater. Sci.*, 47(2):815–823, 2012.
- [74] M. Perrut, P. Caron, M. Thomas, and A. Couret. High temperature materials for aerospace applications: Ni-based superalloys and γ -TiAl alloys. *Comptes Rendus Phys.*, 19(8):657–671, 2018.
- [75] S. Rahimian Koloor, A. Karimzadeh, M. Tamin, and M. Abd Shukor. Effects of Sample and Indenter Configurations of Nanoindentation Experiment on the Mechanical Behavior and Properties of Ductile Materials. *Metals (Basel)*., 8(6):421, 2018.

- [76] J. Rösler, H. Harders, and M. Bäker. Mechanisches Verhalten der Metalle: Gleitsysteme. In *Mech. Verhal. der Werkstoffe*, pages 176–178. Springer Vieweg, Wiesbaden, Wiesbaden, 2016.
- [77] J. Rösler, H. Harders, and M. Bäker. *Mechanisches Verhalten der Werkstoffe*. Springer Vieweg, Wiesbaden, Wiesbaden, 2016.
- [78] B. S. H. Royce, A. Niculin, and P. Batke. The Structure and Properties of Engineering Materials, 2001.
- [79] T. Sakai and J. Jonas. Plastic Deformation: Role of Recovery and Recrystallization. In *Ref. Modul. Mater. Sci. Mater. Eng.*, pages 1–6. Elsevier, 2016.
- [80] G. M. Scamans, M. F. Frolich, W. M. Rainforth, Z. Zhou, Y. Liu, X. Zhouc, and G. E. Thompsonc. The Ubiquitous Beilby Layer on Aluminium Surfaces. *Surf. Interface Anal.*, 42(4):175–179, 2010.
- [81] J. Schindelin, I. Arganda-Carreras, E. Frise, V. Kaynig, M. Longair, T. Pietzsch, S. Preibisch, C. Rueden, S. Saalfeld, B. Schmid, J.-Y. Tinevez, D. J. White, V. Hartenstein, K. Eliceiri, P. Tomancak, and A. Cardona. Fiji: An Open-Source Platform for Biological-Image Analysis. *Nat. Methods*, 9(7):676–682, 2012.
- [82] C. A. Schuh. Nanoindentation Studies of Materials. *Mater. Today*, 9(5):32–40, 2006.
- [83] M. Shell De Guzman, G. Neubauer, P. Flinn, and W. D. Nix. The Role of Indentation Depth on the Measured Hardness of Materials. *MRS Proc.*, 308:613, 1993.
- [84] G. Simmons and H. Wang. *Single Crystal Elastic Constants and Calculated Aggregate Properties: A Handbook*. M.I.T. Press, Cambridge (Mass.), 2nd ed. edition, 1971.
- [85] R. L. Smith and G. E. Sandly. An Accurate Method of Determining the Hardness of Metals, with Particular Reference to Those of a High Degree of Hardness. *Proc. Inst. Mech. Eng.*, 102(1):623–641, 1922.
- [86] I. N. Sneddon. The Relation Between Load and Penetration in the Axisymmetric Boussinesq Problem for a Punch of Arbitrary Profile. *Int. J. Eng. Sci.*, 3(1):47–57, 1965.
- [87] N. A. Stelmashenko, M. G. Walls, L. M. Brown, and Y. V. Milman. Microindentations on W and Mo Oriented Single Arystals: An STM Study. *Acta Metall. Mater.*, 1993.
- [88] X. Sun and K. Cheng. *Micro-/Nano-Machining Through Mechanical Cutting*. Yi Qin, second edi edition, 2015.
- [89] L. Teplyakova, I. Bespalova, and T. Kunitsyna. Rules of Fragmentation and Localization at Aluminium Single Crystal Division During Compression Test. *Adv. Mater. Res.*, 1013:84–90, 2014.

- [90] L. Teplyakova, T. Kunitsyna, and I. Bespalova. Multiscale Localization of Deformation in Single Crystals fcc With Compression. *Tambov Univ. Reports. Ser. Nat. Tech. Sci.*, 21(3):1342–1345, 2016.
- [91] Y. Tian, X. Shang, and M. J. Lancaster. Fabrication of Multilayered SU8 Structure for Terahertz Waveguide with Ultralow Transmission Loss. *J. Micro/Nanolithography, MEMS, MOEMS*, 13(1):013002, 2014.
- [92] J. R. Tuck, A. M. Korsunsky, R. I. Davidson, S. J. Bull, and D. M. Elliott. Modelling of the Hardness of Electroplated Nickel Coatings on Copper Substrates. *Surf. Coatings Technol.*, 127(1):1–8, 2000.
- [93] J. R. Tuck, A. M. Korsunsky, S. J. Bull, and R. I. Davidson. On The Application of the Work-Of-Indentation Approach to Depth-Sensing Indentation Experiments in Coated Systems. *Surf. Coatings Technol.*, 137(2-3):217–224, 2001.
- [94] J. J. Vlassak and W. Nix. Measuring the Elastic Properties of Anisotropic Materials by Means of Indentation Experiments. *J. Mech. Phys. Solids*, 42(8):1223–1245, 1994.
- [95] J. J. Vlassak and W. D. Nix. Indentation Modulus of Elastically Anisotropic Half Spaces. *Philos. Mag. A Phys. Condens. Matter, Struct. Defects Mech. Prop.*, 67(5):1045–1056, 1993.
- [96] G. Wang, Z. Liu, W. Huang, B. Wang, and J. Niu. Influence of Cutting Parameters on Surface Roughness and Strain Hardening During Milling NiTi Shape Memory Alloy. *Int. J. Adv. Manuf. Technol.*, 102(5-8):2211–2221, 2019.
- [97] Z. Wang, H. Bei, E. George, and G. Pharr. Influences of Surface Preparation On Nanoindentation Pop-In in Single-Crystal Mo. *Scr. Mater.*, 65(6):469–472, 2011.
- [98] Z. Wang, J. Zhang, H. ul Hassan, J. Zhang, Y. Yan, A. Hartmaier, and T. Sun. Coupled Effect of Crystallographic Orientation and Indenter Geometry on Nanoindentation of Single Crystalline Copper. *Int. J. Mech. Sci.*, 148:531–539, 2018.
- [99] T. Williams, C. Kelley, J. Campbell, R. Cunningham, D. Denholm, G. Elber, R. Fearick, C. Grammes, L. Hart, L. Hecking, T. Koenig, D. Kotz, E. Kubaitis, R. Lang, A. Lehmann, A. Mai, M. Bastian, E. A. Merritt, P. Mikul, T. Tkacik, J. V. D. Woude, J. R. V. Zandt, A. Woo, and J. Zellner. Gnuplot 5.2 Manual, 2019.
- [100] H. Worch. Mechanische Erscheinungen. In H. Worch, editor, *Werkstoffwissenschaft*, Master, pages 197–406. Wiley-VCH-Verl., Weinheim, 2011.
- [101] M. Yoshida, T. Sumomogi, T. Kino, M. Okumiya, and Y. Tsunekawa. The Relation of Crystallographic Plane with Strength and Deformation Properties of High Purity Aluminum Single Crystals during Nanoindentation. *J. Japan Inst. Met.*, 73(2):95–102, 2009.

- [102] Z. Yuan, M. Zhou, and S. Dong. Effect of Diamond Tool Sharpness on Minimum Cutting Thickness and Cutting Surface Integrity in Ultraprecision Machining. *J. Mater. Process. Technol.*, 62(4):327–330, 1996.
- [103] A. Zahedi, M. Demiral, A. Roy, V. I. Babitsky, and V. V. Silberschmidt. Indentation in F.C.C. Single Crystals. *Solid State Phenom.*, 188:219–225, 2012.
- [104] T. Zhou, Y. Yang, and M. Shuai. Constitutive Model Research on Pure Aluminum Considering Dynamic Recovery and Recrystallization. In *Proc. 2016 3rd Int. Conf. Mechatronics Inf. Technol.*, pages 747–752, Paris, France, 2016. Atlantis Press.
- [105] Q. F. Zhu, Z. H. Zhao, Y. B. Zuo, L. Li, and J. Z. Cui. The Structure Evolution of a 99.995 Percent High Purity Aluminum during Multi-Forging Process in Room Temperature. *Mater. Sci. Forum*, 794-796:876–881, 2014.
- [106] E. Zschech. Metallkundliche Prozesse bei der Wärmebehandlung aushärtbarer Aluminiumlegierungen. *HTM - Haerterei-Technische Mitteilungen*, 1996.

List of Figures

2.1	Scheme of a typical nanoindenter in the ‘C’-configuration. All components including the sample, indenter and the C-shaped device frame contribute to the compliance of the system. This setup differs from the Fischer “Picodentor HM500” device configuration shown in Figure 5.7.	8
2.2	Basic procedure of a nanoindentation experiment. (a) Schematic indentation load-time curves. Basic indentation procedure including a load and unload phase (orange). The procedure can be extended with an additional hold period at maximum load (blue). (b) Load-depth curves resulting from the load-time curves in (a). Basic indentation procedure including a load and unload phase (orange dashed line) and the procedure modified with the hold period (blue line).	8
2.3	Schematic cross-sectional view on the indented surface under load and after load removal. The indentation depth h is the maximum vertical displacement of the indenter during indentation. The contact height h_c is the depth at which the indenter has actual contact with the sample surface. After load removal, the depth of the remaining impression is the residual depth h_f . h_s is merely the difference between h and h_c . Figure from [71], reproduced with permission from Springer Nature.	10
2.4	Scheme of a load-depth curve with the most important indentation parameters of the Oliver-Pharr analysis. Here, the difference between maximum indentation depth h_{max} and the contact depth h_c is notable. Figure from [71], reproduced with permission from Springer Nature.	10
2.5	(a) Illustration of the C-type indenter frame. The initial geometry of the indenter frame is shown in gray. After applying the load P to the sample, the frame is also deformed elastically (black shape). The difference between both states is the deflection c . (b) Spring-model of the system stiffness. The frame and the contact stiffness are modeled as two springs in series. Figure based on [28].	13
2.6	Specifications of the employed indenters according to the DIN EN ISO 14577-2. The Vickers indenter (left) is based on a regular square pyramid with $\alpha = 136^\circ \pm 0.3^\circ$ (angle between opposite lateral faces). The Berkovich indenter (right) is based on a tetrahedron with $\beta = 65^\circ \pm 0.3^\circ$ (angle between the center line and a lateral face).	15

2.7	Schematic depiction of the indenter tip shape (a) Ideal indenter tip. (b) Actual indenter shape (exact geometry is usually inaccessible). (c) The indenter is modeled as a cone with a spherical tip with radius R (sufficient for most experiments).	15
2.8	Schematic depiction of the pile-up and sink-in effect with a Berkovich indenter (three-sided pyramid), and their implications on indentation hardness and modulus calculated according to the Oliver-Pharr method.[28]	17
2.9	Schematic depiction of GND underneath the indenter tip. (a) The material beneath the indenter is pushed into the bulk, resulting in the creation of additional defects (plastic zone). (b) On small scale atomic steps are produced on the deformed surface. Each step is associated with a single GND. Figure based on [70].	18
2.10	Principal indentation with a blunt indenter (i.e. spherical tip) on a rough surface. The actual contact area (red) between the indenter and the surface is lowered due to surface roughness.	19
2.11	Indentation with a sharp indenter (i.e. Berkovich) on a rough surface. The actual contact area, hence indentation hardness depends on the indent position: (a) Roughness peak: hardness is underestimated. (b) Flank: hardness depends on the flank slope. (c) Valley: hardness is overestimated. Figure based on [9]	19
2.12	Scheme of an indentation of a film-substrate system with a sharp indenter. The substrate influence on measured hardness depends on the film thickness t and indentation depth h . Figure adapted from [10]	21
2.13	Anticipated hardness-depth curve of an indentation through a film-substrate system (hard film, soft substrate). (a) Film-dominated region (Indentation depth significantly lower than film thickness) (b) Transitional region (indentation depth in the range of film thickness). (c) Substrate-dominated region (Indentation depths exceeds film thickness significantly).	21
3.1	Face centered cubic crystal lattice with three major lattice planes (100), (110) and (111) (grey areas).	26
3.2	Illustration of two different possibilities (not inclusive) for arrangement of atoms in a metal. (a) Single crystal structure with a distinct orientation (extends to sample boundaries). (b) A polycrystal consisting of many differently orientated grains (single crystals) with identical lattice structure, separated by grain boundaries (dashed line).	26
3.3	Sliding of complete atomic planes in a single crystal. (a) Undisturbed atomic order without applied load. (b) The load is applied and the atomic bonds are stretched reversibly (two blue atoms are connected via a blue atomic bond). (c) All atomic bonds along the plane (blue) simultaneously flip to the next atom on the left side to accommodate the stress. Figure adapted from [77].	31

3.4	Movement of a step-dislocation due to external stress. (a) Undisturbed atomic order without load. The dislocation is marked with an upside-down “T”. (b) Applying shear stress below the CRSS leads to an elastically distorted structure. (c) Once the shear stress exceeds the CRSS, a single atomic bond (blue) flips to the next atom, moving the dislocation by one lattice constant.	31
3.5	Four slip planes of a fcc structure with the $\{111\} \langle 1\bar{1}0 \rangle$ slip system are illustrated in a unit cell. Four of the eight crystallographically equivalent planes have a different orientation. Three different directions per plane (white arrows) results in 12 possible slip-directions for a fcc structure. Image adapted from [77].	33
3.6	Exemplary load-depth curve showing a discontinuity at low indentation depth directly after there Hertzian contact. The curve was acquired on oxidized NiAl surface. Figure from [38], reproduced with permission from John Wiley and Sons.	33
3.7	SEM image of an exemplary AA5083 microstructure at two different magnifications. (a) Triple point between three grains separated by grain boundaries and several micrometer-sized intermetallic phases (light gray especially on the top left) (b) Close-up on small sub-micrometer intermetallic phases (rounded and elongate, light gray) (SEM imaging parameters: 10kV, BSE detector, 8 mm working distance)	38
3.8	Scheme of a complex microstructure resulting from different strengthening measures. Different microstructural features on varying length scales are depicted: (1) Substitutional atoms (solid solution strengthening) (2) Grains with different orientations (3) grain boundaries, (4) dislocations, (5) GP zones (precipitations < 100 nm), (6) dispersoids (< 1000 nm), (7) intermetallic particles ($< 20 \mu\text{m}$) and (8) coarse second phase.	38
4.1	Typical structure of a mechanically influenced aluminum surface. Figure adapted from [42].	42
4.2	Chip formation depending on the cutting edge radius r_e and the uncut chip thickness h . (a) Traditional cutting with infinitely small r_e . (b) Micro-cutting with the r_e in the same range as h . Figure from [1], reproduced with permission from Elsevier	44
4.3	The effect of h on chip formation and surface strain-hardening due to the ploughing-effect. (a) $h < r_e$. (b) $h \approx r_e$. (c) $h > r_e$. Figure from [1]	45
5.1	Compression setup with a cylindric Al specimen mounted between two round compression plates of the “Zwick Retro Line” (Table B.1) and covered by PTFE tape at top and bottom.	50
5.2	Scheme of the machined structures with corresponding process parameters.	52
5.3	Illustration of the tool parameters wedge angle β and cutting edge radius r along with single tooth feed f_z and milling direction.	52

5.4	Illustration of the sample preparation. (a) Sample separation from the bulk. (b) Mounting/Embedding the sample in a resin. (c) Plane grinding the embedded sample. (d) Polishing of the specimen.	53
5.5	Light microscopy 3D multi focus image of an embedded sample with the resin surface damaged due to excessive heat development. The surface (plain-ground resin) is flat in the distance of the metallic sample (1). Close to the metallic sample (3) the surface has substantially bulged due to excessive heat development (2). This produces a significant step (irreproducible, on average above 100 μm) between the deformed resin (2) and the electropolished specimen surface (3) resulting in undefined fringes around the metal sample. Image adapted from [24].	55
5.6	Photographs of the Picodentor HM500 at the installation site in the Laboratory of Materials Engineering, Munich University of Applied Sciences. (a) Device overview (b) Centerpiece of the instrument with measuring head, two-axis stage and microscope.	58
5.7	Sketch of the Helmut-Fischer frame design with a SDH. To be compared to the basic nanoindenter device layout shown in Figure 2.1. The device frame is excluded from the measurement by which the system compliance is reduced significantly.	59
5.8	Sketch of two typical problems that occur when the SDH-unit is placed on an electropolished microsection surface (a) The SDH-unit is rests on the resin, while the indenter is on the metal. (b) The SDH-unit damages the surface of ductile metal specimens.	60
5.9	Exemplary indentation curve on a Al5N-SX-(110) sample obtained with the “basic”-parameters from Table 5.6. (a) Programmed time-load-curve. (b) Resulting load-depth curve.	62
5.10	Exemplary multi-step indentation curves acquired on a Al5N-Poly (rod, as drawn) sample. (a) Programmed time-load-curve with parameters according to Table 5.7. (b) Resulting load-depth curve.	64
6.1	Images of electropolished Al5N surface: (a) Reflected light microscopy (b) SEM image	68
6.2	AFM image of an electropolished ultra-pure aluminum surface with a height difference of approx. 180 nm between the lowest and the highest point . . .	69
6.3	Typical load-depth curves used for the pop-in analysis (curves 1-15). Pop-ins on an exemplary data set (red rectangles) marking the transition from elastic (0-25 nm) to elastic-plastic deformation (> 25 nm) are marked with arrows. Multiple pop-ins observed on some curves can be attributed to subsequent dislocation events.	70

6.4	Indentation profile from the embedding epoxy to the specimen. Overall ca. 120 indentations over a distance l of 7 mm from start to the end were acquired. Different parameters are plotted as a function of the distance l : (a) Indentation hardness H_{IT} , (b) Indentation modulus E_{IT} and (c) Absolute indenter displacement h_0	71
6.5	Illustration of the maximum allowed area of the indentation array due to the stamp effect. The array starts at the point A and ends at the point B . The circle corresponds to the inner rim of the SDH when the indenter tip is positioned in point A . L is the maximum allowed indentation array width and r_A is the SDH-radius. The available area is highlighted in blue (according to section 6.2.2).	71
6.6	Reflected light microscopy image of a 10×10 indentation array on the Al5N-Poly sample surface subject to the stamp effect. The indentation array in the center is surrounded by impressions of the SDH.	72
6.7	Mapping of the absolute vertical position of the indenter (working distance) h_0 . Square 10×10 1 mm wide nanoindentation array obtained on electropolished Al5N-Poly sample (recrystallized by the manufacturer). Maximum height difference is approx. 700 nm.	72
6.8	H_{IT} and E_{IT} of recrystallized Al5N acquired on three independent samples. Mean values are determined from 10×10 indentation arrays per sample. Error bars denote standard deviations. This plot confirms a low sample-to-sample variation, suggesting high reproducibility.	73
7.1	Indentation load-displacement curves on the aluminum (111)-single-crystal surface electrolytically (electropolished) and mechanically polished samples. A discontinuity at a load of approx. 250 μ N can be observed only for the electropolished sample, whereas the mechanically polished sample shows a continuous load-depth behavior.	80
7.2	Optical images of pile-up patterns ($F_{max} = 60$ mN) on three crystallographic orientations of aluminum single crystals. Indenter and crystal lattice in aligned configuration: (a) : (100), (b) : (110), (c) : (111). Indents on the same surfaces with the sample azimuthally rotated by 45° clockwise resulting in mis-aligned patterns: (d) : (100), (e) : (110), (f) : (111). Although the relative orientation of the quadratic Vickers indenter relative to the crystal has been change, the resulting pile-up patterns still resemble the underlying crystal symmetry. The symbol in the upper left corner of each image (square, rectangle, triangle) illustrates the crystal symmetry and it's orientation in respect to the indentr.	81
7.3	SEM image of the indented area ($F_{max} = 10$ mN) on the crystallographic (100) orientation of aluminum single crystal (aligned). A_p is outlined by the solid and A_c by the dashed line.	82
7.4	Dependence of the factor α on the crystal and indenter orientation. Average values with the error bar indicating the respective range ($\alpha_{max} - \alpha_{min}$).	83

7.5	Indentation curves produced with the 6×6 arrays on differently oriented Al single crystal surfaces: (a) (100) orientation, (b) (110) orientation, and (c) (111) orientation. The initial portion of the curves is shown in the insets to visualized the pop-ins.	84
7.6	Comparison of experimental H_{IT} for three crystallographic orientations of the aluminum single crystal to literature values (orange: this study, white: Liu et al. [60]). No information about the measurement error was available for [60].	85
7.7	Comparison of experimental M for three crystallographic orientations of the aluminum single crystal with theory and literature values. Orange: this study (experimental M), white: Liu et al. [60] (experimental M), grey: calculated M according to equation (3.4). No information about the measurement error was available for [60].	85
7.8	Measured H_{IT} (normalized to their respective mean values) as a function of the azimuthal indenter orientation on three crystallographic orientations. Black dots represent data points; solid lines represent fits according to equation (5.9).	86
7.9	Measured M (normalized to their respective mean values) as a function of the azimuthal indenter orientation on three crystallographic orientations. Black dots represent data points; solid lines represent fits according to equation (5.9).	86
8.1	Optical microscopy image (reflected light) of a recrystallized and uniaxially compressed Al5N-Poly specimen. Two types of grains are apparent: the smooth u-type and rough d-type.	92
8.2	Optical microscopy images demonstrating the evolution of the microstructure of polycrystalline aluminum subject to uniaxial compression. The η in % is denoted in the top of the respective image. The compression direction is perpendicular to the image plain.	93
8.3	Plot of E_{IT} as a function of post-indentation creep C_{IT} demonstrating non-desired dependency of E_{IT} on C_{IT} . Data with $C_{IT} < -1\%$ were excluded from the analysis. Data jittering along the x-axis is added to prevent overlay of single data points.	94
8.4	Optical microscopy of indentations with $F_{max} = 100\text{mN}$ on recrystallized and compressed ($\eta = 50\%$) Al5N-Poly. (a) Indent on a d-type grain (smaller area, pile-up patterns depend on indenter geometry, $H_{IT} = 559\text{MPa}$). (b) Indent on a u-type grain (larger area, pile-up patterns depend on the crystallographic grain orientation, $H_{IT} = 207\text{MPa}$).	96

8.5	Summary of H_{IT} and E_{IT} data as a function of the degree of deformation η . Data points for which $C_{IT} < -1\%$ are excluded from the analysis. Indents of the d-type (blue) are excluded from the 0%-deformation data set, since they are thought to be non-recrystallized regions originating from deformation during sample manufacturing. The u-type indents (red) are excluded from the data sets with $\eta > 0\%$. The Data jittering (x-axis) was applied for better visibility i.e. to prevent overlap of single data points.	96
8.6	Average values for H_{IT} and E_{IT} of compressed Al5N-Poly specimen. The error bars correspond with respective standard deviation. The average values are calculated from low-creep data exclusively.	97
8.7	H_{IT} versus indentation depth curves obtained from multistep indentations of Al5N-poly specimen with η from 0% to 75% (denoted in the top of the respective graph). For $\eta = 75\%$ the H_{IT} at maximum indentation depth of both groups of curves is approximated as $H_1 = 230$ MPa and $H_2 = 740$ MPa.	98
8.8	M versus indentation depth curves obtained from multistep indentations of Al5N-poly specimen with η from 0% to 75% (denoted in the top of the respective graph). For $\eta = 75\%$ M at maximum indentation depth of both groups of curves is approximated as $M_1 = 73$ GPa and $M_2 = 85$ GPa.	99
9.1	SEM-images on the flank (left hand side) and rake face (right hand side) of the utilized tools. (a) SC-tool, (b) MD-tool.	106
9.2	SEM-images of the cutting edge radius, acquired parallel to the tool axis. The yellow circles indicate the measured tool radius. (a) SC-tool, $r = 671$ nm. (b) MD-tool, $r = 17$ nm. The image (b) (MD-tool) has a ten times higher magnification (note the scale bar).	106
9.3	Optical microscopy images of the cutting edges for the evaluation of the cutting edge roughness. The images are taken from the direction of the rake face. (a) SC-tool, (b) MD-tool.	106
9.4	Example of micromachined structures. The roughness and indentation measurements have been performed on the horizontal surface.	107
9.5	Confocal microscopy images of AA6082 surfaces milled with $f_z = 3$ μm : (a) SC-tool, (b) MD-tool.	108
9.6	Confocal microscopy images of AA6082 surfaces milled with $f_z = 8$ μm : (a) SC-tool, (b) MD-tool.	108
9.7	Confocal microscopy images of AA6082 surfaces milled with $f_z = 14$ μm : (a) SC-tool, (b) MD-tool.	108
9.8	Summary of vertical one-dimensional roughness R_q and R_t for the different feeds f_z	109
9.9	Summary of horizontal one-dimensional roughness R_q and R_t for the different feeds f_z	109
9.10	Exemplary SEM image of the AA6082 surface milled by the MD-tool and the indentation made according to the ESP-protocoll.	110

9.11	Indentation hardness-depth-curves of machined surfaces in comparison to electropolished AA6082 and polycrystalline Al5N surface as a reference. (a) SC-tool and (b) MD-tool machined surface.	111
9.12	Film-substrate-models fitted to experimental multi-step indentation data. Multi-step indentation data (Ind.) of surfaces produced with two different tools (SC/MD) is fitted to the Korsunsky-Model from Equation (5.10) [53] and the exponential model from equation (5.11). (a),(d): $f_z = 3 \mu\text{m}$, (b),(e): $f_z = 8 \mu\text{m}$, (c),(f): $f_z = 14 \mu\text{m}$	113
9.13	Summarized indentation hardness of aluminum with different microstructures and after different treatments and surface preparation procedures. All hardness values were obtained for the indentation depth of approx. $1.2 \mu\text{m}$	114
9.14	Different models for the interpretation of the indentation results. (a) Uniformly hard film on softer substrate. (b) Gradually hardened surface. (c) Combination of a hard thin surface film and gradually hardened bulk. . . .	116
A.1	Laue diffractograms acquired along [100] (left) [110] (center) and [111] (right) directions of the aluminum single crystals. The crystal integrity is verified by the observed sharp reflexes. The crystallographic orientations are confirmed by the respective symmetries.	124
B.1	Electromet III by Buehler Ltd.	126
C.1	Residual analysis of the fit to the azimuthal indenter orientation data. $e_{M, \text{normalized}}$ (a)-(c). $e_{\text{HIT}, \text{normalized}}$: (d)-(f).	128

List of Tables

5.1	Overview of raw materials used in this study. The code given in the first column is used throughout the present study. Additional information including the chemical composition is provided in chapter A, for exact reference see right column.	48
5.2	Overview of samples investigated in the experimental part of this work. The base materials from Table 5.1 with the respective form, sample orientation, bulk and surface treatments are represented.	49
5.3	Load and strain resulting from the compression of the Al5N-Poly (rod) specimens on the “Zwick Retro Line”. Nominal strain from the devices traverse measurement. Real strain from the micrometer screw gauge measurement.	51
5.4	Parameters of the mechanical polishing of aluminum samples, for used materials see Table B.2	53
5.5	Overview of the different techniques used for roughness determination	56
5.6	Indentation parameters used for the “basic” indentation and “pop-in”-analysis.	62
5.7	Multi-step indentation parameters that were used for AA6082 and Al5N specimens to achieve similar indentation depths.	63
6.1	Roughness values determined based on three AFM images (one example shown in Figure 6.2)	68
7.1	Proportion of the load-depth curves that exhibit pop-ins. The analysis is based on the curves from two data sets dealing with the influence of relative (1) crystal orientation and (2) the azimuthal orientation between the indenter and the sample.	78
7.2	Determined h_p and H_t ($F_{max} = 10$ mN, (110) direction) in comparison to h_c and H_{IT} determined according to the method of Oliver and Pharr.	79
7.3	Values of the fitted parameters x_0 in comparison to σ of the corresponding data sets from the measurement series of the azimuthal indenter orientation influence on H_{IT} and M	83
7.4	Comparison of M_{uvw} values obtained in this study compared to the literature. The values are given with the precision of the corresponding original publication.	88

8.1	Characteristic features of indentation on the u-type and d-type grains. . . .	95
9.1	Average values of the cutting edge roughness R_q and R_t for the SC- and MD-tool with the standard deviation σ	105
9.2	Summary of the minimum (at max. depth) and maximum (at min. depth) hardness values and the onset depth of strain-hardening for all machined samples. Average 8%-onset values are presented in the table.	110
A.1	Contamination analysis of Al5N-Poly (plate) (from the data-sheet provided by the supplier, HMW Hauner GmbH & Co. KG, Röttenbach, Germany, obtained by optical emission spectroscopy)	123
A.2	Contamination analysis of Al5N-Poly (rod) (from the data-sheet provided by the supplier, Goodfellow GmbH, Hamburg, Germany)	123
A.3	Chemical composition of AA6082 (from the data-sheet provided by the supplier, ALRO S. A, Slatina, Romania)	123
B.1	List of used devices	125
B.2	Chemical agents and materials used for polishing	126
D.1	Fitted parameters of the Korsunsky and the exponential fitted to the depth-hardness data from Figure 9.11.	130

Lebenslauf

Pavel Sergeevic Filippov, geboren am 10. August 1983 in Tver, Russland (ehemals Kalinin, UdSSR)

Ausbildung

2016 - 2021: Dr. rer. nat. in Kristallographie and der Ludwig-Maximilians-Universität München, Fakultät für Geowissenschaften

2010 - 2012: M. Sc. in Mikro- und Nanotechnik an der Hochschule München, Fakultät für angewandte Naturwissenschaften und Mechatronik

2006 - 2010: B. Eng in Bioingenieurwesen an der Hochschule München, Fakultät für angewandte Naturwissenschaften und Mechatronik

Arbeitserfahrung

2020 - 2022: Application Scientist bei der FemtoTools AG in Buchs/ZH, Schweiz

2016 - 2020: Wissenschaftlicher Mitarbeiter an der Hochschule München, Fakultät für angewandte Naturwissenschaften und Mechatronik, Labor für Werkstofftechnik

2012 - 2016: Prozessingenieur bei der Nanotools GmbH in München

Publikationen

1. P. Filippov, M. Kaufeld, M. Ebner, U. Koch, Investigation of the Effect of End Mill-Geometry on Roughness and Surface Strain-Hardening of Aluminum Alloy AA6082, *Materials (Basel)*. 13 (2020) 3078. <https://doi.org/10.3390/ma13143078>.
2. P. Filippov, S. Kiderlen, U. Koch, Preparation of the Surfaces of High-Purity Polycrystalline Aluminum for the Mechanical Analysis by Means of Nanoindentation, *Pract. Metallogr.* 57 (2020) 397–414. <https://doi.org/10.3139/147.110633>.
3. P. Lechner, P. Filippov, N. Kraschienski, F. Ettemeyer, W. Volk, A Novel Method for Measuring Elastic Modulus of Foundry Silicate Binders, *Int. J. Met.* 14 (2020) 423–431. <https://doi.org/10.1007/s40962-019-00361-w>.
4. P. Filippov, U. Koch, Nanoindentation of Aluminum Single Crystals: Experimental Study on Influencing Factors, *Materials (Basel)*. 12 (2019) 3688. <https://doi.org/10.3390/ma12223688>.

Fachvorträge

1. P. Filippov, U. Koch, Präparation dünner Aluminiumproben für die mechanische Analyse mittels Nanoindentierung, in: A. Neidel (Ed.), 53. Metallogr. 2019 - "Fortschritte Der Metallogr.", Petzow, G., Dresden, 2019. ISBN 978-3-88355-417-4.
2. P. Filippov, U. Koch, The Effect of Crystal Anisotropy and Azimuthal Indenter Orientation on the Indentation Hardness and Modulus of Single Crystal Aluminum, in: Material Science and Engineering, Online, 2020.